Standard Model Z/gamma to ee production in early data at ATLAS

Thesis submitted in accordance with the requirements of
the University of Liverpool for the degree of Doctor in Philosophy
by
Michael James Flowerdew

December 2009

Abstract

Standard Model Z/gamma to ee production in early data at ATLAS

Michael James Flowerdew

This thesis examines the measurement of the $Z/\gamma^* \to e^+e^-$ production cross section using 10 TeV pp collisions in the ATLAS detector, including a full analysis of theoretical and experimental uncertainties. Theoretical uncertainties on the kinematic event acceptance arising from QED and QCD processes are estimated, and a method for improving the Monte Carlo background estimate is introduced. The measurement of electron trigger efficiencies from data with the $Z/\gamma^* \to e^+e^-$ channel is also studied, concluding that with between 50 and 150 pb^{-1} of data, differential trigger efficiencies can be measured with $0.5-1\%$ precision. The expected uncertainty on the cross section measured with 200 pb^{-1} of data is

$$\frac{\Delta\sigma_{Z/\gamma^*\to e^+e^-}}{\sigma_{Z/\gamma^*\to e^+e^-}} = 0.44\% \text{ (stat.)} \pm 2.5\% \text{ (exp.)} \pm 1.6\% \text{ (theory)} \pm (5-30)\% \text{ (lumi.)}.$$

Contents

Acknowledgements

I would like to begin by thanking my supervisor, Joost Vossebeld, for his patience and advice over the years, not to mention his top-quality proof reading. I would also like to thank the Science and Technology Facilities Council for their financial support throughout this time, as well as John Dainton and Phil Allport, who have led the Liverpool high energy physics group while I've been here.

Many people have made my time at Liverpool more productive and more enjoyable. I would like to thank Max and Uta Klein, and Jan Kretzschmar for their help and advice, especially over the last year. Thanks to Carl Gwilliam - your programming skills have been invaluable in the development of my own. I also want to thank Helen Hayward, Sarah Rigby, Andy Mehta, Sergey Burdin, Neil Jackson, Steve Maxfield, Thomas Kluge, Barry King and the rest of the staff and postdocs, who have been willing to discuss physics, coding and life in general over the years (usually over a cup of coffee). Thanks also to the computing, administrative and other staff of the physics department, especially Norma, your teacakes are sorely missed.

I would like to thank my collaborators from other institutes, especially Tony Weidberg, who devoted more time to me than I had any right to demand. I also thank everyone in the SM, trigger and egamma communities in ATLAS, as well as the "Elan" group, too many in total to name, who have answered questions, explained code and suggested further work. I would also like to thank my undergraduate tutors for a first-class physics education, especially Mandy Cooper-Sarkar, Justin Wark and Peter Read.

I also want to mention those friends who have supported, entertained and sometimes worked with me, both in Liverpool and CERN. First, those I grew to know whilst in St Genis, in particular: Ellie and Erik, Tina and David, Lily, Martin, Anthony, Nadia,

Anna, Denver and many others who made my time there so fun, and so memorable. Also, my fellow PhD students: AJ, Nick, Paul, Lisa, Katharine (and Pierre), Steph, Craig, Abdi, Sylwia, Bozydar, Georgios, James, Peter, Graham, Matt and Lorna. It would not have been the same without you, thanks. Finally, there are my friends from the Cantata choir (Liverpool) and Accordami (Geneva), especially Peter, Richard, Catherine, Blibs, Ken, Nina, Christoph and Anthony, who have been a source of music and entertainment for so long.

Many thanks need to go to my parents, who encouraged my mathematical leanings from a young age. Last of all, I want to thank Sarah, who by now has almost forgiven me for spending my first year of married life in a different country. You have been a source of strength, love and support when I needed it most, and for that I thank you.

Chapter 1

Introduction

Since the discovery of the electron a little over a hundred years ago [1], scientists working in the field of particle physics have been trying to peer ever deeper into the smallest elements of matter. Over the latter part of the twentieth century, larger and more energetic particle colliders have been built, allowing physicists to investigate the laws that apply at the smallest distance and time scales yet explored. This search is not complete, and the Large Hadron Collider (LHC), which is due to begin colliding protons this year, has been built at CERN in Geneva to extend our knowledge of nature into new realms.

The aim of this thesis is to investigate the measurement of the $Z/\gamma^* \rightarrow e^+e^-$ production cross section with early data at the LHC, using simulated events. This will extend equivalent measurements made at the world's current highest energy collider, the Tevatron [2, 3], and will test the high energy physics theories used to extrapolate current experimental results to the higher energy collisions which will occur at the LHC. In particular, it will test the extrapolation of lower energy measurements of the momentum distributions of quarks and gluons within the proton and our understanding of the strong nuclear interaction operating at these new energy scales.

Measurements of the Z and its decay into two electrons will also be important for the characterisation of the ATLAS detector during early running. The $Z/\gamma^* \rightarrow e^+e^-$ decay channel is expected to be relatively background-free, supplying a large, clean sample of high p_{T} electrons for reconstruction and trigger performance studies. This thesis includes one such study, an investigation into the measurement of electron trigger efficiencies using the $Z/\gamma^* \rightarrow e^+e^-$ decay channel.

1.1 Thesis outline

This thesis begins with a theoretical outline of the physics relevant for Z production at the LHC (Chapter 2). The Standard Model is introduced, together with a brief description of electroweak symmetry breaking, quantum chromodynamics (QCD), and Drell-Yan processes in hadron colliders. Chapter 3 continues with a description of the simulated Monte Carlo samples used throughout this thesis. It also contains a detailed investigation into the impact that QCD and electroweak processes have on the kinematic acceptance of $Z/\gamma^* \to e^+e^-$ events.

The next three chapters describe the ATLAS detector hardware and software. Chapter 4 provides an overview of the physical detector, including all of the major subdetectors and the trigger systems. Recent commissioning results from test beams, cosmic ray events and single beam running are also discussed. The methods used for reconstructing and triggering on electrons are introduced in Chapter 5. The ATLAS software framework and Grid computing is discussed in Chapter 6, along with a general purpose analysis software package written in the course of this analysis.

In Chapter 7, a method used to estimate the dominant background contributions for the $Z/\gamma^* \to e^+e^-$ channel is introduced. Limited computing resources make it impractical to simulate sufficient numbers of events to directly estimate these backgrounds. The method discussed is shown to improve the effective statistics of the samples which are available.

The measurement of electron trigger efficiencies from data is considered in Chapter 8. This is done using the "tag and probe" method, which has been used previously for similar studies at the Tevatron [2]. The method is validated on simulated Monte Carlo events. Various sources of bias and systematic uncertainty are investigated, and background removal is discussed in detail. The chapter ends with two case studies illustrating the method's robustness against problems with the trigger definitions, and its potential for use in debugging these problems.

Chapter 9 describes how early ATLAS data can be used to measure the Z/γ^* boson production cross section. Event selection and corrections for efficiencies and resolution effects are discussed. Two cross section definitions are considered, the observable

"kinematic" cross section $\sigma^{\text{kin}}_{Z/\gamma^* \to e^+e^-}$, and the total cross section with phase space extrapolation, $\sigma_{Z/\gamma^* \to e^+e^-}$. The experimental and theoretical uncertainties on both of these quantities are discussed. The conclusions and outlook for this and some related Standard Model measurements can be found in Chapter 10.

Chapter 2

The Drell-Yan process in p-p collisions

In this chapter, theoretical aspects of the Drell-Yan production of Z bosons at the LHC will be discussed. Section 2.1 begins by introducing the Standard Model of particle physics including discussions of the theory of electroweak interactions (Section 2.1.1) and of the strong nuclear force (Section 2.1.2). Finally, the physics of Z boson production in proton-proton collisions will be described in Section 2.2.

2.1 The Standard Model

The Standard Model (SM) of particle physics describes the properties and interactions of fundamental particles as we understand them today.[1] Two types of particles are described, the *bosons*, which transmit forces, and the *fermions*, which make matter. Matter and antimatter are largely treated equally within the SM, except in some rare particle decays.

The fundamental fermions are divided into two principal groups, based on whether they respond to the strong nuclear force. The *quarks* experience the strong force, whilst the *leptons* do not. The nature of the strong force is such that the quarks are not observed in nature as isolated particles, but combine to form *hadrons*, a phenomenon called *confinement* (see Section 2.1.2). Hadrons may be *mesons* ($q\overline{q}$, where q represents a quark and $\overline{q}$ an anti-quark), or *baryons* (qqq, or $\overline{qqq}$). There are also two categories of leptons: charged leptons, like the electron, and neutral leptons, the neutrinos.

Of the four forces known to physics, only three are represented in the SM. There is,

[1] For a more thorough introduction to the SM, see, for example, [4].

Table 2.1: Particle content of the SM. The typical symbols for each particle are given. The labelling of the generation only applies to fermions.

Category		Generation		
		1	2	3
Fermions (f)	Leptons (ℓ, ν)	e	μ	τ
		ν_e	ν_μ	ν_τ
	Quarks (q)	u	c	t
		d	s	b
Bosons (V)	Electroweak	W, Z, γ		
	Strong	g		

as yet, no accepted quantum theory of gravity, and hence no SM graviton. The strong nuclear force, already alluded to, is mediated by the *gluon* (g). The weak nuclear force is mediated by the massive W and Z bosons, while the electromagnetic force is mediated by the *photon* (γ). However, these two forces are known to represent the underlying *electroweak* force, described in Section 2.1.1.

The complete particle content of the Standard Model is listed in Table 2.1. This shows how the four types of fermions (charged leptons, neutrinos, up-type and down-type quarks) exist in three *generations*. The charged leptons and quarks in the second and third generations are more massive than those in the first, and are unstable. Conventional matter is thus made entirely of fermions from the first generation.

Fermions have a property, important for understanding the weak nuclear force, called *chirality*. For highly relativistic particles, chirality is related to helicity, which describes the direction of a particle's spin compared to its motion: either opposite (left-handed) or aligned (right-handed). If a fermion were massless, this analogy would hold exactly. For massive fermions, left- and right-handed chirality states are defined as eigenvectors of $(1 \mp \gamma^5)$, where γ^5 is one of the Dirac matrices [5].

The paradigm underlying forces in the Standard Model is that their properties are fixed by requiring local gauge invariance of the SM Lagrangian. The first major success of local gauge transformations was in the theory of *Quantum Electrodynamics*, or QED, the theory of electromagnetic interactions. The photon's potential A^μ is made to arise

naturally by insisting that a charged fermion's Lagrangian remains invariant under a local phase change $\exp\{\mathrm{i}\theta(x)\}$, where $\theta(x)$ is an arbitrary function of space-time. The factor $\exp\{\mathrm{i}\theta(x)\}$ is the generator of the U(1) group, which gives rise to a massless[2] vector boson - the photon.

Following the sucesses of QED, other symmetry groups have been put forward to explain the other known fundamental forces. In full, the Standard Model is described by the $\mathrm{SU}(3) \times \mathrm{SU}(2)_L \times \mathrm{U}(1)_Y$ symmetry group. The SU(3) component gives rise to the strong nuclear force. The weak nuclear force, described by $\mathrm{SU}(2)_L$, is labelled L to indicate that it only acts on chirally left-handed particles. $\mathrm{U}(1)_Y$ is similar to the U(1) symmetry of QED, but acts on a particle's *weak hypercharge* Y.[3]

2.1.1 The Glashow, Weinberg and Salam model of electroweak interactions

The theory of electroweak interactions was largely constructed in three papers by Glashow [6], Weinberg [7] and Salam [8] in the 1960's. They realised that the underlying symmetry group of these interactions is $\mathrm{SU}(2)_L \times \mathrm{U}(1)_Y$. This means that the Lagrangian describing the Standard Model fermions and bosons must be invariant as the fermion fields undergo the following local gauge transformation:[4]

$$\begin{aligned} \psi_{\mathrm{L}} &\rightarrow \exp\left[-\mathrm{i}\left(\frac{g'}{2}Y\theta'(x) + g\boldsymbol{I}\cdot\boldsymbol{\theta}(x)\right)\right]\psi_{\mathrm{L}} \\ \psi_{\mathrm{R}} &\rightarrow \exp\left[-\mathrm{i}\left(\frac{g'}{2}Y\theta'(x)\right)\right]\psi_{\mathrm{R}}. \end{aligned} \tag{2.1}$$

This represents a unitary transformation in $\mathrm{SU}(2)_L \times \mathrm{U}(1)_Y$ space, parameterised by $\theta'(x)$ and $\boldsymbol{\theta}(x)$, which are arbitrary functions of space-time. There are two intrinsic coupling constants (g' and g), each analagous to the electric charge e in QED, and two associated charges, the hypercharge Y and the weak isospin $\boldsymbol{I}$ (a three-element vector in $\mathrm{SU}(2)_L$ space, which is quantised along the third axis to give $I_3 = \pm\frac{1}{2}$). The components of $\boldsymbol{I}$ satisfy the commutation relation $[I_i, I_j] = \mathrm{i}\epsilon_{ijk}I_k$, making this a *non-Abelian* theory.

[2] The photon must be massless, as inserting a mass term into the QED Lagrangian would spoil the local gauge invariance.

[3] Y is equal to $2(Q - I_3)$, where Q is the particle's electric charge, and I_3 is the third component of weak isospin.

[4] Throughout this thesis, equations will be written using "natural" units, where $\hbar = c = 1$.

The weak nuclear force is chiral, as confirmed by experimental measurements of the neutrino helicity [9]. Mathematically, the left-handed fermions form $\mathrm{SU}(2)_L$ doublets, which may be represented as column vectors. For the first generation, these doublets are

$$\begin{pmatrix} \nu_e \\ e_\mathrm{L} \end{pmatrix} \text{and} \begin{pmatrix} u_\mathrm{L} \\ d_\mathrm{L} \end{pmatrix}. \tag{2.2}$$

The right-handed fermions e_R, u_R and d_R are singlets in the $\mathrm{SU}(2)_L$ representation, which in physical terms means they do not interact with the field generated by the $\mathrm{SU}(2)_L$ symmetry. This difference in behaviour between chiralities is the source of parity violation in weak interactions. Note that while a right-handed neutrino is allowed, there is no experimental support for its existence and so it does not form part of the theory.

Neglecting fermion mass terms (which are not invariant in electroweak theory), the Lagrangian for free fermions may be written as

$$\mathscr{L}_\mathrm{free} = \mathrm{i}\psi_\mathrm{L}^\dagger \gamma^\mu \partial_\mu \psi_\mathrm{L} + \mathrm{i}\psi_\mathrm{R}^\dagger \gamma^\mu \partial_\mu \psi_\mathrm{R}, \tag{2.3}$$

where a sum over all fermion flavours is implied. Under the transformation in Equation 2.1, the form of the Lagrangian in Equation 2.3 changes. Invariance can however be restored by replacing ∂_μ with a *covariant derivative*, which introduces new degrees of freedom interpreted as boson fields. This covariant derivative acts differently on left- and right-handed fields. In a perturbative approach, where $\theta'(x)$ and $\boldsymbol{\theta}(x)$ are small, these derivatives may be written as

$$\begin{aligned} \mathscr{D}_{\mathrm{L}\mu} &= \partial_\mu + \mathrm{i}\frac{g'}{2} Y B_\mu + \mathrm{i} g \boldsymbol{I} \cdot \boldsymbol{W}_\mu, \\ \text{and } \mathscr{D}_{\mathrm{R}\mu} &= \partial_\mu + \mathrm{i}\frac{g'}{2} Y B_\mu. \end{aligned} \tag{2.4}$$

To ensure gauge invariance, the new fields $\boldsymbol{W}_\mu$ and B_μ must transform correctly:

$$\begin{aligned} \boldsymbol{W}_\mu &\rightarrow \boldsymbol{W}_\mu + \partial_\mu \boldsymbol{\theta}(x) + g\boldsymbol{\theta}(x) \wedge \boldsymbol{W}_\mu \\ B_\mu &\rightarrow B_\mu + \partial_\mu \theta'(x). \end{aligned} \tag{2.5}$$

With these modifications, adding kinetic terms for the gauge fields completes the electroweak Lagrangian:

$$\mathscr{L}_\mathrm{EW} = \mathrm{i}\psi_\mathrm{L}^\dagger \gamma^\mu \mathscr{D}_{\mathrm{L}\mu} \psi_\mathrm{L} + \mathrm{i}\psi_\mathrm{R}^\dagger \gamma^\mu \mathscr{D}_{\mathrm{R}\mu} \psi_\mathrm{R} - \frac{1}{4} \boldsymbol{W}_{\mu\nu} \cdot \boldsymbol{W}^{\mu\nu} - \frac{1}{4} B_{\mu\nu} B^{\mu\nu}. \tag{2.6}$$

These kinetic terms are given by:

$$\begin{aligned} \boldsymbol{W}_{\mu\nu} &= \partial_\mu \boldsymbol{W}_\nu - \partial_\nu \boldsymbol{W}_\mu - g\boldsymbol{W}_\mu \wedge \boldsymbol{W}_\nu \\ B_{\mu\nu} &= \partial_\mu B_\nu - \partial_\nu B_\mu. \end{aligned} \tag{2.7}$$

The cross product term in $\boldsymbol{W}_{\mu\nu}$ is needed to compensate for the non-commutation of the weak isospin vector elements. This term represents self-coupling, where three or four bosons interact at a point (note that these fields do not yet correspond to the physical W or Z bosons).

Symmetry breaking

While the B_μ field could represent the electromagnetic field, the three $\boldsymbol{W}_\mu$ fields cannot directly produce the weak nuclear force we observe. This is a very short-range force, which means that the corresponding gauge bosons need to be very massive (the range of the force scales as $1/M_W$, *cf* [5], Section 11.9). However, introducing a mass term such as $-\frac{1}{2}M_W^2 \boldsymbol{W}_\mu \boldsymbol{W}^\mu$ would destroy the local gauge invariance of Equation 2.6.

This problem was eventually solved with the introduction of the *Higgs mechanism* [10, 11, 12]. This spontaneously breaks the $\mathrm{SU}(2)_L \times \mathrm{U}(1)_Y$ symmetry through the action of an $\mathrm{SU}(2)_L$ doublet of complex scalar fields ϕ:

$$\phi(x) = \frac{1}{\sqrt{2}} \begin{pmatrix} \phi_1(x) + \mathrm{i}\phi_2(x) \\ \phi_3(x) + \mathrm{i}\phi_4(x) \end{pmatrix}. \tag{2.8}$$

This doublet has a potential term in the Lagrangian which includes a quartic term in ϕ:

$$\mathscr{L}_{\text{Higgs}} = \mathscr{D}_{\mathrm{L}\mu}\phi^\dagger \mathscr{D}_{\mathrm{L}}^\mu \phi - V(\phi) = \mathscr{D}_{\mathrm{L}\mu}\phi^\dagger \mathscr{D}_{\mathrm{L}}^\mu \phi - \mu^2 \phi^\dagger \phi - \lambda(\phi^\dagger \phi)^2. \tag{2.9}$$

If $\mu^2 > 0$ and $\lambda < 0$, the potential $V(\phi)$ has a minimum at $\phi^\dagger\phi = -\mu^2/2\lambda$. This ground state is highly degenerate, with an infinite number of solutions. This gives rise to three massless Goldstone bosons, which can be eliminated through a suitable choice of gauge. The fourth, massive, boson is the *Higgs boson*, arising from oscillations in the remaining Higgs field $H(x)$. Writing $v = \sqrt{-\mu^2/2\lambda}$, ϕ may now be written as

$$\phi(x) = \frac{1}{\sqrt{2}} \begin{pmatrix} 0 \\ v + H(x) \end{pmatrix}. \tag{2.10}$$

Substituting this into Equation 2.9 gives mass terms involving the $\boldsymbol{W}_\mu$ and B_μ fields, through a mechanism which respects local gauge invariance. The physical electroweak bosons can now be identified, as the mass and charge eigenstates of these fields:

$$\begin{aligned} W^{+\mu} &= \frac{W_1^\mu + \mathrm{i}W_2^\mu}{\sqrt{2}} \\ W^{-\mu} &= \frac{W_1^\mu - \mathrm{i}W_2^\mu}{\sqrt{2}} \\ Z^\mu &= \cos\theta_W W_3^\mu - \sin\theta_W B^\mu \\ A^\mu &= \sin\theta_W W_3^\mu + \cos\theta_W B^\mu. \end{aligned} \tag{2.11}$$

The angle $\theta_W = \tan^{-1}(g'/g)$ is a parameter of the theory, and describes the mixing between the weak boson W_3^μ and B^μ. It is defined such that the photon field A^μ is massless. The mass of the W is given by $M_W = \sqrt{-2\mu^2}$, while the Z mass is $M_Z = M_W/\cos\theta_W$. The masses of fermions (which were neglected earlier) can also be generated by the Higgs boson, if it couples to each of them with a strength proportional to its mass.

The couplings of the physical bosons can also be deduced by combining Equation 2.11 with Equation 2.6. Like the original $\boldsymbol{W}$ fields, the W only couples to left-handed fermions. Its coupling constant, g, is related to the Fermi constant for low energy weak interactions (G_F) by

$$\frac{G_F}{\sqrt{2}} = \frac{g^2}{8M_W^2}. \tag{2.12}$$

The photon, like the original B^μ field, couples equally to left- and right-handed fermions. The fermion-photon coupling strength (e) is known from QED. In terms of electroweak parameters, this is given by

$$e = g\sin\theta_W = g'\cos\theta_W. \tag{2.13}$$

The Z, like the photon, couples to both left- and right-handed fermions, but with a different strength to each. This is sometimes expressed as differences between vector and axial couplings of the Z. Expressed in terms of a fermion's charge (Q) and third component of isospin (I_3, which is zero for right-handed fermions), the Z boson's coupling to fermions is given by

$$c_Z = I_3 - Q\sin^2\theta_W. \tag{2.14}$$

Table 2.2: Summary of the fermion couplings to photon (Q), W (I_3) and Z (c_Z, defined in Equation 2.14) bosons in the standard electroweak model.

Particle	Q	I_3	c_Z
ν_l	0	1/2	$\frac{1}{2}$
ℓ_{L}	-1	-1/2	$-\frac{1}{2} + \sin^2\theta_W$
u_{L}	2/3	1/2	$\frac{1}{2} - \frac{2}{3}\sin^2\theta_W$
d_{L}	-1/3	-1/2	$-\frac{1}{2} + \frac{1}{3}\sin^2\theta_W$
ℓ_{R}	-1	0	$\sin^2\theta_W$
u_{R}	2/3	0	$-\frac{2}{3}\sin^2\theta_W$
d_{R}	-1/3	0	$\frac{1}{3}\sin^2\theta_W$

Table 2.3: Experimental measurements of the principal electroweak parameters. An explanation of how these parameters are obtained is given in [15].

Quantity	Value	Uncertainty
M_Z	91.1876 GeV/c^2	2.1 MeV/c^2
M_W	80.398 GeV/c^2	25 MeV/c^2
$\sin^2\theta_W$	0.23119	1.4×10^{-4}
$G_F/(\hbar c^3)$	1.16637×10^{-5} GeV^{-2}	1×10^{-10} GeV^{-2}
M_t	171.3 GeV/c^2	1.6 GeV/c^2

The electroweak couplings of fermions are summarised in Table 2.2.

Some of the most precise measurements of the electroweak sector have been made in the e^+e^- colliders at the Large Electron-Positron Collider and the Stanford Linear Collider. In these experiments, Z/γ^* and W bosons were produced and measured with minimal backgrounds from other processes. Their final results have been combined with recent measurements of boson production at the Tevatron [13, 14] not only to test the accuracy of the Standard Model but to place important constraints on the mass of the SM Higgs boson, which has not yet been discovered. Some of the important electroweak parameters have been summarised in Table 2.3.

2.1.2 The theory of strong interactions

The strong nuclear force is described in the Standard Model by the theory of *Quantum Chromodynamics*, or QCD. The theory arose from the original quark models of the 1960's [16, 17], with further additions as more massive quarks were discovered. The

basic symmetry group of QCD is SU(3). This symmetry remains unbroken in nature, meaning that gluons are massless, like the photon.

The symmetry group SU(3), which describes QCD, has eight generators, collectively referred to as $\boldsymbol{T}$. These correspond directly to the eight gluons of the theory, while the three dimensions mean that the theory involves three charges, called *colour*. Therefore, the elements of $\boldsymbol{T}$, denoted T_a, are conventionally represented as 3×3 matrices in colour space.[5] As with the elements of $\boldsymbol{I}$ in SU(2), these elements do not commute:

$$[T_a, T_b] = \mathrm{i} f_{abc} T_c. \tag{2.15}$$

Here, f_{abc} denotes one element of a $3 \times 3 \times 3$ array of structure constants, the values of which depend on the particular representation used.

The quark fields ψ_q are SU(3) triplets, which transform under a rotation in colour space:

$$\psi_q \rightarrow \exp\left[-\mathrm{i} g_s \boldsymbol{T} \cdot \boldsymbol{\theta}(x)\right] \psi_q, \tag{2.16}$$

whilst the leptons are colour singlets, and their fields are unaffected by this rotation.

As before, the transformation in Equation 2.16 modifies the free-fermion Lagrangian. Invariance can be achieved by the introduction of an eight-component vector boson field $\boldsymbol{G}$. In the perturbative limit, these fields transform as follows:

$$G_{a\mu} \rightarrow G_{a\mu} + \partial_\mu \theta_a(x) + g_s f_{abc} \theta_b(x) G_{c\mu}. \tag{2.17}$$

As in electroweak theory, an appropriate covariant derivative must be introduced:

$$\mathscr{D}_\mu = \partial_\mu + \mathrm{i} g_s \boldsymbol{T} \cdot \boldsymbol{G}_\mu. \tag{2.18}$$

The QCD Lagrangian can then be written:

$$\mathscr{L}_{\mathrm{QCD}} = \mathrm{i}\psi_q^\dagger \gamma^\mu \mathscr{D}_\mu \psi_q - m_q \psi_q^\dagger \psi_q - \frac{1}{4} \boldsymbol{G}_{\mu\nu} \cdot \boldsymbol{G}^{\mu\nu}. \tag{2.19}$$

As with Equations 2.3 and 2.6, the first two terms are to be summed over all quark flavours.

The gluon kinetic tensor $\boldsymbol{G}^{\mu\nu}$ has a similar form to Equation 2.7:

$$G_{a\mu\nu} = \partial_\mu G_{a\nu} - \partial_\nu G_{a\mu} - g_s f_{abc} G_{b\mu} G_{c\nu}. \tag{2.20}$$

[5] The indices a, b, c will always refer to the gluon index $1, \ldots 8$, not the colour index. The trace of the product of two colour matrices is denoted by $\boldsymbol{A} \cdot \boldsymbol{B} = A_a B_a$.

Again, the non-Abelian nature of this interaction gives rise to a self-coupling term, meaning that gluons will couple to gluons. This has some important consequences for QCD phenomenology, which will be examined next.

Running coupling and confinement

Despite the complexity of colour indices, the theory behind the strong interaction bears similarities to the electroweak theory before symmetry breaking. In terms of phenomenology however, the strong force has a unique behaviour, not least because it leads to the formation of closely bound hadrons. The coupling strength of the strong force is usually quoted in terms of the rationalised coupling constant $\alpha_s = g_s^2/4\pi$, which is of the order of a few times 10^{-1} at low energies $\mathcal{O}(\text{GeV})$. This contrasts sharply with the electroweak coupling constant α, which has a value around $1/137$ at low energies.

It is necessary to quote energy scales with the values of α and α_s because the creation of virtual $f\overline{f}$ pairs around a charged (in the most general sense of the word) particle modifies the effective boson field strength around that particle. This is often called vacuum polarisation. In the Abelian theory of QED, this polarisation screens the electric charge of a target particle from a hypothetical probe. Thus, as the collision energy increases and the probe resolves the target better, it experiences more of the target's electric charge, and the effective value of α increases. In QCD, a similar effect occurs, but the gluon self-coupling reverses the effect. Thus, α_s decreases as a function of collision energy, an effect which has been measured experimentally as illustrated in Figure 2.1.

The variation of α_s with energy scale μ is given by (*cf* [15], Chapter 9)

$$\mu\frac{\partial\alpha_s(\mu)}{\partial\mu} = -\frac{11-\frac{2}{3}n_f}{2\pi}\alpha_s^2(\mu) - \mathcal{O}(\alpha_s^3(\mu)), \tag{2.21}$$

where n_f is the number of quark flavours with $m_q < \mu$. Within the SM, $n_f \leq 6$ for all μ, so the leading term in Equation 2.21 is always negative. This has two important consequences: asymptotic freedom and quark confinement.

Asymptotic freedom is the statement that $\alpha_s \to 0$ as $\mu \to \infty$. In other words, as quark collision energies increase, they behave more and more like free particles. This means that perturbation theory can be applied to high energy QCD collisions, but not

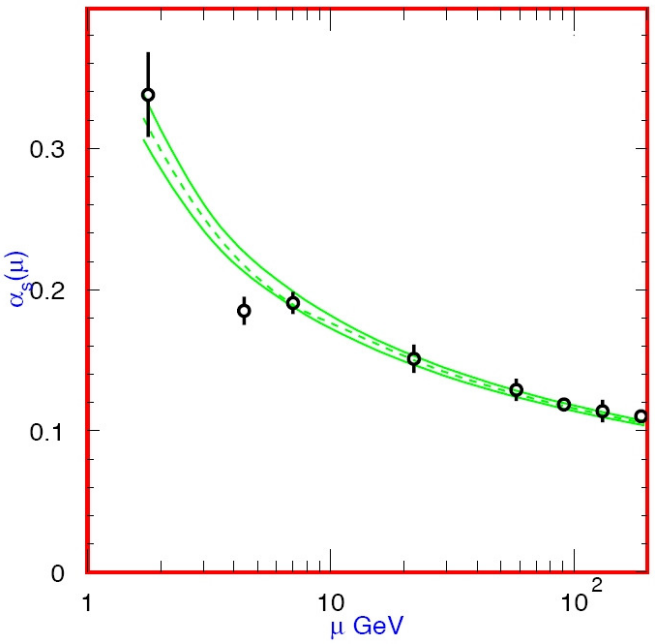

Figure 2.1: Measurements of α_s as a function of the energy scale μ. The lines show the Particle Data Group's average and $\pm 1\sigma$ limits (from [15], Chapter 9).

to low energy QCD interactions.

Quark confinement refers to the observation that no objects with a net colour charge have ever been seen. As the gluon is massless, one would naïvely expect the strong force to have an infinite range, and colour-charged objects to be as common as electrically charged ones. However, μ is small in long-range interactions, and therefore α_s is very large. In order to escape from a hadron, any colour-charged object (*eg* a quark) would have to develop so much potential energy that there would be enough energy in the gluon field to produce $q\overline{q}$ pairs in the intervening space. These would then be free to form hadrons with both the escaping quark and the hadron remnant, in a process called *hadronisation*. Thus, no finite amount of energy can liberate a free quark or gluon, and they are confined to exist as the constituents of mesons and baryons.

2.2 Vector boson production at hadron colliders

In high energy proton colliders, such as the LHC, quark-antiquark collisions can produce real Z bosons, *ie* bosons which are on the mass shell. The dominant production channel

for this is the Drell-Yan process [18]:

$$q\overline{q} \rightarrow Z/\gamma^* \rightarrow f\overline{f}. \tag{2.22}$$

In the intermediate state, there is interference from off-shell photons (γ^*), as the two gauge bosons share the same quantum numbers (if this were not the case, the mixing of Equation 2.11 would not be possible). Although the proton is a matter particle, the Drell-Yan process is possible in pp collisions due to the presence of the parton "sea". This sea consists of quarks, antiquarks and gluons, each typically carrying only a small fraction of the proton's momentum, constantly being created and destroyed through strong interactions.

An important parameter for proton colliders is the square of the centre of mass energy, s. However, the energy available for the intermediate state in Drell-Yan production is less, because the quarks do not carry the full proton momentum. If the colliding partons carry fractions x_1 and x_2 of the respective protons' momenta, then the invariant mass squared of the $q\overline{q}$ system is

$$\hat{s} = x_1 x_2 s. \tag{2.23}$$

For on-shell Z production, $\hat{s} \approx M_Z^2$. Thus, the x values for this process will be small at the LHC, typically around $M_Z/14$ TeV $= 6.5 \times 10^{-3}$.

The cross section for the parton-level process in Equation 2.22 can be calculated using electroweak theory. QCD effects also need to be considered because quarks are involved. However, α_s is small at high energy scales (*cf* Figure 2.1), and so a perturbative expansion in powers of α_s can be made. At the partonic level, the leading term, with no additional QCD interactions, is (*cf* [19], Equation 10.17):

$$\hat{\sigma}_{q\overline{q}\rightarrow Z}(\hat{s}) = \frac{2\pi\sqrt{2}}{3} M_Z^2 G_F \left[(c_Z^{q_\mathrm{L}})^2 + (c_Z^{q_\mathrm{R}})^2\right] \delta(\hat{s} - M_Z^2). \tag{2.24}$$

Note that the decay width of the Z (Γ_Z) and all photon terms have been neglected.

The probability of finding a quark (or antiquark) with momentum fraction x is described by a *parton density function*, or *pdf*, denoted $f_q(x, \mu_F)$. These depend on an energy scale, μ_F, called the factorisation scale. The value of this scale is not fixed by the theory, although it is usually chosen to be near a characteristic energy or momentum

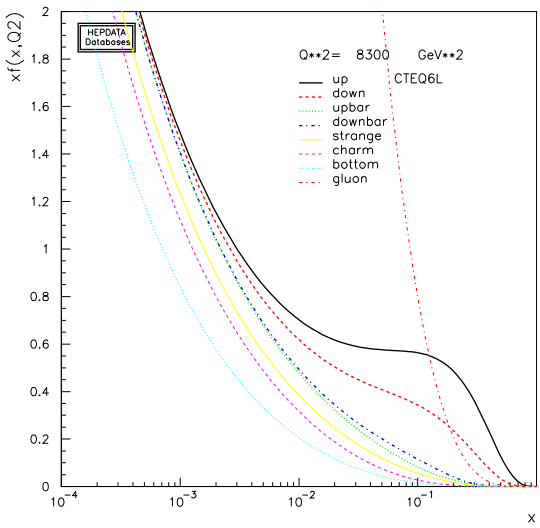

Figure 2.2: Parton density functions (*pdf*s) as a function of Björken x, at a constant $\mu_F = M_Z^2$, according to the fits of the CTEQ collaboration [24].

scale of the process (for example, M_Z). One particular set of *pdf* parameterisations, by the CTEQ collaboration, is shown in Figure 2.2. The valence quark contributions to the proton's momentum can clearly be seen as bumps in the u and d *pdf*s, but at x values relevant for on-shell Z production at the LHC, the parton "sea" dominates, which contributes equally to the q and $\overline{q}$ distributions. The gluon distribution is many times larger than any of these, but does not contribute to the Drell-Yan process until higher order QCD corrections are considered.

The data used to constrain the *pdf* parameterisations come from many sources, including ep collisions at the HERA collider, various fixed target experiments, and Drell-Yan and jet data from the Tevatron. Recently, *pdf* parameterisations have been published by the CTEQ [20] and MSTW [21] groups. In addition, the HERA experiments have published their own *pdf* set with a full consideration of experimental systematic effects [22]. The DGLAP equations [23], on which the determination of the *pdf* parameterisations is based, also allows these results to be extrapolated to the higher-energy regions probed at the LHC.

To describe the total Z production cross section in pp collisions, Equation 2.24 or

its higher order equivalent needs to be convolved with the relevant *pdf*s to give:

$$\sigma_{pp\to Z} = \sum_q \int dx_1 dx_2 \left\{ f_q(x_1, \mu_F) f_{\overline{q}}(x_2, \mu_F) + f_q(x_2, \mu_F) f_{\overline{q}}(x_1, \mu_F) \right\} \hat{\sigma}_{q\overline{q}\to Z}(x_1 x_2 s). \tag{2.25}$$

This convolution relies on the factorisation theorem [25] in order to allow separation of the parton-level interaction and the description of the proton given by the *pdf*s. The Z production cross section therefore depends on the physical *pdf*s, and different *pdf* parameterisations predict different Z boson production rates at the LHC. The estimation of *pdf* uncertainties varies between different *pdf* sets, depending on the input data and model assumptions, but their impact on the Z/γ^* production cross section is typically in the range $1 - 3\%$ [26].

The dependence of Equation 2.25 on μ_F has no physical origin, but is rather an artifact of our inability to perform calculations to all perturbative orders in QCD. This dependence can be reduced by adding higher order QCD terms into Equation 2.24. This involves calculating α_s, and the energy scale at which this is done is referred to as the renormalisation scale μ_R. Typically, for Drell-Yan Z/γ^* boson production, μ_F and μ_R are chosen to be equal to each other and to either M_Z or $\hat{s}$ (which may not equal M_Z due to the finite width of the Z boson). This choice is not unique and is a source of theoretical systematic uncertainty, which again decreases as one adds further perturbative orders. Calculations have been performed up to Next-to-Next-to-Leading Order (NNLO) precision, with less than 1% residual uncertainty from the choice of scales [27]. When considering this level of precision, Next-to-Leading Order (NLO) electroweak effects also become relevant, and these have also been calculated for W and Z/γ^* production at the Tevatron and LHC [28, 29]. The implementation and interaction of QCD and QED corrections will be considered in Chapter 3.

In addition to the primary, "hard" interaction described by Equation 2.22, both the colliding and spectator partons undergo many "soft" QCD interactions during the course of a collision. These interactions must be treated with phenomenological models as the coupling is too strong for perturbative techniques to be applied. In addition, confinement requires that apparently bare quarks and gluons in the final state undergo hadronisation into colourless hadrons. Corrections for missing higher order QCD and

QED terms are added by models for both initial and final state radiation. These calculations form an essential part of the event generation process for accurate modelling of complete events as seen in high energy physics detectors, and dedicated *Monte Carlo* programs exist to model these effects in simulated physics events.

Two popular Monte Carlo programs are PYTHIA [30, 31] and HERWIG [32, 33]. These programs calculate hard processes to LO precision in α_s, but can in principle be used with more advanced fixed-order event generators simply to provide a description of the soft showering on top of the hard processes. There is however a need to avoid the double-counting of radiative effects when doing this, requiring dedicated matching routines between the two programs used. One example of a matched NLO matrix element calculation with a parton shower description is in the event generator MC@NLO [34]. In general, while fixed order calculations are expected to provide the best estimate of the total Z/γ^* production rate at the LHC, tuned Monte Carlo programs with soft QCD showers and hadronisation should provide a better description of the observable kinematic distributions. This is discussed further in the next chapter.

Chapter 3

Event generation for pp collisions and $Z/\gamma^* \rightarrow e^+e^-$ acceptance studies

In order to understand and predict the response of a high energy particle detector such as ATLAS, large numbers of simulated events need to be produced. In addition, Monte Carlo generated event samples are also used to extrapolate from the $Z/\gamma^* \rightarrow e^+e^-$ cross section measured within the detector acceptance to the total $Z/\gamma^* \rightarrow e^+e^-$ cross section. In this chapter, the generation of these events is addressed. Section 3.1 begins with a description of the simulated event samples used in this thesis. In the remaining sections, aspects of PYTHIA's physics model that affect the acceptance of $Z/\gamma^* \rightarrow e^+e^-$ events are studied and the uncertainty on this acceptance is estimated. The chapter finishes with a discussion on the factorisation of the different processes included in PYTHIA's physics model, in Section 3.4, which impacts on what methods can reliably be used to estimate acceptance corrections and their uncertainties.

3.1 Monte Carlo generators

A number of different Monte Carlo generators are used to produce simulated events for signal and background processes relevant to the analysis in this thesis. These provide matrix element calculations for inclusive processes, up to a specified order in α_s or α, usually Leading Order (LO). All of the generated samples used to study detector effects include hadronisation and soft QCD effects such as parton showering. In addition, the underlying event is modelled using parameters which are tuned based on published

data from the Tevatron and other sources [35].[6] Issues relating to "pile-up" (multiple hard interactions ocurring in a single bunch crossing) have been neglected, as they are less important in early data when the instantaneous luminosity is still low. Once the event generation is complete to the hadron level, the simulation of an event is passed on to GEANT 4 which models the detector itself. All of this is managed within the ATLAS software framework ATHENA, described in Chapter 6.

The simulated datasets used in this thesis have been produced with two different generators. Most events have been produced using PYTHIA 6.4 [31]. This generator includes Leading Order matrix elements, and simulates initial and final state QCD radiation as well as the underlying event and hadronisation. This version of PYTHIA models the multiple interactions associated with the spectator partons and the initial state radiation in a consistent manner, and includes parton showers which are ordered by the parton's momenta. Both of these developments, described in [36], allow a more realistic description of initial and final state QCD radiation. Final state photon (*ie* QED) radiation is calculated using PHOTOS [37, 38], while decays of τ leptons are handled using the dedicated TAUOLA package [39, 40].

Events were also generated using the MC@NLO generator [34]. This produces a fixed-order parton-level calculation at Next-to-Leading Order (NLO) in α_s. Hadronisation in this case is modelled by HERWIG [32, 33], while the underlying event is produced using JIMMY [41]. PHOTOS and TAUOLA are used for final state photon radiation and τ decays, exactly as with PYTHIA.

All events have been generated using the CTEQ6L1 (with PYTHIA) and CTEQ6M (with MC@NLO) parameterisations for the parton density functions [24]. The former *pdf* parameterisation is designed for Leading Order calculations, and uses the LO value for α_s ($\alpha_s(M_Z) = 0.130$), while the latter parameterisation is made for calculations up to NLO and uses the NLO value for α_s ($\alpha_s(M_Z) = 0.118$).

Table 3.1: Description of Monte Carlo samples used in this thesis. The columns list the generator used to produce each sample, the cross section output by each generator, the efficiency of filters applied on the final state particles, and the equivalent integrated luminosity of the available simulated samples. See the text for a description of the filters and physics content of each sample. More details on the cross sections at $\sqrt{s} = 14$ TeV are available in [42].

$\sqrt{s} = 14$ TeV Process	Generator	σ [nb]	ϵ_{F}	$\int \mathcal{L}dt$ [pb^{-1}]
$Z/\gamma^* \to e^+e^-$	PYTHIA	1.66	0.84	152
Filtered events	PYTHIA	2.4×10^6	0.08	0.087

$\sqrt{s} = 10$ TeV Process	Generator	σ [nb]	ϵ_{F}	$\int \mathcal{L}dt$ [pb^{-1}]
$Z/\gamma^* \to e^+e^-$	PYTHIA	1.144	0.96	4490
$Z/\gamma^* \to e^+e^-$	MC@NLO	1.357	0.96	3050
Filtered events	PYTHIA	1.46×10^6	0.071	0.093
$t\bar{t}$	MC@NLO	0.3736	0.54	9810
$W \to e\nu_e$	PYTHIA	11.76	0.88	465
$W \to \tau\nu_\tau$	PYTHIA	4.184	0.87	106
$Z/\gamma^* \to \tau^+\tau^-$	PYTHIA	1.128	1	531

3.1.1 Generated samples

Results are presented in this thesis for pp collisions at two centre of mass (CM) energies: 14 TeV, the design CM energy of the LHC, and 10 TeV, a reduced CM energy which may be used for early collisions. The simulated datasets used are listed in Table 3.1, along with details of the event generation which preceeds the detector simulation. In almost all cases, a filter is applied between event generation and simulation, to avoid the time-consuming simulation of events which are unlikely to result in the reconstructed objects (*eg* electrons) which are of interest.[7] To avoid biasing the resulting simulated events, the filter criteria are typically chosen so that only events where final state electrons fall well outside the Inner Detector acceptance are rejected. The main exception is in the filtered event sample, as discussed below. The efficiencies of these filters (denoted ϵ_{F})

[6] The underlying event describes the soft interactions between the "spectator" partons not directly involved in the high-Q^2 collision.

[7] Some of the filters apply cuts on a particle's *transverse momentum* (p_{T}) and/or *pseudorapidity* (η). The p_{T} of a particle is the component of its momentum perpendicular to the beam direction. Pseudorapidity is defined in terms of the polar angle θ between the particle's trajectory and the beam direction as $\eta = -\ln\tan(\theta/2)$. See also Section 4.2.

are included in Table 3.1. The processes used in these datasets, and the filters applied, will now be discussed.

The $Z/\gamma^* \rightarrow e^+e^-$ signal

The primary signal sample used for this thesis consists of $Z/\gamma^* \rightarrow e^+e^-$ events simulated using PYTHIA. These samples (one each at $\sqrt{s} = 10$ and 14 TeV) include events where the intermediary boson is an off-shell photon, as well as Z/γ^* interference effects. A lower mass limit of 60 GeV/c^2 is imposed on the exchanged boson, to remove the low mass Drell-Yan component. This requirement is included in the listed cross sections of Table 3.1. In Chapter 9, a second 10 TeV signal sample is used, generated using MC@NLO. This sample also includes off-shell photon production, with the same cut of $M_{Z/\gamma^*} > 60$ GeV/c^2.

All of the signal samples apply a filter to the final state leptons in each event, with cuts that vary with $\sqrt{s}$. In the 14 TeV sample, at least one electron in the event is required to have $p_{\mathrm{T}} > 10$ GeV/c and $|\eta| < 2.7$. In the 10 TeV samples, one electron of any p_{T} is required to have $|\eta| < 2.8$. The efficiencies of these filters are given in Table 3.1.

Filtered event sample

QCD jet events are the dominant background to $Z/\gamma^* \rightarrow e^+e^-$ events. This sample contains all QCD processes where the p_{T} of the hard scatter is greater than 15 GeV/c, including heavy flavour production. It also contains other processes which will lead to reconstructed electrons or photons, such as prompt photon, $t\bar{t}$, W and Z/γ^* production. As the sample contains many event types, and not just QCD jet events, it shall be referred to simply as the "filtered event" sample, after the filter described below. Filtered event samples have been produced at both CM energies of 10 and 14 TeV.

The vast majority of QCD-mediated events produce jets which are either too diffuse or have too low an energy to be misreconstructed as high p_{T} electrons or photons. The filter applied to this sample aims to remove some of these events at the generator level, to reduce the overall simulation time. This is achieved by selecting on the p_{T} sum within $\eta - \phi$ windows of size $\Delta\eta \times \Delta\phi = 0.12 \times 0.12$. If one such window within $|\eta| < 2.7$

contains stable particles (excluding muons and neutrinos) whose p_{T} sums to at least 17 GeV/c, the event is kept. This filter has the potential to bias the reconstructed electron spectrum, although tests indicate that this bias is negligible for reconstructed electrons with $p_{\mathrm{T}} > 20$ GeV/c, increasing to approximately 30% for electrons with $p_{\mathrm{T}} = 15$ GeV/c.

Even with this filter and the large number of events generated (almost 9.6 million events after filtering at $\sqrt{s} = 14$ TeV), the size of the jet cross section means that the filtered event samples still correspond to a very small integrated luminosity (< 0.1 pb^{-1}) compared to the signal sample and the other backgrounds. A method for improving the effective statistics of this sample, involving a detailed study of its properties, will be presented in Chapter 7.

Top quark production

Top quark pair production is expected to form an important background to $Z/\gamma^* \rightarrow e^+e^-$ events, due to the large $t\bar{t}$ cross section at the LHC and the presence of decay modes involving two high p_{T} electrons in the final state. $t\bar{t}$ events have been generated using MC@NLO, and the cross section quoted in Table 3.1 is for inclusive $t\bar{t}$ production, calculated to NLO precision.

Decays of the top quark can be grouped into two types: hadronic ($t \rightarrow bW \rightarrow bq\overline{q}'$) and leptonic ($t \rightarrow bW \rightarrow b\ell\nu$, $\ell = e, \mu, \tau$). Events where both top quarks decay hadronically are not expected to contribute significantly to this background. The filter on this sample therefore only accepts all semi- and fully-leptonic decay modes.

Electroweak backgrounds

Further backgrounds considered in this analysis arise from decays of the W and Z bosons (excluding $Z/\gamma^* \rightarrow e^+e^-$). Only certain decay modes have been considered, limited to $W \rightarrow e\nu_e$, $W \rightarrow \tau\nu_\tau$ and $Z/\gamma^* \rightarrow \tau^+\tau^-$. Tau leptons are included because they can decay to electrons, but also because hadrons from many τ decays (*eg* $\tau^\pm \rightarrow \pi^\pm\nu_\tau$) can be misidentified as electrons. All of these samples have been simulated using PYTHIA.

The simulated $Z/\gamma^* \rightarrow \tau^+\tau^-$ events have the same requirement on the Z/γ^* mass

of $M_{Z/\gamma^*} > 60$ GeV/c^2 as the signal. Unlike the signal, there is no filter on the final state particle kinematics.

For the $W \to \tau\nu_\tau$ decay mode, the tau lepton is forced to decay to either an electron or a muon. These branching fractions are included in the cross section listed in Table 3.1. Both W samples contain a filter requiring at least one final state electron or muon with $|\eta| < 2.8$.

3.2 Cross section prediction and acceptance correction

The primary aim of this thesis is to study the measurement of the total $Z/\gamma^* \to e^+e^-$ production cross section ($\sigma_{Z/\gamma^* \to e^+e^-}$) in early data. This will be done by selecting events in ATLAS with two reconstructed electron candidates passing some cut criteria within a certain kinematic region. This region in phase space is defined by cuts on each lepton's pseudorapidity and p_{T}, as well as on the invariant mass of the pair, M_{ee}. These cuts are principally motivated by experimental concerns, such as the detector geometry, electron triggering requirements and reduction of backgrounds. A cut on M_{ee} also restricts attention to the region of on-shell Z boson production, away from the region dominated by low mass Drell-Yan production.

Assuming that N $Z/\gamma^* \to e^+e^-$ candidate events have been observed once an integrated luminosity of $\mathrm{L} = \int \mathcal{L}dt$ has been collected, the total cross section may be measured by applying a number of corrections to N:

$$\sigma_{Z/\gamma^* \to e^+e^-} = \frac{N - B}{\mathcal{A}\mathcal{S}\epsilon\mathrm{L}}. \tag{3.1}$$

The corrections include backgrounds (B), detector and trigger efficiencies (ϵ), resolution effects ($\mathcal{S}$), and acceptance ($\mathcal{A}$). Backgrounds are discussed further in Chapter 7, while efficiency determination is the subject of Chapter 8. It is assumed that the product $\mathcal{S}\epsilon$ describes the known experimental effects, such that $\mathcal{A}$ is a purely theoretical quantity, with purely theoretical uncertainties. Physically, $\mathcal{A}$ is an extrapolation factor, into the unmeasured regions of phase space.

In Chapter 9, the measurement of $\sigma^{\mathrm{kin}}_{Z/\gamma^* \to e^+e^-} = (N - B)/(\mathcal{S}\epsilon\mathrm{L})$ is also considered, that is, the cross section without the phase space extrapolation. Both measurements are of interest. The "kinematic" cross section $\sigma^{\mathrm{kin}}_{Z/\gamma^* \to e^+e^-}$ will not suffer from the the-

oretical uncertainties present in $\mathcal{A}$, whilst the total cross section $\sigma_{Z/\gamma^* \to e^+e^-}$ is directly comparable with theoretical calculations, as it does not depend upon a particular set of kinematic cuts. For the measurement of $\sigma_{Z/\gamma^* \to e^+e^-}$, it is necessary to consider the acceptance $\mathcal{A}$ and its theoretical uncertainties.

These uncertainties arise from various theoretical effects. First of all, calculations at Leading Order precision (in α_s) are known to be subject to additional QCD corrections [43]. Therefore higher order calculations need to be considered. The highest order calculations currently available are up to NNLO (Next-to-Next-to-Leading Order) in α_s [27] and up to NLO for electroweak effects [29]. In addition, the choice of parton density function (*pdf*) needs to be considered. These have been studied elsewhere [44]. In this chapter, a study into the importance of various non-perturbative QCD effects is presented, whilst NLO QED effects are also considered.

3.2.1 Sample production

The PYTHIA generator has been used to examine factors which affect the acceptance of $Z/\gamma^* \to e^+e^-$ events in ATLAS [31]. This is a Leading Order generator, which calculates just the first matrix element in the perturbative expansion in α_s. It also models various non-perturbative processes which influence the final state particle distributions, and hence $\mathcal{A}$. These include:

- QCD Initial State Radiation (ISR)
- "Primordial" parton k_{T} (an intrinsic parton transverse momentum)
- Final State Radiation (FSR), predominantly of photons (modelled by PHOTOS)
- Parton Showers (PS), hadronisation, and multiple interactions

These processes will collectively be called *additional PYTHIA processes* in what follows. An event sample produced with all of these processes included will be referred to as "Full PYTHIA", while a sample produced with none of these processes present is called "PYTHIA LO". Other samples, with some but not all of the above processes present, will be labelled with respect to these two extremes. For example, the label "Full

PYTHIA − ISR" will mean that a sample was generated with everything present except ISR.

Events have been generated for pp collisions with $\sqrt{s} = 14$ TeV using the ATLAS software framework, which interfaces with PYTHIA and other event generators. The generator settings used for the 14 TeV $Z/\gamma^* \to e^+e^-$ sample in Table 3.1 were used as a starting point, including the cut of $M_{Z/\gamma^*} > 60$ GeV/c^2, the choice of *pdf* (CTEQ6L1 [24]) and the tuned parameters describing the underlying event. However, the lepton filter described in Section 3.1.1 was removed to make these samples fully inclusive. All other settings were left unchanged, except where explicitly stated.

Figure 3.1 compares some kinematic distributions in the "Full PYTHIA" and "PYTHIA LO" samples. At Leading Order, the boson acquires no transverse momentum, and the lepton p_{T} spectrum shows a clear Jacobian peak. Also, the di-electron mass is equal to the boson mass. When the additional PYTHIA processes are present, the boson often has significant p_{T}. Additionally, the lepton p_{T} spectrum is smeared with respect to "PYTHIA LO", and the η distribution is more central. Finally, the di-electron mass is reduced from the boson mass due to radiative effects.

The final selection criteria used in a $Z/\gamma^* \to e^+e^-$ analysis will depend on the trigger menu used during the relevant data-taking periods. As the final menus are not yet known, a nominal p_{T} acceptance cut of $p_{\mathrm{T}}^{\mathrm{e}} > 20$ GeV/c has been chosen for these studies. Also, a pseudorapidity cut of $|\eta^e| < 2.5$ has been used, motivated by the acceptance of the Inner Detector (*cf* Section 4.3). The implications of an additional cut on the di-electron mass are discussed in Section 3.3.4.

3.3 Acceptance uncertainty

In this section, several variations of the PYTHIA model parameters are explored, together with their effect on the generated events. Table 3.2 gives the acceptance related to the cuts applied on the electron p_{T} and $|\eta|$, individually and combined. The table is split into two parts. In the top half, each PYTHIA process is added into the "PYTHIA LO" calculation, while in the bottom half the same processes are removed from the "Full PYTHIA" configuration. Note that the processes are added and subtracted

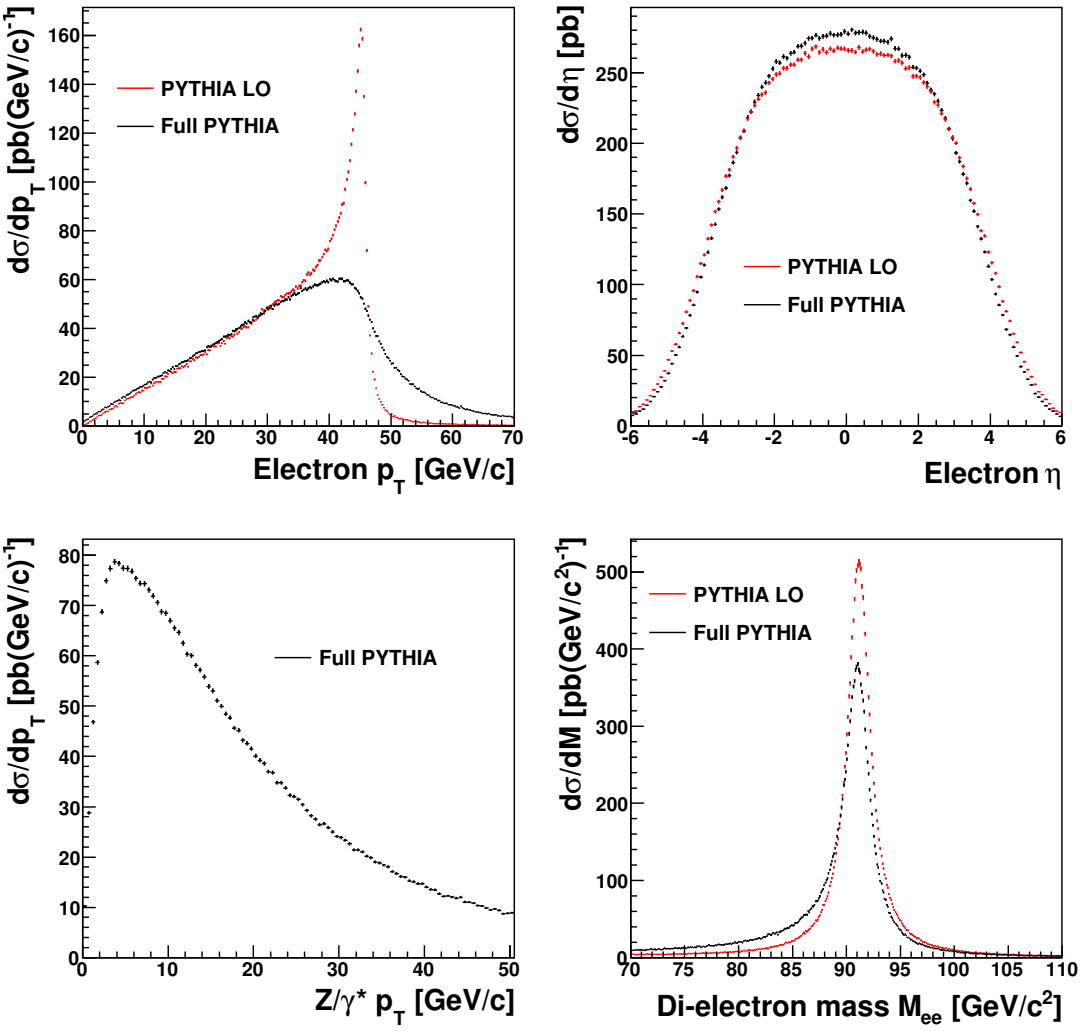

Figure 3.1: Comparison of $Z/\gamma^* \to e^+e^-$ events generated at LO with and without additional PYTHIA processes. Top left: electron p_{T}. Top right: electron pseudorapidity. Bottom left: Z/γ^* boson p_{T} (which is identically 0 for "PYTHIA LO"). Bottom right: M_{ee}.

individually, not sequentially.

Table 3.2 shows that the overall acceptance of the combined p_{T} and $|\eta|$ cuts is approximately 40%. Of the two cuts, the $|\eta|$ cut is the more significant as it removes more than half of the sample on its own. By contrast, the acceptance of the p_{T} cut applied on its own is in the range of $75 - 85\%$.

The acceptance for the "Full PYTHIA" sample is almost 2.5% lower than the "PYTHIA LO" sample. This appears to be the result of a balance between a 2.8% increase in the acceptance of the $|\eta|$ cut, and more than a 10% drop in the p_{T} cut acceptance.

Table 3.2: Acceptance values of $Z/\gamma^* \to e^+e^-$ events under several variations of the physics model. Acceptances are shown separately for the p_{T} cut and the $|\eta|$ cut, and for both combined. Each PYTHIA process variation is applied individually, not consecutively.

Sample	$p_{\mathrm{T}}^{\mathrm{e}} > 20$ GeV/c	$\lvert\eta^e\rvert < 2.5$	$p_{\mathrm{T}}^{\mathrm{e}} > 20$ GeV/c and $\lvert\eta^e\rvert < 2.5$
Relative to PYTHIA LO			
Default	$85.20 \pm 0.04\%$	$44.43 \pm 0.05\%$	$42.11 \pm 0.05\%$
+ FSR	$80.31 \pm 0.04\%$	$44.55 \pm 0.05\%$	$40.10 \pm 0.05\%$
+ PS	$85.20 \pm 0.04\%$	$44.52 \pm 0.05\%$	$42.18 \pm 0.05\%$
+ k_{T}	$84.06 \pm 0.04\%$	$44.52 \pm 0.05\%$	$41.82 \pm 0.05\%$
+ ISR	$78.60 \pm 0.04\%$	$47.26 \pm 0.05\%$	$41.72 \pm 0.05\%$
Relative to Full PYTHIA			
Default	$74.40 \pm 0.04\%$	$47.27 \pm 0.05\%$	$39.64 \pm 0.05\%$
- FSR	$78.62 \pm 0.04\%$	$47.34 \pm 0.05\%$	$41.73 \pm 0.05\%$
- PS	$74.42 \pm 0.04\%$	$47.28 \pm 0.05\%$	$39.71 \pm 0.05\%$
- k_{T}	$74.44 \pm 0.04\%$	$47.29 \pm 0.05\%$	$39.69 \pm 0.05\%$
- ISR	$79.37 \pm 0.04\%$	$44.60 \pm 0.05\%$	$39.81 \pm 0.05\%$

The variation in the acceptance of the $|\eta|$ cut appears to be entirely due to ISR, with the other PYTHIA processes having little impact on the $|\eta|$ cut acceptance. The sensitivity of the p_{T} cut acceptance is more complex, with apparent contributions from ISR, FSR and the primordial k_{T}.

A quantitative analysis of Table 3.2 shows that the effects on the acceptance due to the different PYTHIA processes do not factorise, meaning that the impact of some processes depends on the presence or absence of the others. For example, adding in primordial k_{T} to "PYTHIA LO" decreases the acceptance of the p_{T} cut by more than 1.1%, but removing it from "Full PYTHIA" where other processes like ISR are present leaves the p_{T} cut acceptance unchanged within statistical uncertainties. This issue, and its possible impact on acceptance calculations, will be discussed further in Section 3.4. First, the individual PYTHIA processes will be examined in more detail.

3.3.1 QCD radiation in the initial state

The effects of initial state radiation (ISR) are shown in Figure 3.2. In the upper plot, the $p_{\mathrm{T}}^{\mathrm{Z}}$ distribution can be seen, showing the contribution solely from ISR ("LO+ISR") and

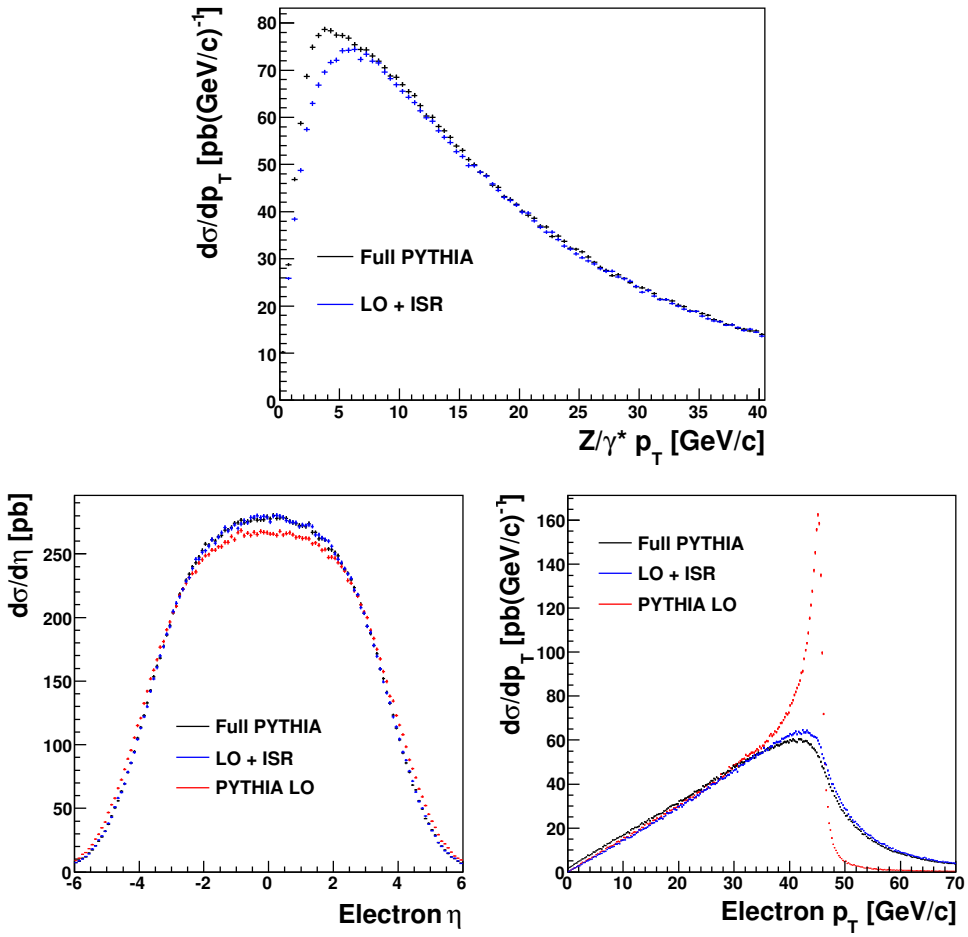

Figure 3.2: Illustration of the principal effects of QCD initial state radiation. Top: Z/γ^* boson p_{T}. Bottom left: electron η. Bottom right: electron p_{T}.

from all PYTHIA processes together ("Full PYTHIA"). At large values of $p_{\mathrm{T}}^{\mathrm{Z}}$, the two curves converge, indicating that ISR is responsible for imparting the boson with large amounts of p_{T} in these events. Indeed, PYTHIA's ISR model partially compensates for the lack of higher order QCD terms in the matrix element calculation.

The apparent lack of events at low $p_{\mathrm{T}}^{\mathrm{Z}}$ in the "LO+ISR" case is due to the fact that approximately 3% of events do not undergo ISR. When ISR is the only PYTHIA process included, the Z/γ^* boson in these events has no transverse momentum, and does not appear in this plot. The addition of the other processes in "Full PYTHIA" causes these events to populate the low $p_{\mathrm{T}}^{\mathrm{Z}}$ bins. As will be seen in Section 3.3.2, this migration is caused by the inclusion of primordial k_{T}.

ISR strongly affects the lepton distributions too, increasing their centrality in η

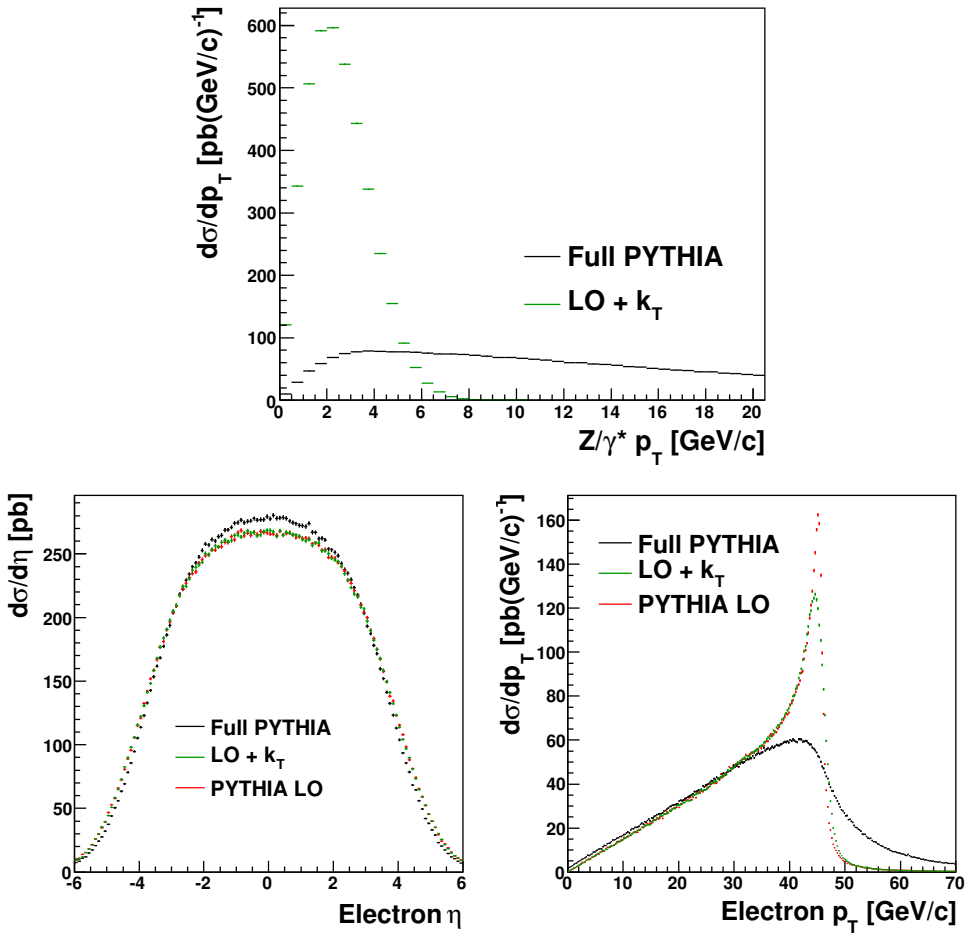

Figure 3.3: Illustration of the principal effects of primordial parton k_{T}. Top: Z/γ^* boson p_{T}. Bottom left: electron η. Bottom right: electron p_{T}.

while smearing out the sharp Jacobian peak present in the "PYTHIA LO" electron p_{T} spectrum. The electrons are no longer back-to-back in ϕ, and need not have identical p_{T} values. Thus, the acceptance for the electron p_{T} cut decreases by almost 7% with respect to "PYTHIA LO", while the acceptance of the $|\eta|$ cut increases by almost 3%. This partial cancellation results in a modest change in the acceptance of less than 1% when both cuts are applied.

3.3.2 Primordial parton k_{T}

The "primordial" k_{T} is the intrinsic transverse motion of partons inside the proton. This models motion attributable to the Pauli uncertainty principle, and also other poorly understood elements of low energy shower evolution [31, Section 11.3.3]. By default, the primordial k_{T} is modelled using a Gaussian distribution with a width of

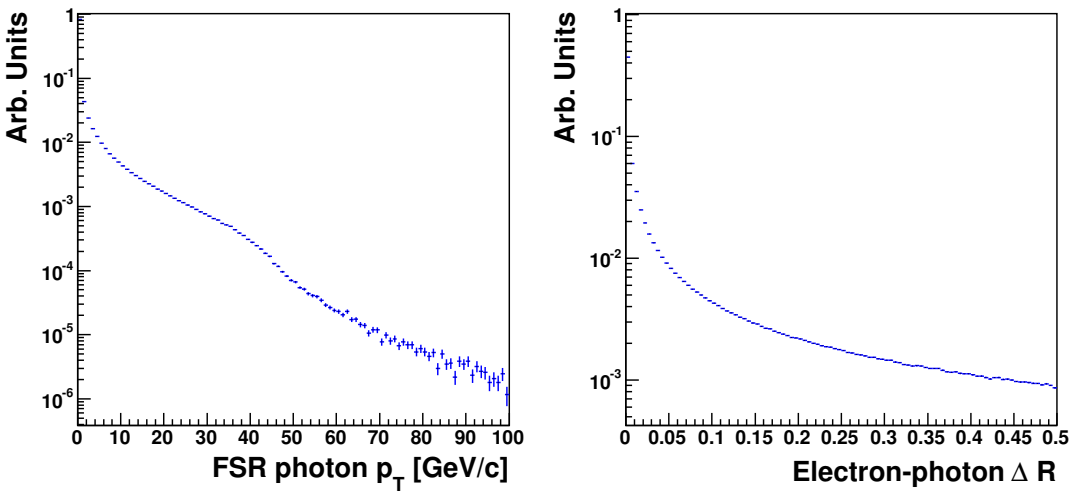

Figure 3.4: Characteristic distributions of final state photon radiation as modeled by PHOTOS. Left: photon p_{T}. Right: $\Delta R_{e\gamma}$ between final state electrons and photons.

2 GeV/c.

Figure 3.3 shows the effect that the primordial k_{T} has on the boson and lepton kinematic distributions. The top panel shows the boson p_{T}. Compared to the effect of ISR on $p_{\mathrm{T}}^{\mathrm{Z}}$, the impact of primordial k_{T} is relatively minor. In the lower panels, it can be seen that the lepton centrality is barely affected by the primordial k_{T}, although it slightly smears the Jacobian peak in $p_{\mathrm{T}}^{\mathrm{e}}$ when it is the only PYTHIA process present. The effect of primordial k_{T} on the acceptance is small when both p_{T} and $|\eta|$ cuts are applied, as was seen in Table 3.2.

3.3.3 Parton showers, hadronisation and multiple interactions

A number of further processes included in PYTHIA modify the hadronic final state, including multiple interactions, parton showers and hadronisation. Whilst these processes are expected to modify the details of, for example, the hadronic final state, they were found to have no appreciable effect on the kinematics of the Z/γ^* boson or its leptonic decay products. For completeness, parton showers are included in Table 3.2 and the following tables, but these processes will not be considered further.

3.3.4 Photon radiation in the final state

At the LHC, electroweak corrections can affect the Z/γ^* production cross section (with cuts) at the few percent level [29]. Whilst smaller than NLO QCD effects, these are

Table 3.3: Acceptance values of $Z/\gamma^* \to e^+e^-$ events, where final state photons are recombined with final state electrons if $\Delta R_{e\gamma} < 0.05$. The acceptances of events with no final state radiation are copied from Table 3.2 for comparison. Each variation is applied individually, not consecutively.

Sample	$p_{\mathrm{T}}^{\mathrm{e}} > 20$ GeV/c	$\lvert\eta^e\rvert < 2.5$	$p_{\mathrm{T}}^{\mathrm{e}} > 20$ GeV/c and $\lvert\eta^e\rvert < 2.5$
Relative to PYTHIA LO			
Default	$85.20 \pm 0.04\%$	$44.43 \pm 0.05\%$	$42.11 \pm 0.05\%$
+ FSR	$83.32 \pm 0.04\%$	$44.55 \pm 0.05\%$	$41.39 \pm 0.05\%$
+ PS	$85.20 \pm 0.04\%$	$44.52 \pm 0.05\%$	$42.18 \pm 0.05\%$
+ k_{T}	$84.06 \pm 0.04\%$	$44.52 \pm 0.05\%$	$41.82 \pm 0.05\%$
+ ISR	$78.60 \pm 0.04\%$	$47.26 \pm 0.05\%$	$41.72 \pm 0.05\%$
Relative to Full PYTHIA			
Default	$76.92 \pm 0.04\%$	$47.27 \pm 0.05\%$	$40.87 \pm 0.05\%$
- FSR	$78.62 \pm 0.04\%$	$47.34 \pm 0.05\%$	$41.73 \pm 0.05\%$
- PS	$76.98 \pm 0.04\%$	$47.28 \pm 0.05\%$	$40.95 \pm 0.05\%$
- k_{T}	$77.00 \pm 0.04\%$	$47.29 \pm 0.05\%$	$40.93 \pm 0.05\%$
- ISR	$82.22 \pm 0.04\%$	$44.60 \pm 0.05\%$	$41.09 \pm 0.05\%$

comparable with NNLO QCD corrections. More importantly, real electroweak corrections (*ie* photon radiation) affect the final state in a leptonic Z/γ^* decay. In effect, the final state of a significant fraction of events is modified from e^+e^- to $e^+e^- + n\gamma$. In the simulation used here, this final state radiation (FSR) is modelled using PHOTOS [37, 38], which calculates radiative QED corrections to decay processes in a generic way that can be applied to any process. The calculations use the leading-logarithmic approximation, and include effects such as interference in $f\overline{f}$ final states and multi-photon radiation. The effect of photon FSR on the acceptance of the lepton p_{T} and η cuts was shown in Table 3.2. FSR has a large effect on the p_{T} cut acceptance, almost 5% with respect to "PYTHIA LO". This is reduced to a 2% effect when the cut on $|\eta|$ is applied as well.

Some characteristic distributions of the radiated photons in $Z/\gamma^* \to e^+e^-$ events are shown in Figure 3.4. Generally, most radiated photons have a very low p_{T}, $\mathcal{O}(\mathrm{GeV}/c)$, and a very small ΔR separation from the radiating electron. However, there are very long tails in these distributions, indicating that a small number of events are expected

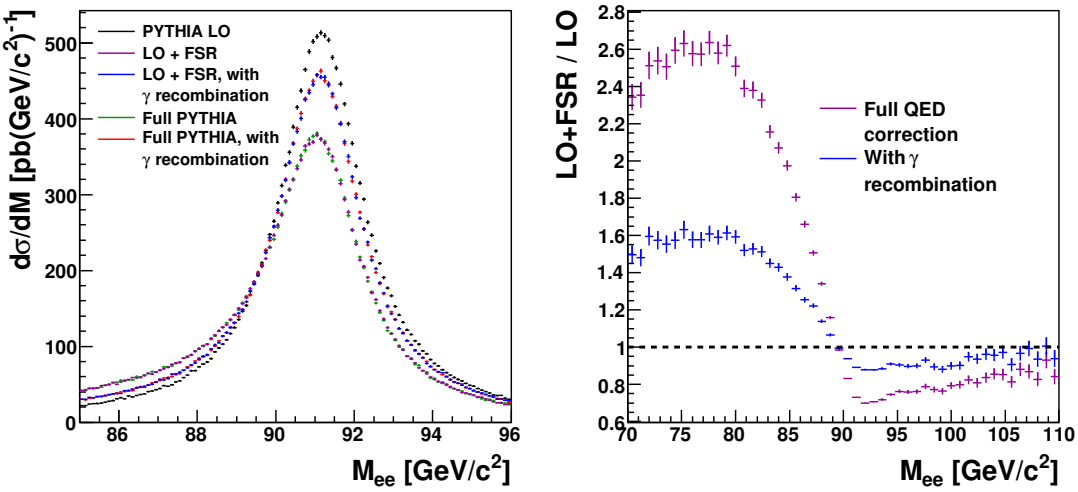

Figure 3.5: Left: Distribution of M_{ee} in PYTHIA with and without PHOTOS. Right: Ratio $\sigma_{\mathrm{LO+FSR}}/\sigma_{\mathrm{LO}}$ as a function of M_{ee}, with and without photon recombination.

to have significant photon radiation. The finite spatial resolution of the electromagnetic calorimeter means that if the electron-photon $\eta - \phi$ separation is much less than the typical electromagnetic calorimeter cluster size of $\Delta\eta \times \Delta\phi \approx 0.1 \times 0.1$ (*cf* Section 5.1.3), both are likely to be reconstructed within the same cluster. To study this effect, *recombined* electrons have been constructed in the generated data, whereby a photon's 4-momentum is added to the nearest electron if they are separated by $\Delta R_{e\gamma} < 0.05$. This cutoff value has been chosen because it is approximately equal to the radius of a reconstructed EM cluster, although the results presented here are found not to depend strongly on this choice. Increasing the cutoff value to 0.1 changes the effect of recombination by approximately 10%.

All of the acceptances in Table 3.2 have been recalculated with photon 4-momenta recombination, with results shown in Table 3.3. Trivially, the acceptance values for samples without FSR are unchanged. Photon recombination reduces the impact of FSR on the acceptance by approximately a factor of 2, leaving a 1% correction when both p_{T} and $|\eta|$ cuts are applied.

FSR also significantly alters the M_{ee} spectrum. Clearly, this distribution needs to be understood to determine the acceptance correction for a cut on the di-electron invariant mass. Figure 3.5 shows how the M_{ee} spectrum shifts due to FSR, and how this shift is reduced by photon recombination. With or without photon recombination,

Table 3.4: Acceptance of a cut of $70 < M_{ee} < 110$ GeV/c^2 for events generated with $M_{Z/\gamma^*} > 60$ GeV/c^2. Electron-photon recombination ("γ recomb.") does not alter the "PYTHIA LO" result, as there is no FSR in this case.

	Without γ recomb.	With γ recomb.
PYTHIA LO	$96.23 \pm 0.02\%$	–
Full PYTHIA	$90.78 \pm 0.03\%$	$94.03 \pm 0.02\%$

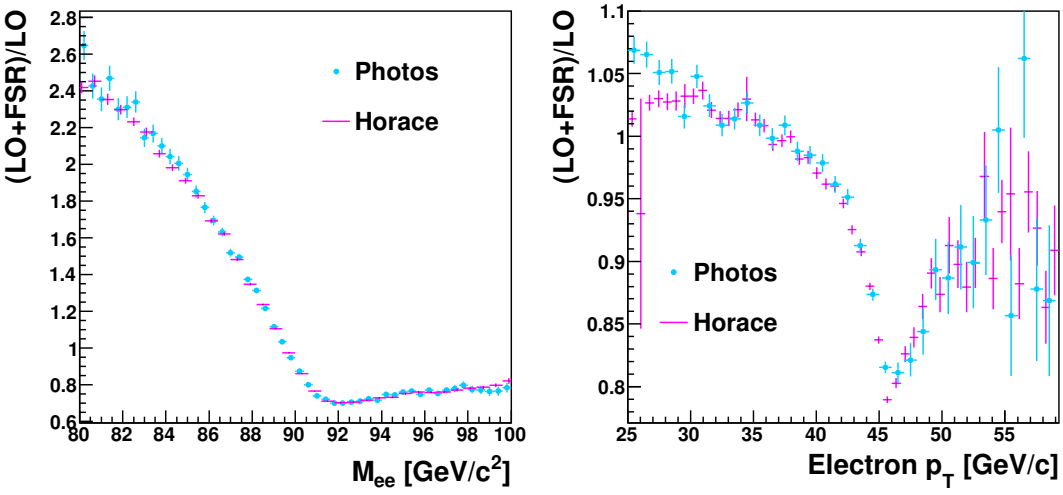

Figure 3.6: Comparison of modifications to the di-electron mass and electron p_{T} from radiative QED corrections using PHOTOS and complete $\mathcal{O}(\alpha)$ electroweak corrections using HORACE. The plots show the ratio of the corrected to the LO differential cross sections. Left: as a function of M_{ee}. Right: as a function of $p_{\mathrm{T}}^{\mathrm{e}}$.

the di-electron mass spectrum corresponding to "LO+FSR" closely matches the "Full PYTHIA" mass spectrum. Thus, this spectrum is unaffected by the other PYTHIA processes, and its acceptance uncertainty can be studied with QED models only. The right panel of Figure 3.5 shows the ratio of the mass spectra with and without FSR, illustrating the size of this correction as a function of M_{ee}. Photon recombination reduces FSR effects significantly, by as much as 60% at a mass of 80 GeV/c^2. This is particularly relevant when acceptance cuts on the di-electron mass are considered. Table 3.4 shows how the acceptance of a cut on the di-electron mass is modified by FSR and photon recombination. Photon radiation causes a fall in the acceptance of 5.4% with respect to "PYTHIA LO". Applying photon recombination reduces this difference to 2.2%.

Whereas PHOTOS includes only real QED corrections, a full set of $\mathcal{O}(\alpha)$ elec-

troweak corrections has been calculated, and is included in the HORACE event generator [28, 29]. The predictions of HORACE and PHOTOS for the di-electron mass and the electron p_{T} are compared in Figure 3.6. For PHOTOS, the ratio (LO + FSR)/LO is shown, while the equivalent ratio for HORACE includes the full electroweak corrections. In the mass variable, good agreement is observed, whilst for the electron p_{T} a discrepancy of up to 5% is seen at low p_{T} values.

Although the principal concern here is the effect of radiation on the acceptance of $Z/\gamma^* \to e^+e^-$ events, it is worth noting that electroweak effects also affect the total cross section. It has been shown that the additional real and virtual corrections to the rate not included in PHOTOS amount to a factor of $1 + \frac{3\alpha}{4\pi}$, a 0.17% correction [45].

3.3.5 Electroweak parameterisation

Electroweak theory has a large number of parameters, which can be mutually dependent. For example, the relationship $\sin^2\theta_W = 1 - M_W^2/M_Z^2$ (valid in a Leading Order approximation) means that only two of $\sin^2\theta_W$, M_W and M_Z are independent. In PYTHIA, and most other event generators, different electroweak parameter schemes are available, in which different variables are treated as independent.

PYTHIA has a choice of three schemes for electroweak parameterisation when calculating production cross sections and decay widths ([31], page 194). In Scheme 0 (the default), $\alpha(Q^2)$, $\sin^2\theta_W$, M_W and M_Z are set independently. In the other two schemes, $\alpha(Q^2)$ is treated as a derived quantity, and the Fermi weak coupling constant G_F is independent. Thus, in Scheme 1, $\sin^2\theta_W$, G_F, M_W and M_Z are treated independently. In Scheme 2, $\sin^2\theta_W$ is also treated as a derived quantity, calculated in terms of M_W and M_Z.

To test these variations, the cross section and acceptance of $Z/\gamma^* \to e^+e^-$ events were calculated using PYTHIA with each electroweak scheme in turn. Corresponding results calculated using MCFM version 5.2 [46, 47] were also provided.[8] MCFM is a tool for calculating cross sections in hadron colliders up to NNLO in α_s. Results presented here are calculated at LO precision in QCD, and use the default MCFM electroweak scheme, where G_F, M_W and M_Z are independent. This is closest to PYTHIA's Schemes

[8] MCFM calculations provided privately by U. Klein, University of Liverpool.

Table 3.5: Electroweak parameter values used in the electroweak parameter scheme test. These values only apply to the independent parameters used in each scheme. The value of α_s is that used by the CTEQ6L1 *pdf*s, while the other variables are based on the MCFM defaults.

$M_W = 80.419$ GeV/c^2	$\Gamma_W = 2.06$ GeV	$G_F/(\hbar c)^3 = 1.16639 \times 10^{-5}$ GeV^{-2}
$M_Z = 91.188$ GeV/c^2	$\Gamma_Z = 2.49$ GeV	$\alpha(0) = 1/137.036$
$M_t = 170.9$ GeV/c^2	$\sin^2\theta_W = 0.2312$	$\alpha_s(M_Z) = 0.12978$

Table 3.6: Total Leading Order cross sections and acceptances calculated by PYTHIA and MCFM[8] under different assumptions. Accepted events have two electrons with $p_{\mathrm{T}} > 20$ GeV/c and $|\eta| < 2.5$.

Generator	EW Scheme: Independent parameters	$\sigma_{Z/\gamma^* \to e^+e^-}$ at LO [pb]	$\mathcal{A}$
PYTHIA	0: $\alpha(Q^2)$, $\sin^2\theta_W$, M_W, M_Z	1685.4 ± 0.9	$(42.17 \pm 0.05)\%$
PYTHIA	1: $\sin^2\theta_W$, M_W, M_Z, G_F	1704.5 ± 0.9	$(42.23 \pm 0.05)\%$
PYTHIA	2: M_W, M_Z, G_F	1681.7 ± 0.9	$(42.20 \pm 0.05)\%$
MCFM	1: M_W, M_Z, G_F	1710.0 ± 0.7	$(42.09 \pm 0.06)\%$

1 and 2. The electroweak parameters used in these tests are motivated by the MCFM default parameters, listed in Table 3.5. These are different from PYTHIA's default values used elsewhere.

Table 3.6 shows the cross sections and acceptances calculated using these schemes, together with their statistical uncertainties. Depending on the scheme and generator used, the cross section predictions vary by up to 1.7%, with the PYTHIA results being consistently lower than the MCFM calculation. The acceptance is less sensitive to these changes than the total cross section. The three acceptance values calculated with PYTHIA are consistent within the statistical uncertainties, but differ from the MCFM value by 0.11% on average. As a fractional uncertainty on the acceptance, this is a very small effect of $\Delta\mathcal{A}/\mathcal{A} = 0.26\%$, which is to be taken as the systematic uncertainty on $\mathcal{A}$ from this source. Photon recombination and the additional PYTHIA processes have not been considered in this result, as MCFM does not include these processes. The uncertainty on the acceptance is assumed to remain unchanged upon inclusion of these processes.

3.3.6 Parton density functions

Although not investigated here, the choice of parton density function will also affect the acceptance of $Z/\gamma^* \to e^+e^-$ events, and contributes to its uncertainty. This uncertainty is addressed in [44], which examined a range of *pdf* (and other) uncertainties on the Z/γ^* boson production cross section and acceptance. Using the CTEQ6.5 *pdf* parameterisation set, and kinematic cuts similar to those used here,[9] their figures suggest a fractional uncertainty on the acceptance $\Delta\mathcal{A}/\mathcal{A}$ of 1.5% arising from the choice of *pdf* parameterisation. This uncertainty does not take into account the effect of photon recombination. Recent work by the H1 and ZEUS collaborations has provided new data which reduces the uncertainties in the *pdf* parameterisations [22, 48]. The uncertainty on the total Z/γ^* cross section is thus reduced from a few percent down to $\mathcal{O}(1\%)$. However, these studies do not directly address the uncertainty on the acceptance of $Z/\gamma^* \to e^+e^-$ events at the LHC.

3.4 Higher order QCD and QED corrections and a test of factorisation

In Sections 3.3.1 to 3.3.4, various non-LO aspects of PYTHIA, used in conjunction with PHOTOS, have been examined. Although PYTHIA calculates total cross sections using Leading Order matrix elements, it emulates many higher order and nonperturbative processes which are relevant when differential distributions are considered. This is an advantage when the events are used as an input to a Monte Carlo detector simulation, as the simulated distributions will be closer to those observed in the experiment. However, the underlying matrix element calculation is still ultimately incorrect, especially considering that NNLO QCD calculations are available [27], in addition to the aforementioned $\mathcal{O}(\alpha)$ electroweak calculations.

A common approach is to adjust the Monte Carlo prediction by K-factors, which are calculated in order to scale events generated by PYTHIA until the absolute cross section and distributions match those from the higher order predictions. In general, these K-

[9] The acceptance cuts used in [44] are: $p_{\mathrm{T}}^{\mathrm{e}} > 20$ GeV/c, $|\eta^e| < 2.0$ and $79 < M_{ee} < 104$ GeV/c^2.

factors are calculated by comparing (say) NNLO QCD to the strict LO calculation:

$$K = \frac{\sigma_{NNLO}}{\sigma_{LO}}. \tag{3.2}$$

Scaling of the total cross section in this manner does not affect the calculation of the event acceptance as the LO kinematic distributions are left unchanged. Higher order corrections to the acceptance would need to consider differential K-factors:

$$K(x) = \frac{d\sigma_{NNLO}/dx}{d\sigma_{LO}/dx}, \tag{3.3}$$

where x corresponds to some relevant variable (*eg* y_Z, $p_{\mathrm{T}}^{\mathrm{Z}}$) or a group of variables. This form of reweighting can change the acceptance, as it changes the kinematic distribution of electrons in the event. There are two problems with using Equation 3.3 in practice. First of all, this definition of $K(x)$ cannot be applied to events generated by PYTHIA due to the modification of the event kinematics by the additional included processes. This particularly applies to $p_{\mathrm{T}}^{\mathrm{Z}}$, for example. Secondly, there is currently no program capable of calculating higher order corrections for both QCD and QED effects simultaneously. If these effects could be shown to factorise, these corrections could be calculated and applied independently of each other, but there is no *a priori* reason to assume that this is the case.

The first of the above problems can be addressed by referring all correction factors to the event generation used for simulation. In the case of PYTHIA, one would define

$$K'(x) = \frac{d\sigma_{NNLO}/dx}{d\sigma_{PYTHIA}/dx}. \tag{3.4}$$

Such a reweighting method has been tried by others in the context of Higgs production [49, 50]. In that study, the authors found that the reweighted simulation and fixed-order calculations agreed well in kinematic regions where fixed-order calculations are reliable. The two estimates differed near kinematic boundaries where resummation effects in the reweighted simulation (but not the fixed-order calculation) are important. If this reweighting were to be applied to $Z/\gamma^* \to e^+e^-$ events, a careful consideration of these issues would be important.

The second problem, relating to the combination of QED and QCD effects, can only be addressed by a model which includes both types of effect, such as the PYTHIA and

Table 3.7: Table of the acceptance ratios δ_{Full} and δ_{LO}, as defined in Equations 3.6 and 3.5, for different PYTHIA processes. The first row shows the combined effect of all processes together.

Sample		$p_{\text{T}}^{\text{e}} > 20$ GeV/c	$\lvert\eta^e\rvert < 2.5$	$p_{\text{T}}^{\text{e}} > 20$ GeV/c and $\lvert\eta^e\rvert < 2.5$
PYTHIA	δ_{LO}	$-12.68 \pm 0.06\%$	$6.39 \pm 0.16\%$	$-5.87 \pm 0.16\%$
FSR	δ_{LO}	$-5.74 \pm 0.06\%$	$0.27 \pm 0.16\%$	$-4.77 \pm 0.16\%$
	δ_{Full}	$-5.37 \pm 0.07\%$	$-0.15 \pm 0.15\%$	$-5.01 \pm 0.16\%$
PS	δ_{LO}	$0.00 \pm 0.06\%$	$0.20 \pm 0.16\%$	$0.17 \pm 0.17\%$
	δ_{Full}	$-0.03 \pm 0.08\%$	$-0.02 \pm 0.15\%$	$-0.18 \pm 0.17\%$
k_{T}	δ_{LO}	$-1.34 \pm 0.06\%$	$0.20 \pm 0.16\%$	$-0.69 \pm 0.17\%$
	δ_{Full}	$-0.05 \pm 0.08\%$	$-0.04 \pm 0.15\%$	$-0.13 \pm 0.17\%$
ISR	δ_{LO}	$-7.75 \pm 0.06\%$	$6.37 \pm 0.16\%$	$-0.93 \pm 0.17\%$
	δ_{Full}	$-6.26 \pm 0.07\%$	$5.99 \pm 0.16\%$	$-0.43 \pm 0.17\%$

PHOTOS combination used earlier in this chapter. QED and QCD factorisation has been tested by comparing the fractional change in acceptance due to a given process X, where X is one of the additional PYTHIA processes listed in Section 3.2.1. The change with respect to "PYTHIA LO" is $\delta_{\text{LO,X}}$, given by

$$\delta_{\text{LO,X}} = \frac{\mathcal{A}_{\text{LO}+X}}{\mathcal{A}_{\text{LO}}} - 1. \tag{3.5}$$

This is to be compared with the fractional change observed when removing X from the "Full PYTHIA" calculation, $\delta_{\text{Full,X}}$:

$$\delta_{\text{Full,X}} = \frac{\mathcal{A}_{\text{Full}}}{\mathcal{A}_{\text{Full}-X}} - 1. \tag{3.6}$$

Equations 3.5 and 3.6 describe ratios of acceptances, as this is the quantity of interest for the present study. The size of $\delta_{\text{Full/LO,X}}$ indicates how significant the effect of process X is, while the sign indicates if it tends to increase (positive) or decrease (negative) the acceptance. If the effect of process X factorises with that of the other processes, the ratios $\delta_{\text{LO,X}}$ and $\delta_{\text{Full,X}}$ should be equal. The different δ values are shown Table 3.7 (without photon recombination) and Table 3.8 (with photon recombination). Note than in the case where X is the set of all differences between "PYTHIA LO" and "Full PYTHIA", $\delta_{\text{LO}} = \delta_{\text{Full}}$ by definition.

In almost every case, agreement between δ_{LO} and δ_{Full} is observed, to within $\sim 0.5\%$.

Table 3.8: Table of the acceptance ratios δ_{Full} and δ_{LO}, as defined in Equations 3.6 and 3.5, for different PYTHIA processes, where final state photons and electrons are recombined if $\Delta R_{e\gamma} < 0.05$. The first row shows the combined effect of all processes together.

Sample		$p_{\text{T}}^{\text{e}} > 20$ GeV/c	$\lvert\eta^e\rvert < 2.5$	$p_{\text{T}}^{\text{e}} > 20$ GeV/c and $\lvert\eta^e\rvert < 2.5$
PYTHIA	δ_{LO}	$-9.72 \pm 0.06\%$	$6.39 \pm 0.16\%$	$-2.94 \pm 0.16\%$
FSR	δ_{LO}	$-2.21 \pm 0.06\%$	$0.27 \pm 0.16\%$	$-1.71 \pm 0.16\%$
	δ_{Full}	$-2.16 \pm 0.07\%$	$-0.15 \pm 0.15\%$	$-2.06 \pm 0.17\%$
PS	δ_{LO}	$0.00 \pm 0.06\%$	$0.20 \pm 0.16\%$	$0.17 \pm 0.17\%$
	δ_{Full}	$-0.08 \pm 0.08\%$	$-0.02 \pm 0.15\%$	$-0.20 \pm 0.17\%$
k_{T}	δ_{LO}	$-1.34 \pm 0.06\%$	$0.20 \pm 0.16\%$	$-0.69 \pm 0.17\%$
	δ_{Full}	$-0.10 \pm 0.08\%$	$-0.04 \pm 0.15\%$	$-0.15 \pm 0.17\%$
ISR	δ_{LO}	$-7.75 \pm 0.06\%$	$6.37 \pm 0.16\%$	$-0.93 \pm 0.17\%$
	δ_{Full}	$-6.45 \pm 0.07\%$	$5.99 \pm 0.16\%$	$-0.54 \pm 0.17\%$

In particular, QED FSR appears to factorise from the different QCD processes at this level or better, for the particular cuts chosen. This is true whether or not photon recombination is applied. It is however evident that for the effects of ISR and primordial k_{T}, factorisation is not completely satisfied. This is most obvious in the case where only the p_{T}^{e} cut is applied, where δ_{LO} and δ_{Full} differ by $\mathcal{O}(1.5\%)$. This observation can be understood by remembering that these two processes contribute towards the boson p_{T}. When applied individually to "PYTHIA LO", both processes increase the p_{T} from 0 to some value in each event. When applied together, they will not in general boost the boson in the same direction, meaning that for the final p_{T}^{Z}, the effects add quadratically rather than linearly. The effect of applying primordial k_{T} (contributing ~ 2 GeV/c to the boson p_{T}) on top of ISR (which can contribute many tens of GeV/c to p_{T}^{Z}), which is measured by $\delta_{\text{Full,k}_{\text{T}}}$, is particularly small. Applying the cut on $\lvert\eta^e\rvert$ significantly reduces the non-factorisation, down to the 0.5% level. However, when both cuts are applied, addition or removal of ISR has much less effect on the acceptance than when either cut is applied individually, as was noted in Section 3.3.1.

These uncertainties worsen as $p_{\text{T}}^{\text{cut}}$ increases. This is seen in Figure 3.7, which shows different δ values as a function of $p_{\text{T}}^{\text{cut}}$. As the allowed range of $\lvert\eta^e\rvert$ is fixed by the ATLAS tracking system, the acceptances used in Figure 3.7 include the standard

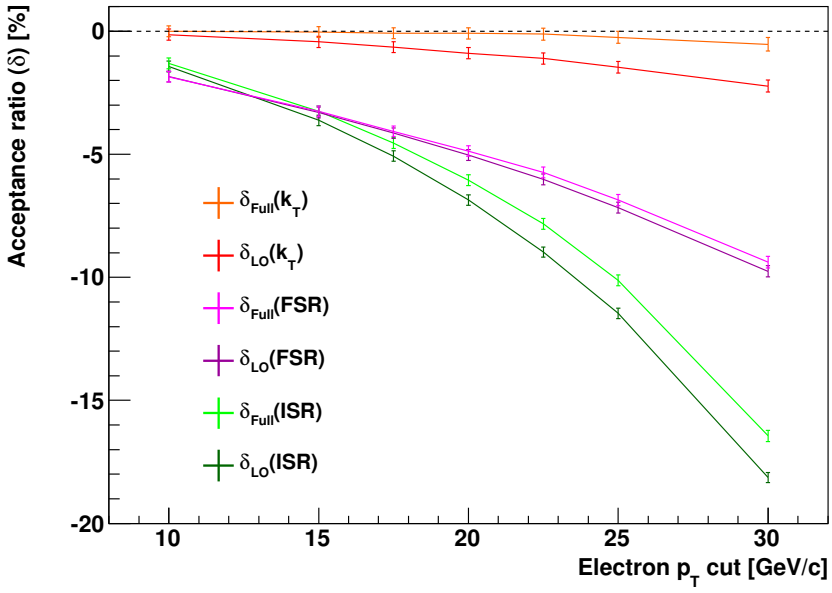

Figure 3.7: Ratio of acceptances (without photon recombination) as a function of p_{T} cut. All acceptances are relative to that for events where both electrons have $|\eta| < 2.5$.

$|\eta^e|$ cut. This shows that, within this $|\eta|$ range, ISR, FSR and primordial k_{T} all tend to decrease the acceptance, with their effects becoming more pronounced as $p_{\mathrm{T}}^{\mathrm{cut}}$ is increased. In addition, the difference between δ_{LO} and δ_{Full} becomes larger as $p_{\mathrm{T}}^{\mathrm{cut}}$ increases. This implies that applying K-factors derived from fixed-order calculations to full Monte Carlo events may give results that are incorrect by several percent for the highest values of $p_{\mathrm{T}}^{\mathrm{cut}}$, if higher order effects on the boson kinematics are similar to the ISR modelling in PYTHIA. Applying K-factors for QED effects is expected to have a smaller uncertainty due to factorisation, especially if photon recombination is applied.

3.5 Summary and conclusions

In the previous sections, the effects of various processes or corrections on the acceptance of $Z/\gamma^* \rightarrow e^+e^-$ events have been considered. Each process is subject to some theoretical uncertainty, which will contribute in turn to the theoretical uncertainty on the acceptance.

In considering the additional PYTHIA processes, such as ISR, FSR and the primordial k_{T}, it will be assumed, in common with the acceptance studies in [42], that the impact of each process on $\mathcal{A}$ is accurate to within 20%. Therefore, 20% of the

Table 3.9: Estimated fractional uncertainty on the acceptance of $Z/\gamma^* \to e^+e^-$ events. The results marked * do not account explicitly for photon recombination.

	Without γ recombination	With γ recombination
ISR, FSR, PS, k_{T}	1.06%	0.44%
M_{ee} cut acceptance	1.1%	0.44%
Electroweak scheme	0.26%	0.26%*
*pdf*s	1.5%	1.5%*
Total	2.2%	1.6%

observed effect on the acceptance due to a given process is taken as the uncertainty for that process. The uncertainties thus obtained are added in quadrature to derive the total uncertainty from these processes. The results depend on whether or not photon recombination is applied. Applying this prescription to the results in the final columns of Tables 3.2 and 3.3 yield estimates of the total relative uncertainty $\Delta\mathcal{A}/\mathcal{A}$ due to ISR, FSR, Parton Showers and primordial k_{T} of 1.06% without and 0.44% with photon recombination. It should be noted that these uncertainties do rely on a significant cancellation between the increase in $|\eta|$ acceptance and decrease in p_{T} acceptance caused by ISR.

It is expected that the ISR corrections included in PYTHIA give a reasonable agreement in the lepton distributions compared to those from NLO and NNLO predictions, and therefore it is assumed that the 20% uncertainty applied on the ISR correction is adequate to account for the uncertainty in the acceptance due to missing higher order QCD effects. Similarly, it is assumed that, given the good agreement observed between PHOTOS and HORACE, a 20% uncertainty on the FSR correction should be adequate to cover the uncertainty of missing higher order electroweak effects. In further studies, higher order effects could be accounted for more thoroughly by implementing the prescriptions described for differential K-factors in Section 3.4.

FSR modifies the acceptance of the M_{ee} cut, as discussed in Section 3.3.4. The uncertainty of this is also taken to be 20% of the overall change in $\mathcal{A}$, which is 1.1% without and 0.44% with photon recombination. The full uncertainty on the acceptance must also include the uncertainties arising from the electroweak scheme and the *pdf*

parameterisation, as discussed in Sections 3.3.5 and 3.3.6 respectively. The results are summarised in Table 3.9. These uncertainties could be improved by repeating the analysis using tools which include higher order effects, especially NLO QCD, in addition to using more recent *pdf* parameterisations.

In events generated with $M_{Z/\gamma^*} > 60$ GeV/c^2, the acceptance for events with $p_{\mathrm{T}}^{\mathrm{e}} > 15$ GeV/c, $|\eta^e| < 2.5$ and $70 < M_{ee} < 110$ GeV/c^2 is therefore:

$$\mathcal{A}_{\mathrm{e}} = 37.56\% \pm 0.05\% \text{ (stat.)} \pm 0.83\% \text{ (theory)}. \tag{3.7}$$

If photons within $\Delta R_{e\gamma} < 0.05$ of final state electrons are recombined with those electrons, the acceptance is modified, becoming:

$$\mathcal{A}_{\mathrm{e}\gamma} = 39.17\% \pm 0.05\% \text{ (stat.)} \pm 0.63\% \text{ (theory)}. \tag{3.8}$$

Recombining electrons and photons signficantly reduces both the size and the uncertainty of QED corrections to $\mathcal{A}$. In Chapter 9, it will be seen that this recombination procedure is also important at an experimental level as it significantly reduces the uncertainties on the detector resolution.

Chapter 4

The ATLAS Detector and Trigger

In this chapter, the physical hardware of the Large Hadron Collider (LHC) and the ATLAS detector is described. The LHC and the associated experiments are introduced first, in Section 4.1. Then, the main design aims of ATLAS are described in Section 4.2, followed by the principal detector components in Sections 4.3 to 4.6. The trigger and luminosity measurement systems are discussed in Sections 4.7 and 4.8. Finally, some recent detector commissioning results are summarised in Section 4.9.

4.1 The LHC

The LHC (`http://lhc.web.cern.ch/lhc/` and [51]) is a proton-proton synchrotron collider, 27 km in circumference, pictured in Figure 4.1. Built at the site of the European Organisation for Nuclear Research (CERN), it occupies the tunnel which used to house the Large Electron-Positron Collider (LEP), straddling the French/Swiss border near Geneva. The LHC is the highest energy collider in the world, capable of accelerating protons up to 7 TeV, and lead ions up to 2.8 TeV per nucleon. To produce rare processes at an acceptable rate, the LHC is designed to collide protons at an extremely high rate, up to a luminosity of 10^{34} cm^{-2}s^{-1} (10^{27} cm^{-2}s^{-1} for heavy ions), resulting in approximately a billion collisions per second.

The LHC first became operational on 10^{th} September 2008, an event which received wide media publicity. Although no *pp* collisions took place in 2008, all the major LHC experiments saw events resulting from protons colliding with deliberately placed beam stops and the low-density gas remaining in the beam pipe. The ensuing period of commissioning with beam was short however, owing to an accelerator incident nine

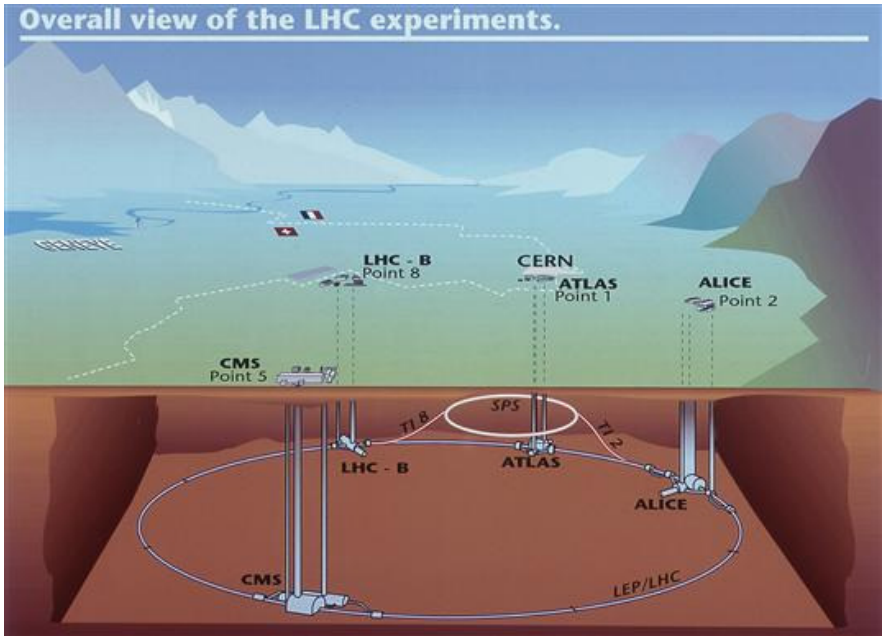

Figure 4.1: Schematic view of the LHC tunnel and the four major experiments, described in the text.

days later [52]. Much effort has since been devoted by the experiments at the LHC to a long period of commissioning using cosmic muons. Following major repairs to sections of the accelerator, beam is expected to recommence in late 2009, with collisions following soon after. For safety reasons, the first high energy collisions will occur with a reduced beam energy, to be increased in phases over time.

The LHC is designed to maximise two critical parameters for discovery of new physics. These are the collision energy and luminosity. The increase of parton density functions towards low x, especially due to the gluon contribution, (see Figure 2.2 for an example) means that as proton energy increases, so do inclusive cross sections for processes involving a significant mass scale. Achieving beam energies of 7 TeV requires a large magnetic field to bend the protons around the LHC ring. A cross section of an LHC dipole is shown schematically in Figure 4.2. Superconducting magnets are used, cooled with liquid helium at 1.9 K. The double aperture design allows the simultaneous acceleration of protons in both directions.

The instantaneous luminosity, denoted $\mathcal{L}$, is primarily a function of the beam shape and currents. It determines the expected rate for a process with a given cross section

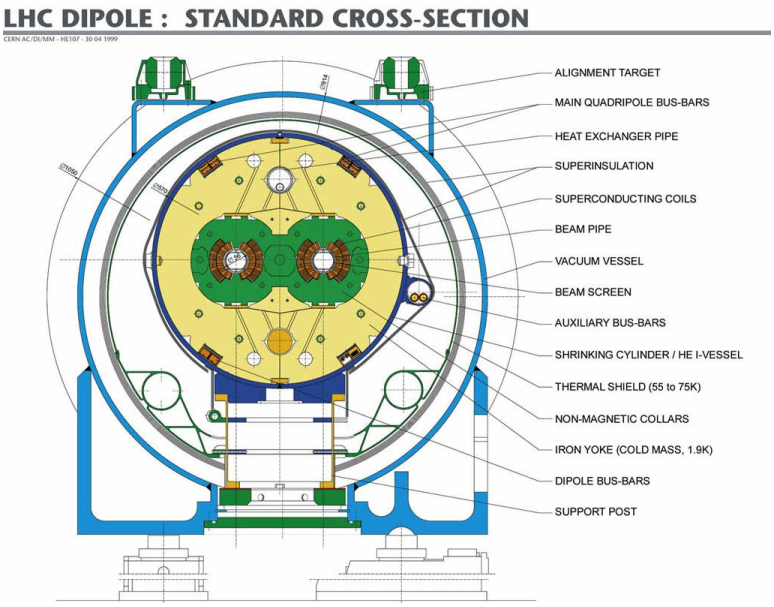

Figure 4.2: Cross-sectional diagram of an LHC dipole magnet. The two apertures for the beams can clearly be seen, as well as the various support structures and services.

σ:

$$N = \sigma \int \mathcal{L} dt = \sigma \mathrm{L}. \tag{4.1}$$

The quantity $\mathrm{L} = \int \mathcal{L} dt$ is called the *integrated luminosity*. This has dimensions of cm^{-2}, or more commonly the inverse of some (sub)multiple of the *barn* (b). When operational, the LHC will achieve its challenging design luminosity by focussing the high current proton beams close to each interaction point and by having a high bunch crossing rate of one bunch every 25 ns.

4.1.1 Collider experiments at the LHC

The ATLAS experiment ([53, 54] and Figure 4.3), and to a large extent the entire LHC, is designed to probe the energy and luminosity frontiers in proton collisions. It is hoped that many new physical phenomena will be discovered, both within and beyond the Standard Model of particle physics. ATLAS is a general purpose detector, designed for maximum sensitivity to the many potential signatures which may characterise this new physics.

In addition to ATLAS, the LHC hosts three other major experiments, as shown in Figure 4.1. These experiments are called ALICE [55], CMS [56] and LHCb [57]. Of these three, CMS is the most similar to ATLAS in its physics aims and overall design.

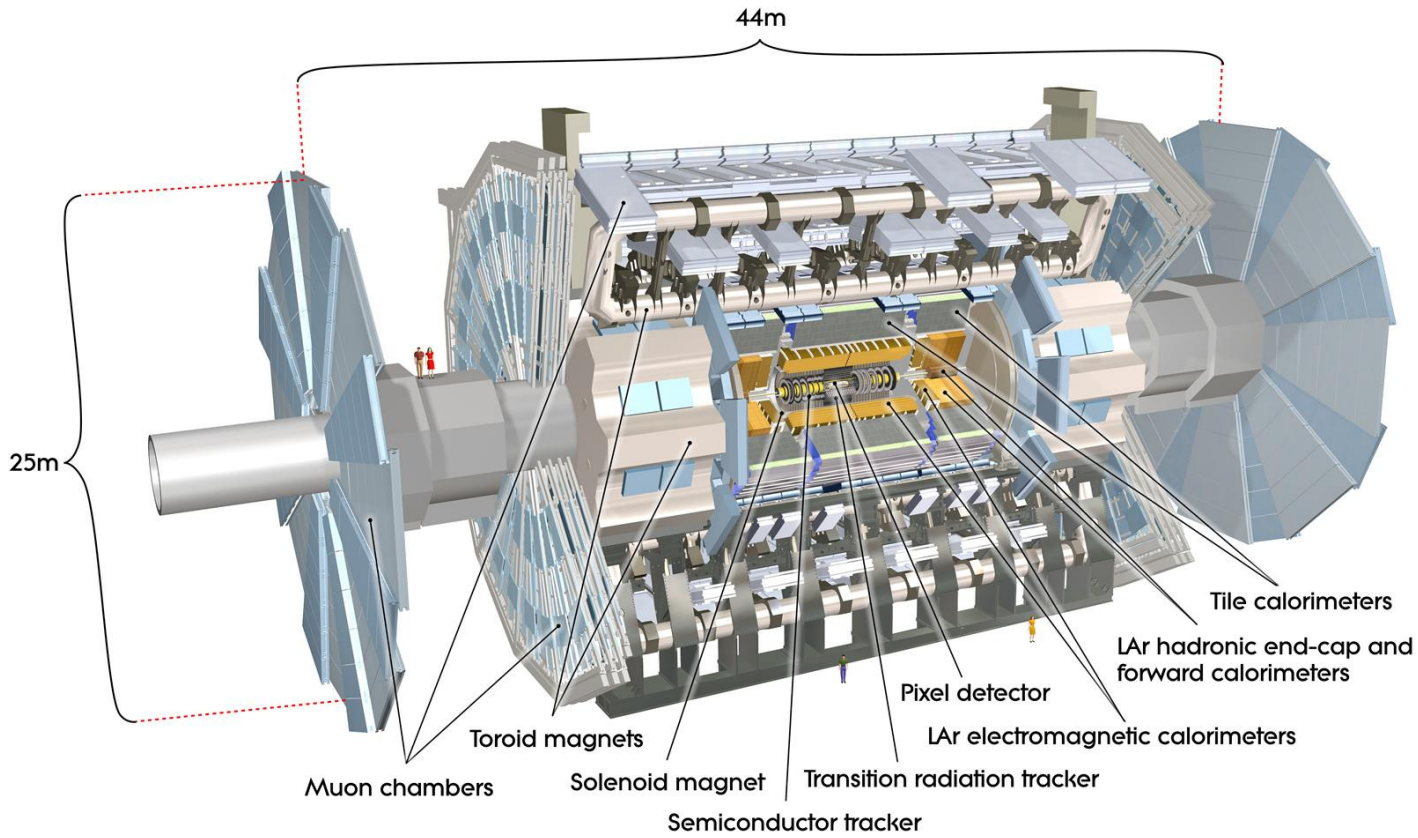

Figure 4.3: Cut-away view of the ATLAS detector, showing the positions of the various subdetectors.

Having two general purpose experiments at the LHC not only doubles the number of rare events recorded, but the two experiments use differing technologies and thus can also be used to cross-check each other's results. LHCb is a single arm spectrometer, designed to precisely measure the properties of B mesons in order to better understand quark flavour mixing. With precise enough measurements, it may be possible to see effects which come into play at energies far beyond our direct reach. Finally, ALICE is optimised for heavy ion collisions, to investigate complex strongly interacting systems and the quark-gluon plasma. In addition, the LHC hosts two smaller experiments (LHCf [58] and TOTEM [59]), which provide complementary physics measurements in the forward regions, using the same collisions as the general purpose experiments.

4.2 The ATLAS Experiment

The principal physics aims of ATLAS can be loosely sorted into four categories. These are: Standard Model physics (including flavour physics), Higgs physics, searches for physics beyond the SM, and heavy ion physics. To accommodate all of these, ATLAS has a general-purpose design, capable of detecting and measuring different types of particles. The main design aims of ATLAS were [53]:

- Fast, radiation-hard electronics and sensors with high granularity.
- Good momentum resolution, detector efficiency and vertex identification (*eg* secondary vertices from b and τ decays).
- Electromagnetic calorimetry for electron and photon measurements, and full coverage hadronic calorimetry for jet and missing E_{T} measurements.
- Muon identification and measurement over a wide range of energies.
- High efficiency triggers with excellent background rejection, capable of working with low thresholds in a high multiplicity environment.
- Good energy/momentum resolution in all subdetectors, summarised in Table 4.1.

All of this must be achieved with high precision in the challenging environment set by the LHC, with up to an anticipated 23 inelastic pp collisions per 25 ns bunch crossing,

Table 4.1: ATLAS design performance requirements, from [53]. The Muon spectrometer performance is quoted for a muon with $p_{\mathrm{T}} = 1$ TeV/c, measured in stand-alone mode, independently of the Inner Detector.

		η coverage	
Detector component	Required resolution	Measurement	L1 Trigger
Tracking	$\frac{\sigma_{p_{\mathrm{T}}}}{p_{\mathrm{T}}} = 0.05\%\ p_{\mathrm{T}} \oplus 1\%$	± 2.5	–
EM calorimetry	$\frac{\sigma_E}{E} = \frac{10\%}{\sqrt{E}} \oplus 0.7\%$	± 3.2	± 2.5
Hadronic calorimetry			
barrel and endcap	$\frac{\sigma_E}{E} = \frac{50\%}{\sqrt{E}} \oplus 3\%$	± 3.2	± 3.2
forward	$\frac{\sigma_E}{E} = \frac{100\%}{\sqrt{E}} \oplus 10\%$	$3.1 < \lvert\eta\rvert < 4.9$	$3.1 < \lvert\eta\rvert < 4.9$
Muon spectrometer	$\frac{\sigma_{p_{\mathrm{T}}}}{p_{\mathrm{T}}} = 10\%$	± 2.7	± 2.4

consisting mostly of inelastic QCD processes.

Throughout the following descriptions of the ATLAS detector, a common set of coordinates will be used. The z direction is defined to be along the beam pipe, with the origin located at the centre of the detector. The horizontal x axis is defined to point towards the centre of the LHC ring and y axis vertically upwards, so that x, y, z form a right-handed set. The polar (θ) and azimuthal (ϕ) angles are defined with respect to this axis system. Instead of θ, it is more usual to use the *pseudorapidity* η to describe the polar angle, where η is defined as

$$\eta = -\ln\tan(\theta/2). \tag{4.2}$$

Radial distances are denoted by $R = x^2 + y^2$, while the transverse component of momentum is $p_{\mathrm{T}} = \sqrt{p^2 - p_z^2}$. In some cases, it is more convenient to define *transverse energy* as the energy deposited in a calorimeter component, corrected for its position by the formula $E_{\mathrm{T}} = E/\cosh\eta$. In the highly relativistic limit, and neglecting calorimeter resolution effects, the deposited transverse energy is equal to the p_{T} of the incident particle.

4.3 The Inner Detector

The Inner Detector (ID, [53, 60]) has to cope with a high charged particle density resulting from the LHC collisions. This demands the use of a high granularity design,

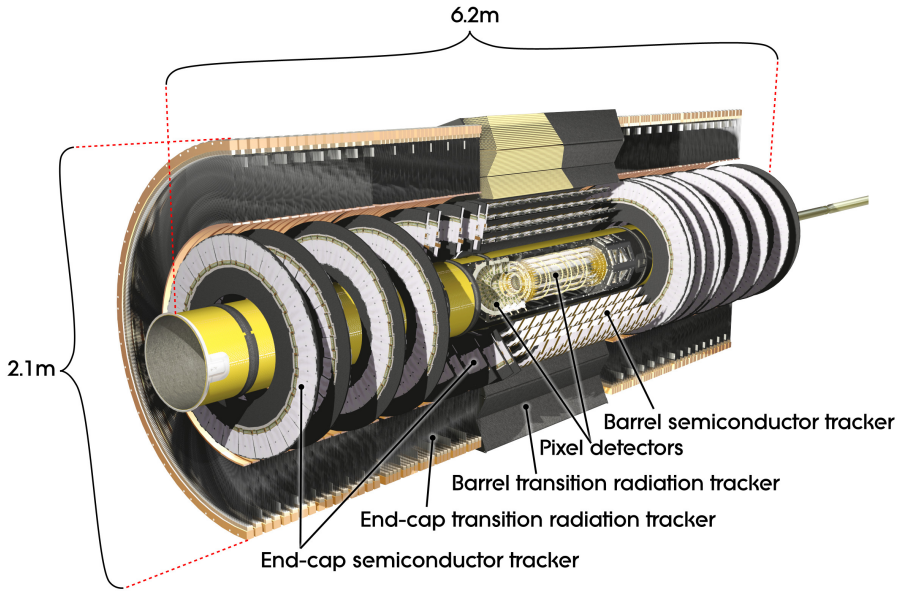

Figure 4.4: Cut-away view of the ATLAS Inner Detector, showing the three main components: pixels, SCT and TRT.

achieved through the use of silicon technology in the first two layers (pixels and SCT), and a straw tube gaseous detector in the outer layer (TRT). These three main subsytems are each divided into one barrel and two endcap sections, as illustrated in Figure 4.4. The detector as a whole covers the region $|\eta| < 2.5$.

In addition to simply detecting charged particles (above a nominal p_{T} threshold of 0.5 GeV/c), the ID provides a measurement of track momenta as well as location of the primary vertex and possible secondary vertices in each event. The ID is immersed in a 2 T magnetic field provided by a superconducting solenoid positioned on the inner face of the electromagnetic calorimeter. In this field, a charged particle with a transverse momentum of 40 GeV/c is expected to produce a track with a sagitta of approximately 1 mm. The field is considerably weaker near the ends of the ID cavity due to the finite length of the solenoid.

4.3.1 The Pixel detector

The pixel subdetector [61] lies closest to the interaction point, with the innermost layer (also called the b-layer) positioned at $R \sim 5$ cm. Over 1,500 modules, segmented in $R - \phi$ and z, provide approximately 80.4 M readout channels. The presence of this subdetector improves the vertex location capabilities of the ID, especially for finding

secondary vertices from c, b and τ decays. This is achieved through excellent position resolution, down to 10 μm in $R-\phi$ and 115 μm in z (R) in the barrel (endcap). The pixel layers provide three space points for a typical track within its acceptance.

Due to the proximity of the pixel detector to the beam where radiation levels are highest, the innermost layer will need replacing after approximately three years of running at nominal luminosity. The other components are able to survive a 1 MeV neutron equivalent fluence F_{neq} of $\sim 8 \times 10^{14}$ cm^{-2}, the equivalent of approximately 10 years of ATLAS running. To avoid reverse annealing, leading to an increase of the required bias voltage, after the inevitable radiation damage, the pixels need to be kept at temperatures of -5 to -10 °C during most of their life span [62].

An instrument called the Beam Conditions Monitor (BCM, [63]) is also installed very close to the beam line, to protect the pixels and other ATLAS components from misdirected proton beams. The BCM consists of two diamond sensors, equally placed less than 6 cm from the beam at $|z| = \pm 1.9$ m. Normal pp collisions will produce coincident signals while events like collimator or beam gas collisions will produce signals with a time difference of $\Delta z/c = 12.5$ ns. These can be used to trigger an LHC beam abort. As well as being an essential safety feature, the BCM will also provide a triggering signal and a bunch-by-bunch luminosity estimate, complimentary to LUCID, the principal luminosity measuring system (see Section 4.8).

4.3.2 The Silicon Tracker

The main Silicon Tracker (SCT) modules consist of back-to-back sensors with silicon strips, arranged with a stereo angle of 40 mrad between the layers [64, 65]. Signals in strips on opposite sides of a module allow *space points* to be formed, defined as the location where the strips cross. With four concentric barrels and nine disks in each endcap, this detector typically provides four space points for each track within the acceptance. In the barrel, one set of strips is aligned along z, and in the endcaps, one set is aligned along R, allowing a precision measurement of ϕ, with an $R-\phi$ resolution of around 17 μm [53]. The small stereo angle, chosen to reduce ambiguities to acceptable levels, means that the resolution of the orthogonal coordinate (z in the barrel and R in the endcaps) is worse, around 580 μm. Like the pixel detector, the SCT needs to

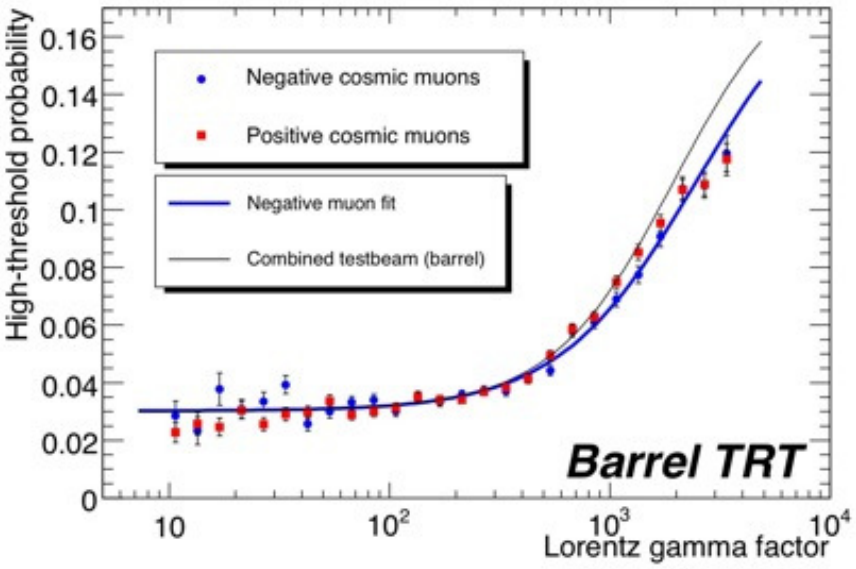

Figure 4.5: Probability of high threshold hits being produced per straw within the TRT barrel as a function of the Lorentz factor E/m. This is measured both for cosmic muons and in test beams.

operate in a high radiation environment, and has been designed to survive up to an integrated equivalent fluence of $F_{\text{neq}} = 2 \times 10^{14}$ cm^{-2}.

4.3.3 The Transition Radiation Tracker

The final layer of the ID is the Transition Radiation Tracker (TRT, [66, 67, 68]). This is designed to provide a large number of hits per track, typically 36, and aid particle identification through the detection of transition radiation. Due to budgetary and time constraints, this subdetector has a slightly reduced coverage compared to the pixels and SCT, covering $|\eta| < 2.0$. The TRT is constructed from drift tubes ("straws"), each 4 mm in diameter and filled with xenon-based gas mixture. Each straw provides $R - \phi$ measurements (in the barrel) with an intrinsic precision of 130 μm per straw. The transition radiation is produced by polypropylene-polyethylene fibres in the barrel and polypropylene foils in the endcaps, interleaved with the straws. Ultra-relativistic particles (electrons, in particular) passing through the numerous dielectric boundaries in these materials can produce low energy transition radiation photons which contribute to the ionisation in the xenon gas mixture, thus enhancing the signal amplitude. The measured probability for high threshold hits as a function of E/m is shown in Figure 4.5,

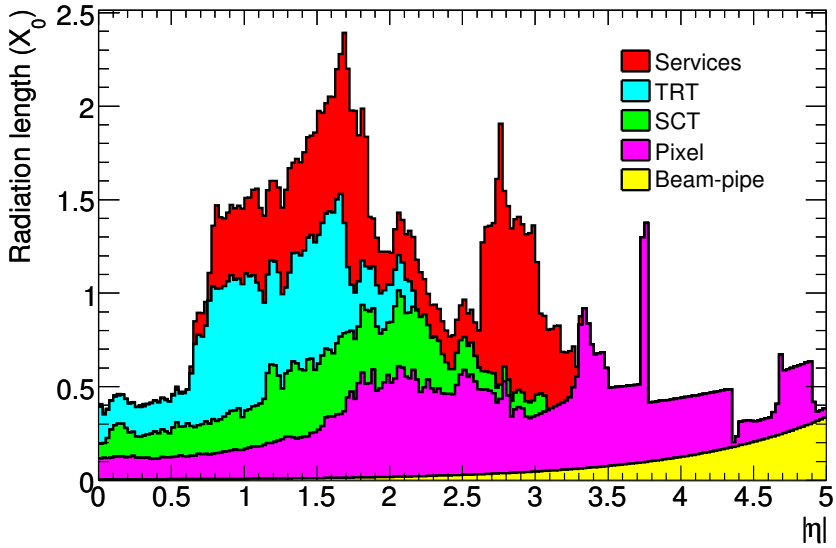

Figure 4.6: Cumulative material traversed within the Inner Detector envelope by an infinite momentum track as a function of $|\eta|$. The material depth is measured in units of the radiation length X_0.

and its use in identifying electrons is described in Section 5.1.4.

4.3.4 Inner Detector summary

Each ID subdetector has its own optimised readout architecture, with certain elements common to the whole system. The ID is not part of the Level 1 trigger (see Section 4.7), so the data from each event, after being digitised on-detector, are simply stored in buffers of sufficient length to cover the Level 1 trigger latency. Subject to a Level 1 accept, the data are then passed to the off-detector electronics.

One of the most important parameters of the ID is the amount of material it contains. Increased multiple scattering, bremsstrahlung and photon conversion all affect track reconstruction quality and momentum measurements. The magnitude of these effects is determined by the number of radiation lengths traversed by a particle crossing the ID. This is plotted in Figure 4.6 as a function of $|\eta|$. The gap between barrel and endcap sections of the ID housing the barrel and pixel endcap services can clearly be seen at $|\eta| \sim 1.5$. The ATLAS detector simulation includes a detailed description of this material, based on extensive bookkeeping and weighing of the detector components.

The Inner Detector performance is critically dependent on its successful alignment.

During normal running, a daily selection of $\mathcal{O}$(1M) tracks will be selected for ongoing monitoring of the alignment. This should be sufficient to determine the silicon module positions with a precision of 10 μm. Even without collisions, significant steps towards good alignment have been made using cosmic rays, as described in Section 4.9.1.

In addition to misalignments, a further uncertainty comes from the knowledge of the magnetic field inside the ID volume. This was mapped using a moveable array of Hall probes just before ID installation, with the barrel and endcap calorimeters in their final positions. The combination of this and a detailed simulation has achieved an average fractional bending power uncertainty in the range 2 to 12×10^{-4}, mostly within the range required for a precision measurement of the W mass. Four permanent NMR probes will monitor any long term drifts in the field during running, from their positions near $z = 0$.

Another vital rôle of the Inner Detector is to provide a precise determination of the primary vertex location in each event. One of the hardest channels for this is $H \rightarrow \gamma\gamma$, where the particles with the highest p_{T}, the photons, leave no tracks. Nevertheless, measuring the location of this vertex is essential for a measurement of the Higgs mass in this channel. In this most difficult case, using only tracks from the hadronic final state, the primary vertex resolution is expected to be < 40 μm in $x - y$ and < 80 μm in z. In busier events with more high-p_{T} tracks (such as $t\bar{t}$ production) and beam constraints, these resolutions can be reduced down to ~ 11 μm and ~ 40 μm respectively.

4.4 The Electromagnetic Calorimeter

Calorimetry in ATLAS is divided into two parts - electromagnetic and hadronic. A cutaway view of both systems is illustrated in Figure 4.7. The electromagnetic part, described here, extends out to $|\eta| < 3.2$, while the other calorimeter systems are described in Section 4.5. The purpose of the electromagnetic calorimeter system is twofold. First, it identifies and precisely measures electrons and photons. Second, it measures the electromagnetic component of jets within its acceptance. Detailed descriptions of the EM calorimeter may be found in [53, 69, 70, 71].

Inside the EM calorimeter, liquid argon is used as an ionising medium. The liqud

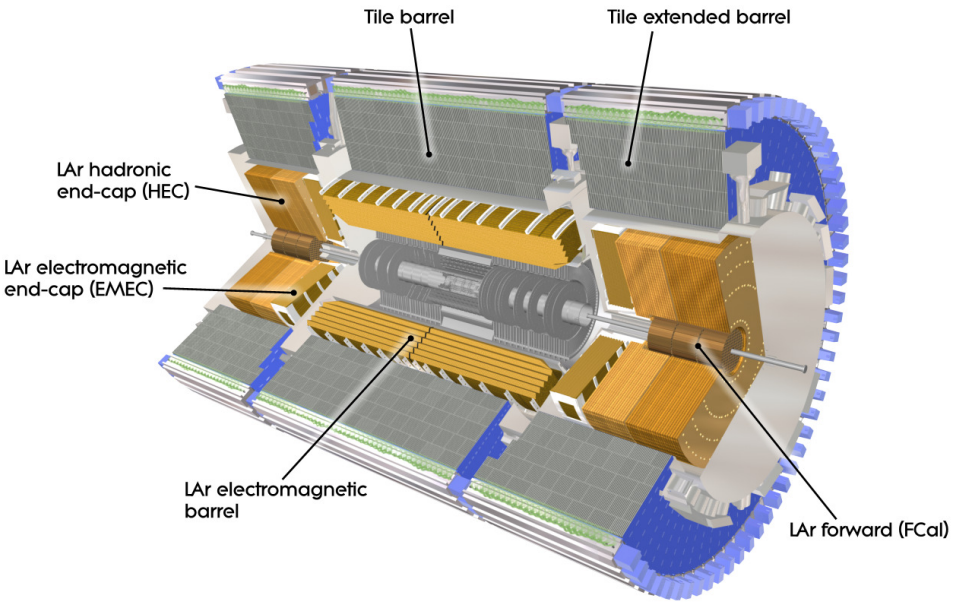

Figure 4.7: Cut-away view of the ATLAS calorimeter system, showing the main components.

argon fills the gaps between the accordion-shaped lead absorbers and kapton electrodes (see Figure 4.8). This design was chosen to achieve uniform coverage over ϕ, and because liquid argon is an intrinsically linear, radiation-hard medium which will have a stable response over time. The folding angle, absorber thickness and wave amplitude all vary with radius and η to optimise linearity and resolution.

To measure shower evolution as a function of depth, the EM calorimeter is longitudinally segmented. Within $|\eta| < 2.5$ (corresponding to the Inner Detector acceptance), there are three principal segments or layers. The first layer is finely segmented in η (although the segmentation granularity varies in $|\eta|$), providing a precise position measurement in that direction. The second layer is the largest, and absorbs most of the electromagnetic energy in a shower or jet. The third layer, just in front of the hadronic calorimeter, is used to estimate possible energy leakage from EM showers from the rear of this calorimeter. These three layers are illustrated in Figure 4.8. Within the range $|\eta| < 1.8$ there is, in addition, a fourth, presampling, layer in front of the first layer. This is used to estimate energy losses for electrons and photons before reaching the calorimeter. In the region $2.5 < |\eta| < 3.2$, the design is similar but with a coarser granularity and only two longitudinal layers. In the forward regions ($|\eta| > 3.2$), a

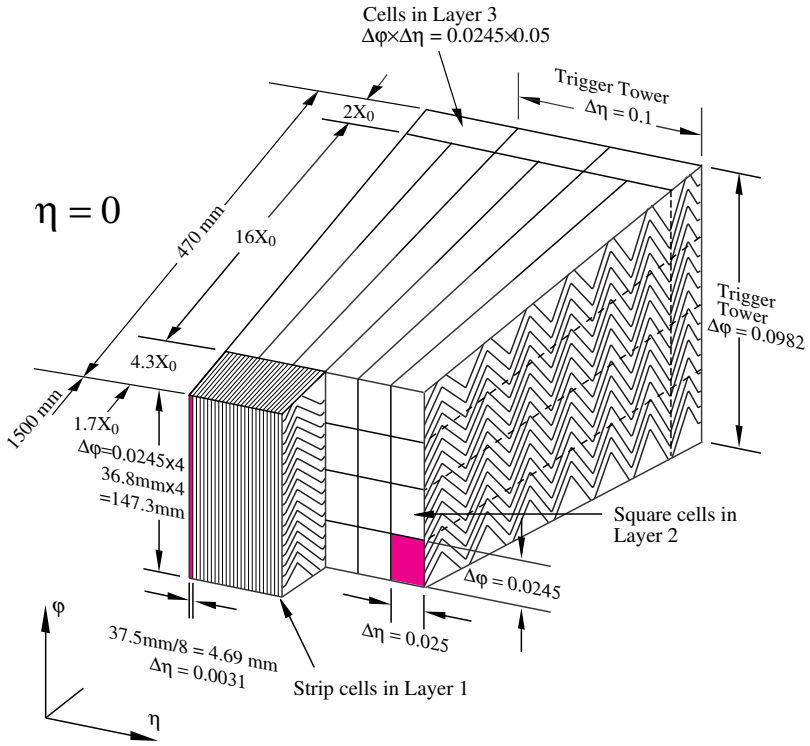

Figure 4.8: Schematic of a section of the barrel EM calorimeter. The accordian structure is visible, as well as the different granularities in each layer and trigger tower.

different set of liquid argon calorimeters measure both electromagnetic and hadronic components of jets. These will be discussed in Section 4.5.

The region of transition between barrel and endcap sections in the EM calorimeter ($1.37 < |\eta| < 1.52$) is expected to be more challenging in terms of calibration and reconstruction, due to the increased dead material (for services, support structures, *etc*) in this region. While scintillators are in place to estimate losses, it is assumed in this thesis that this region will not be well enough understood for precision measurements in early data.

The electronics for the electromagnetic calorimeter have been designed to allow the provision of trigger signals within the Level 1 latency, as well as having a high radiation tolerance and dynamic range (signals range from $\sim$ 10 MeV to $\sim$ 3 TeV). To satisfy these requirements, signal amplification and digitisation is handled by the front-end electronics on the detector, which also provide analogue sums of deposits in trigger "towers" for the Level 1 calorimeter triggers. Initial calibration has been performed using precisely controlled charge injections directly into the detector cells, in addition

to test beam runs. This tests the full readout system, including preamplification.

The EM calorimeter is designed to have good energy reconstruction performance for electrons and photons. In test beams at the CERN SPS ring, it has been shown to be linear to within 0.1% for electrons between 15 and 180 GeV [72], while nonuniformities across η and ϕ are typically at the level of 0.5 to 0.6% [73]. The same studies investigated the resolution of the calorimeter's response, in terms of the three main contributing factors:

$$\frac{\sigma(E)}{E} = \frac{a}{E(\text{GeV})} \oplus \frac{b}{\sqrt{E(\text{GeV})}} \oplus c. \tag{4.3}$$

Here, a is the coefficient for noise terms, including pile-up and other biases, and is more significant at low energies. b is the coefficient for stochastic noise, which includes fluctuations in the signal sampling as well as lateral or longitudinal leakage. Finally, c quantifies the calibration uncertainty, energy losses and other factors which scale with energy. These terms are added in quadrature (indicated by the $\oplus$ symbol) to find the final resolution as a function of E. Typical values for the coefficients are $a \simeq 250$ MeV, $b = 10\ \%\sqrt{\text{GeV}}$ [72] and $c = 0.5 - 0.8\%$ [73], satisfying the requirements of Table 4.1. The electron and photon identification performance was also tested in these runs. For an electron reconstruction efficiency of 90%, pion rejection factors of between 200 and 1400 were measured [74].

4.5 Hadronic Calorimeters

The ATLAS hadronic calorimeters [53] cover the range $|\eta| < 4.9$. Their purpose is to completely stop and absorb all strongly interacting particles produced in each collision, both for the measurement of jets and to avoid hadronic punch-through into the muon system. Figure 4.9 shows the depth of each calorimeter system in interaction lengths (the depth of material over which all but $1/e$ of hadronic particles will interact). With at least 10 interaction lengths over almost the complete angular range, hadronic jets should be well contained.

As Figure 4.9 shows, different technologies are used in different regions of the hadronic calorimeter. Each consists of at least three samplings, for shower profile measurements. At the lowest pseudorapidities ($|\eta| < 1.7$), a sampling calorimeter called

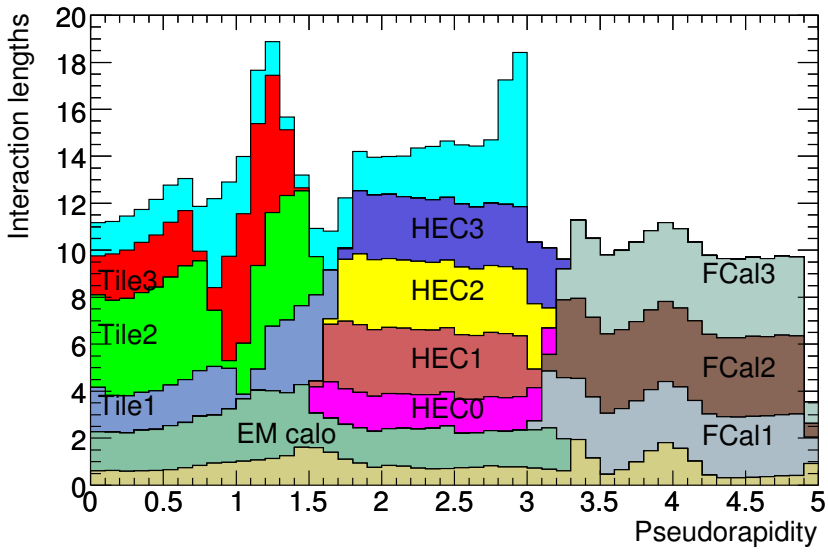

Figure 4.9: Cumulative depth, in terms of interaction lengths, in front of and inside each calorimeter layer. All calorimeters are shown: the EM calorimeter, the hadronic calorimeters in the barrel (Tile) and end caps (HEC), and the forward calorimeters (FCal). For $|\eta| < 3$, the total material in front of the first active layer of the muon spectrometer is also shown in blue.

TileCal is used [53, 75]. This contains steel absorbers and scintillating tiles arranged as shown in Figure 4.10. This design provides a good calorimeter depth at limited cost, and allows the TileCal to act as the return yoke for the magnetic field of the ID solenoid. The scintillation light in the tiles is read out, via wavelength shifting fibres, by photomultiplier tubes positioned behind each calorimeter module. The fibres are grouped to form pseudo-projective readout cells, where the projection is towards the nominal interaction point. A small plug calorimeter is used to estimate energy losses in the transition region between the barrel and extended barrel sections.

In the intermediate region ($1.5 < |\eta| < 3.2$), the hadronic endcap (HEC) calorimeter is responsible for jet measurements [53, 71]. Due to the more intense radiation environment, this uses a liquid argon technology, similar to the EM calorimeter but with copper absorbers to provide the necessary density of material [76, 77]. This subdetector shares its cryostat with the EM endcap calorimeter and forward calorimeters. Two separate wheels have two longitudinal layers each, giving four in total.

The forward calorimeters (FCal [78]), just visible in Figure 4.7, also use liquid argon as the active medium. They complete the calorimetry system, extending measurements

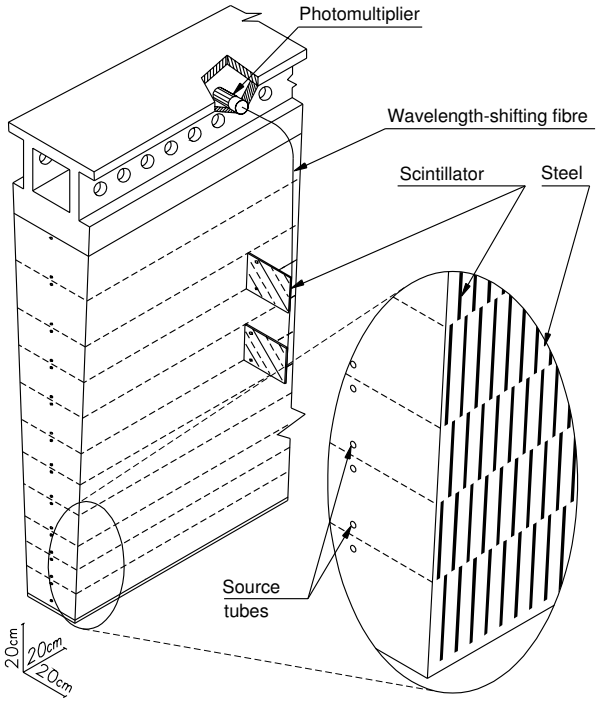

Figure 4.10: Schematic of a TileCal module, showing the optical readout from the scintillating tiles.

out to $|\eta| = 4.9$. The FCal has a high density design with high granularity output, due in part to its location and size, but also due to the high particle density expected this close to the beam line. It consists of three longitudinally separated modules. The first module has copper absorbers, and is optimised for electromagnetic measurements. The other two modules have tungsten absorbers, and are primarily for measuring hadronic energy deposits. An FCal electrode consists of a co-axial copper rod and tube, separated by a small gap filled with liquid argon. The electrodes are supported by copper plates (FCal1) or small tungsten slugs (FCal2 and FCal3).

The final calorimeters associated with ATLAS are located away from the main detector, 140 m either side of the interaction point. The Zero Degree Calorimeters (ZDC, [79, 80]) measure neutral particles, especially neutrons, at very low angle ($|\eta| > 8.2$). Their main purpose is to determine the centrality of heavy ion collisions, but they also increase the acceptance for diffractive processes and provide a trigger for minimum bias events during low luminosity running.

The readout of the hadronic and forward calorimeter systems mirrors that of the electromagnetic calorimeter described in Section 4.4, in its split between front-end and

back-end electronics. Like the EM calorimeter, these systems provide energy sums in pseudo-projective towers for the Level 1 trigger decision, with similar latency requirements. The liquid argon components of the hadronic calorimeter are calibrated in a similar way to the EM calorimeter, with charge injections into the preamplifiers. The FCal can inject pulses at the front-end crates to independently test the system. Due to the additional demands of optical components in its design, the TileCal has three on-detector calibration methods. The first is, again, based on charge injection to test the electronics alone. To test optical performance and PMT response, calibrated laser pulses can be sent into each cell. Finally, a radioactive ^{137}Cs source can be moved hydraulically around the calorimeter to monitor overall performance.

4.6 The Muon Spectrometer

The Muon Spectrometer (MS [53, 81]) defines the outer dimensions of ATLAS, and is the largest component in terms of detector volume. It is essentially a tracking detector, designed to measure the curvature of muons in a toroidal magnetic field, independently of the Inner Detector. Due to the depth of the calorimeters, muons are typically the only particles that pass through the muon systems, save for the undetectable neutrinos. The MS consists of *precision* chambers to accurately measure the momenta of muons, and *trigger* chambers with Level 1 trigger capability. The precision and trigger chambers of the MS cover the pseudorapidity range $|\eta| < 2.4$, roughly corresponding to the Inner Detector acceptance, while additional chambers without Level 1 trigger capability extend measurement coverage in the forward regions up to $|\eta| = 2.7$. The approximate positions of the various chambers described in this section are shown in Figure 4.11.

The toroidal magnetic field, is supplied by a large system of superconducting air-core magnets (see Figure 4.3). In the barrel region, eight 25.3 m long magnets supply an effective field of ~ 0.5 T, with muon chambers arranged inside the field. In each endcap, eight smaller but stronger magnets generate a more localised field of ~ 1 T, with muon chambers located before and after the field.

The sensitive chambers are arranged projectively, in three stations (*ie* layers) for both barrel and endcap regions. In the toroidal field, muons bend in the η direction,

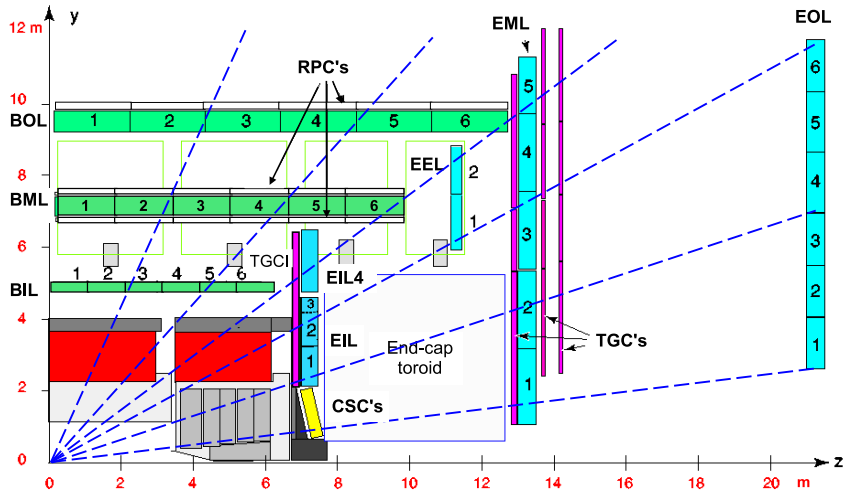

Figure 4.11: Section through the ATLAS Muon Spectrometer, showing how infinite momentum tracks would propagate through the various chambers. MDTs are shown in green and blue, the other MS chambers are as marked. Parts of the ATLAS calorimeter system can also be seen, for comparison.

which is therefore the direction that the precision chambers measure. Over most of the MS, Monitored Drift Tubes (MDTs) make this measurement. In the forward regions ($2 < |\eta| < 2.7$), Cathode Strip Chambers (CSCs) are used in the inner station, where occupancies are high.

The trigger chambers are interleaved between the precision chambers. These perform three tasks: to measure the ϕ coordinate of the muons, to provide a fast signal for the Level 1 trigger decision, and to provide bunch-crossing identification information. A mixture of Resistive Plate Chambers (RPCs) in the barrel and Thin Gap Chambers (TGCs) in the endcaps are used for this purpose.

The desired performance of the MS, together with its large size, places stringent requirements on the knowledge of module positions and of the magnetic field. The expected sagitta, within the MS, of the track of a muon with $p_{\mathrm{T}} = 1$ TeV/c for example is only ~ 0.5 mm. Muon chamber alignment uncertainty must therefore be significantly better than this. To this end, a complex optical alignment system has been developed and installed. Combined with track-based alignment algorithms, an ultimate precision of around 30 μm on sagitta measurements is expected.

As well as the chamber positions, knowledge of the magnetic field is critical for

momentum measurements, especially since the field is highly nonuniform. The bending power is described by the field integral over a given track, $\int B\mathrm{d}l$, and needs to be understood to within a few parts in a thousand. To this end, the MS volume is monitored by about 1800 3D Hall sensors located on the MDT chambers and endcap toroid cryostats to measure spatial variations. In addition, two NMR probes track any long-term drifts in the field strength. These measurements have been compared with simulations in order to reconstruct the positions of the toroidal coils and to check perturbations caused by the TileCal and other magnetic structures. Using these methods, it is expected that the magntic field can be reconstructed to within 0.2%.

4.7 The ATLAS trigger

At the LHC design luminosity of 10^{34} cm^{-2}s^{-1}, it is not technically or financially feasible to permanently record every event to disk. At most, events can be recorded at an average rate of $\sim$ 200 Hz, corresponding to an acceptance rate of the order of one in 2×10^5 [82]. The online rejection of events is dealt with by the trigger system, which will be described in outline here. Details specific to electron triggers will be described further in Chapter 5.

ATLAS operates a three-level trigger. These are called Level 1 (L1, [83]), Level 2 (L2) and the Event Filter (EF). Level 2 and the Event Filter are collectively called the High Level Trigger, or HLT [82]. Each level improves on the previous level's decision by running increasingly sophisticated algorithms, at the cost of increased execution time. If an event is rejected at any level, processing on that event ceases and it is not passed on to the next level (or permanent storage in the case of the EF). Information is passed between levels based on *Regions of Interest* (RoIs), which describe where deposits passing a particular trigger threshold were found in the detector.

The full trigger system, as described here, will only be used at relatively high luminosities ($\mathcal{L} \gtrsim 10^{33}$ cm^{-2}s^{-1}). During earlier stages of running, less stringent criteria can be used, maintaining a constant event accept rate at each level. In addition to less severe selection criteria, early triggers may run one or more levels in *pass-through* mode, meaning that the event is passed to the next level without further selection.

At higher luminosities, the output rates of these early triggers will be too high, requiring modification of the thresholds and/or selection criteria. Some loose (even pass-through) triggers will continue to run for monitoring purposes, but they will be heavily *prescaled*. This means that only a small, randomly selected subset of events passing the trigger selection will be passed to the next level.

4.7.1 Level 1 event selection

The Level 1 (L1) trigger needs to be very fast, to cope with a bunch crossing rate of 40 MHz. It is therefore a hardware trigger, based around on-detector electronics, with a limited granularity view of the calorimeter and muon systems. The Inner Detector and precision muon chambers (MDTs) are not used for reasons of speed. In addition to the main ATLAS detector, Level 1 trigger signals are provided by the beam pickups, Beam Conditions Monitor (Section 4.3), Zero Degree Calorimeter (Section 4.5), the luminosity monitors ALFA and LUCID (Section 4.8), and forward scintillators designed to detect minimum bias events. The available system bandwidth limits the combined output rate for all L1 triggers to about 75 kHz, which may be upgraded to a maximum of 100 kHz. The available data buffering on the detector means that the Level 1 decision must be completed within 2.5 μs or less, on average. About 1 μs of this time is taken up by signal propagation alone.

Energy deposits in the calorimeters are summed in towers of size $\Delta\eta \times \Delta\phi = 0.1 \times 0.1$ [84]. The different L1 signatures are derived from these towers and L1 muon candidates. The L1 signatures include the detection of wide or narrow localised energy deposits (jet and $e/\gamma/\tau$ candidates respectively), as well as the "global" signatures of $\{-\sum \boldsymbol{p}_{\mathrm{T}}\}$, the missing transverse energy, and $\sum E_{\mathrm{T}}$, the scalar sum of transverse energy deposits.

Assuming an event passes the L1 selection, event data are read out by detector-specific electronics and transferred to the Readout Drivers (RODs), at the instruction of the L1 Central Trigger Processor (CTP). In parallel, RoI information is passed to the RoI Builder ready for processing by the Level 2 trigger.

4.7.2 Level 2 event selection

The Level 2 trigger is responsible for reducing the event rate down from the Level 1 output rate of 75−100 kHz to $\sim$ 2 kHz. It is a software-based trigger, run on a dedicated processor farm. The increased latency with respect to Level 1 (40 ms, including data transfer time) allows the Level 2 trigger to utilise the full detector granularity in both position and energy. Typically, this information will only be accessed within each RoI identified at Level 1, amounting to $1 - 2\%$ of a complete event.

The Level 2 decision improves upon that of Level 1 in several ways. The improved resolution means that higher p_{T} thresholds can be used without compromising efficiency. In addition, better particle identification can be achieved, especially through the use of the Inner Detector. Amongst other things, this allows electrons and photons to be distinguished for the first time.

Once an event is selected by the Level 2 trigger, it is passed to the event builder [85], where information from all parts of the detector are assembled into one contiguous structure, before being passed to the Event Filter.

4.7.3 The Event Filter

The Event Filter acts as the final pass before data is written permanently to tape. The final output rate must be less than 200 Hz, limited by offline processing power and storage capability. This is equivalent to approximately 300 MB s^{-1}. Event rejection at this level is improved by using algorithms and calibrations similar to those used for offline reconstruction. This is possible as the time budget of about 4 s per event is significantly larger than in Levels 1 and 2. Events accepted by the EF are recorded in inclusive *streams* according to the type(s) of objects which triggered the event. For example, there are streams forseen for electron, photon, muon, hadronic tau, jet, missing E_{T} and B physics signatures, as well as streams for calibration and detector monitoring [53], although this list is not final. After tests of both inclusive and exclusive streaming, it was decided to make these streams inclusive, meaning that complex events (*eg* $t\bar{t}$) may end up in more than one stream.

4.8 Luminosity determination

For ATLAS to be able to measure absolute cross sections, it is necessary to know the luminosity delivered as a function of time. Over the course of a fill (expected to last up to 12 hours) the instantaneous luminosity will vary significantly, decaying exponentially with a time constant of about 15 hours [51, Section 2.2.8]. This decay in luminosity is primarily due to collisions, but a number of other effects discussed in the reference also contribute. To track these variations, each fill of the LHC will be divided by ATLAS into so-called *luminosity blocks*. These are periods over which it may be assumed that the instantaneous luminosity is constant. Its precise duration has yet to be defined, but is likely to be of the order of minutes.

The primary luminosity monitor for ATLAS is LUCID ([53, Section 7.1] and [86]), which uses Čerenkov radiation to detect inelastic pp scattering, providing a relative luminosity measurement using the observed charged particle multiplicity. LUCID is primarily designed for online bunch-by-bunch luminosity monitoring, although a subset of LUCID events will be recorded for more detailed offline analysis of the luminosity and, potentially, studies of diffraction.

There are two LUCID detectors, placed either side of the interaction point at approximately $z = \pm 17$ m. Each contains twenty 15 mm diameter aluminium drift tubes, filled with C_4F_{10}, arranged around the beam pipe at a radial distance of approximately 10 cm. Simulations indicate that simply counting the number of tubes with a signal above a particular threshold will estimate the bunch luminosity sufficiently well for online monitoring, while more precise charge measuring methods can be used in offline processing. The BCM (see Section 4.3) can also provide bunch-by-bunch relative luminosity information.

Initially, the absolute luminosity delivered to ATLAS will be poorly known as estimates from the machine parameters may only be accurate to within about 20 or 30%, improving with time and possibly constraints from the heavy ion runs where luminosity measurements are simpler, using the ZDC (see Section 4.5).

Due for completion in 2010, the ALFA detector will monitor the absolute luminosity delivered to ATLAS with an expected precision of better than 5% (Section 7.2 of [53],

and [79, 86]). It will measure the elastic scattering amplitude of protons in the forward direction, which is related to the total (elastic and inelastic) cross section by the optical theorem. Relying on ATLAS itself for this measurement would lead to considerable inaccuracy due to the large extrapolations made necessary by its limited acceptance. Instead, special runs with low emittance beams will allow ALFA to detect the interference region between electroweak and hadronic forward scattering, giving the one extra parameter needed for an absolute luminosity measurement. This is possible because the scintillating fibres of ALFA are both far from the interaction point (at $|z| = 240$ m) and can be positioned very close to the beam (~ 1 mm), giving access to proton scattering events with very small momentum transfers ($< \sqrt{10^{-3}}$ GeV/c). This closeness to the beam is possible due to the use of *Roman pots* that allow moving detectors near the beam, and in which the detectors are only separated from the beam vacuum by a thin window. To obtain more precise results, ALFA's measurements can be compared with those from TOTEM [59], which will measure the total pp cross section at LHC Point 5 (CMS).

The final method of determining the absolute luminosity delivered to ATLAS may be by using W and Z/γ^* boson production. As described in Chapter 2, these processes have been calculated to NNLO precision. Current *pdf* estimates lead to uncertainties on W and Z/γ^* production rates of a few percent. If the cross sections for these processes can be understood sufficiently well, they could ultimately complement ALFA as an independent luminosity measure.

4.9 Detector commissioning with cosmics and single beam

The commissioning of ATLAS has been in progress now for many years. Some test beam results have already been described (*eg* in Section 4.4); this section concentrates primarily on results obtained during single beam running in September 2008 and cosmic ray events obtained at various times. As beam operations ceased on September 19$^{\text{th}}$ 2008 [52], an extended period of cosmic running followed, allowing improvement of the initial alignment and calibration of ATLAS before collisions commence later this year.

In this section, some of the major commissioning results relating to electron re-

Table 4.2: Current status of the Barrel sections of the Inner Detector, following commissioning efforts with cosmic rays and single beam running in 2008. In certain cases, data quality criteria have been required, see [90]. Some values will improve before data-taking with collisions begin. *This quantity is the probability that a hit associated with a track is caused by noise.

Subdetector	Operational fraction (approx.)	Noise occupancy/rate	Hit efficiency	$R-\phi$ residual widths
Pixels	98.5%	$< 2 \times 10^{-10}$	$> 99.7\%$	24 μm
SCT	99.5%	$5{\times}10^{-5}$	$\geq 99\%$	30 μm
TRT	98.2%	$< 1\%^{*}$	97.2%	187 μm

construction are summarised (*ie* the Inner Detector and the EM calorimeter). For a summary of the whole detector status, including the other subsystems, see [87] for example. The trigger is not discussed here, as the event types favour the commissioning of muon and minimum bias triggers. Some results are however discussed in the references provided, and also more specifically in [88] (Level 1) and [89] (HLT).

4.9.1 Commissioning of the Inner Detector

The full Inner Detector became operational in August 2008. The first LHC beams on September 10^{th} 2008 were used to time-in elements of the Inner Detector, although the pixels were off and the SCT ran at a reduced high voltage for safety reasons. In the following months, more than 7.5 million Inner Detector cosmic tracks were recorded, 2.7 M of these with the magnetic solenoid on [90]. Results are presented for the barrel detectors. The endcap results, while limited in statistical precision, generally indicate performance within specifications.

Some of the important commissioning parameters for the barrel Inner Detector components are summarised in Table 4.2. The fraction of operational modules reported are the current values, which in some cases have increased slightly since the 2008 cosmic run. This and other figures of merit in the table show the overall good state of each subdetector.

The third column in Table 4.2 shows the mean noise occupancy per channel per bunch crossing for the silicon detectors. This is a critical performance parameter, and both operate well within their design specifications. For the pixels, only about 10^{-4}

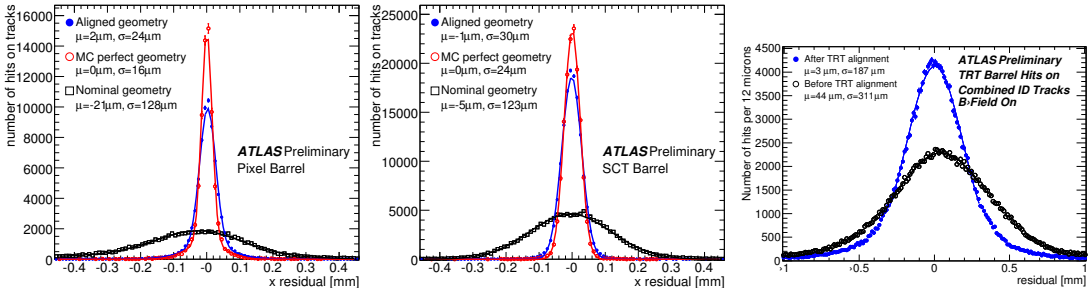

Figure 4.12: Residuals in the most accurate measurement direction between measured points in the Inner Detector barrel and the reconstructed track. Left: pixel detector. Middle: SCT. Right: TRT. Residuals before and after alignment are shown, as well as Monte Carlo values for a fully aligned detector (except for the TRT). For the silicon detectors, tracks are required to pass through the innermost pixel layer and have $p_{\mathrm{T}} > 2$ GeV/c. For the TRT plot, only hits in the outermost pixel layer are required.

known noisy channels had to be masked to achieve the quoted noise occupancy [91], while the SCT design requires mean occupancies of less than $5{\times}10^{-4}$. For the TRT, the probability of a hit on a track originating from noise is quoted.

The hit efficiencies in the fourth column are measured by extrapolating reconstructed tracks to an active component and checking for the presence of a signal in that component. Dead or inactive elements are excluded from this measurement. The silicon detectors are more than 99% efficient, while the slightly lower TRT efficiency is compensated by the larger number of hits per track in this subdetector.

The final quality figure in Table 4.2 is a measure of resolution, namely the width of the distribution in track residuals along the $R-\phi$ direction. The principal alignment procedure involves a phased global χ^2 fit which measures the displacements and rotations of whole subdetectors, then layers and modules, using reconstructed tracks. The residuals are shown in Figure 4.12, where it can be seen that the current resolutions already approach those expected for a fully aligned detector. Further studies, comparing track segments in upper and lower halves of the ID, have found that the measured resolution of the track parameters d_0, z_0, ϕ_0 and Q/p_{T} are also no more than 50% greater than expected for a perfectly realigned detector [90].

4.9.2 Commissioning of the EM calorimeter

Due to the ATLAS installation schedule, the EM calorimeters have been operational in the cavern since 2006. Cosmic ray events have been used since this time to complement

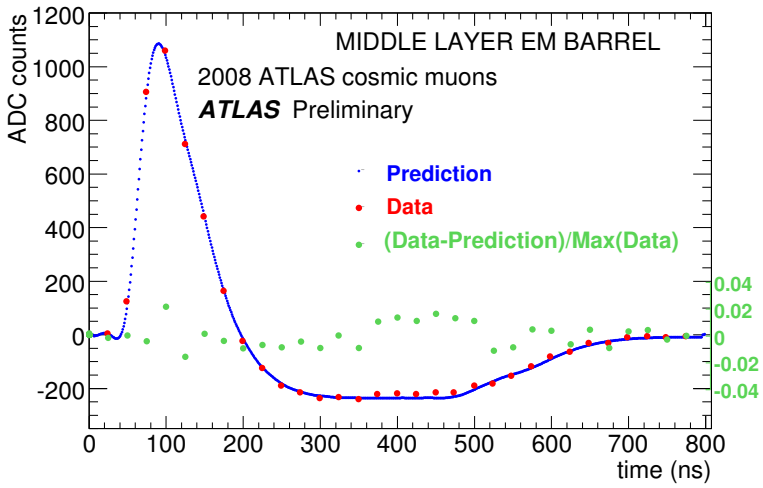

Figure 4.13: Ionisation pulse shape of a cosmic signal from strong muon bremsstrahlung, reconstructed in the middle layer of the EM barrel calorimeter. The measured values (red) are compared with the prediction (blue). The difference, normalised to the pulse height, is shown in green. The position of the rise at $500 - 700$ ns is sensitive to a potential shift of the electrode with respect to its nominal position.

some of the test beam studies described in Section 4.4. Although cosmic muons leave minimal deposits of energy in calorimeters, they can still be detected with a good signal to noise ratio. Detailed analysis of the energy scale and uniformity of the calorimeter have been performed [92], concluding that the energy scale agrees with the simulation to within 3% on average, and that the response uniformity was better than 2% in the range $|\eta| < 0.8$.

The more recent cosmic runs from 2008 are still being analysed, but some results are already available (see, for example, [93]). In these runs, approximately 99% of the EM calorimeter cells were operational. Most of the remainder had temporary problems relating to their power supplies or front-end electronics. These are expected to be operational before collisions commence, with just 0.02% of cells considered to be unrecoverable. In events where the muon suffers significant bremsstrahlung, it is possible to measure the calorimeter response pulse shape. These have been confirmed to be within 4% of expectations (see Figure 4.13). Drift times in the liquid argon have also been measured, confirming that the contribution of variations in the gaps between the electrodes to the nonuniformity of the calorimeter is no more than 0.3% [93]. In addition, a small sample of 36 high energy delta ray electron candidates have been

identified within the cosmic sample, allowing a first *in situ* examination of electron shower shapes and identification criteria [94].

The first beam-related events seen by ATLAS in September 2008 were the so-called *beam splash* events. For these, a proton beam was deliberately stopped on a collimator placed about 140 m from the detector, producing large numbers of secondary particles, mainly pions and muons. These deposited several hundred TeV of energy throughout the calorimeter, giving a strong signal over the whole volume for the first time. As the particles arrived coherently, it was also an opportunity to check the timing of the detector, which matched expectations to within 2 ns [93].

Chapter 5

Electron reconstruction and triggering in ATLAS

In this chapter, both the reconstruction and triggering of electrons within ATLAS are described. Whilst triggering is chronologically the first process, many parts of the trigger selection (especially in the HLT) derive from the offline reconstruction, which will therefore be described first, in Section 5.1. Details concerning the electron trigger are then given in Section 5.2.

5.1 Electron reconstruction

The detection and identification of electrons and photons is critically important if ATLAS is to fulfil its primary physics aims. However, the conditions of collisions at the LHC make this significantly harder than in previous experiments. For example, the relative rate of QCD jet production compared to inclusive electron production is expected to be between 10 and 100 times higher than at the Tevatron [53, Section 10.4]. In addition, aspects of the detector itself complicate the analysis, such as the significant amounts of material in the Inner Detector (see Section 4.3). The strategies for reconstructing and triggering electron and photon candidates are described in detail in [42], although further improvements have been made in the cluster energy reconstruction since that report was published. As far as is possible, these strategies have been evaluated using test beams of electrons, photons and pions (see Section 4.4) and through detailed simulations. Ultimately, these strategies will be tested using collision data.

The reconstruction and identification of electrons and photons consists of four steps:

1. Identification of suitable energy deposits (cluster seeds) in the calorimeter.
2. Track reconstruction and matching to the cluster seeds.
3. Full calorimeter cluster reconstruction.
4. Application of identification cuts to the electron or photon candidates.

The parameters (p_{T}, η, isolation, *etc*) associated with each electron candidate are fixed after step 3. In step 4, identification cuts are applied, but the candidates themselves are not otherwise altered. To reflect this difference, a distinction will often be made between electron *reconstruction* (steps 1-3) and electron *identification* (step 4).

The descriptions in this chapter will focus on the reconstruction and identification of electrons, but many of the steps are performed identically for photon reconstruction. This is because electrons and photons produce similar-looking electromagnetic showers in the calorimeters. The presence of an associated track is the principal discriminating factor between the two cases. Where appropriate, some aspects of photon reconstruction will also be described.

The algorithm described here is the principal reconstruction method for electrons with a high p_{T} which are spatially separated from other particles in the event. A different algorithm exists, optimised for identification of electrons within jets. This algorithm is not considered further here, for more details see [42].

5.1.1 Cluster seed reconstruction

The first step in reconstructing a calorimeter cluster is to locate suitable cluster seeds. This is done using a sliding window algorithm [95] within the precision region of the calorimeter ($|\eta| < 2.5$). The seeds are rectangular, with a size of 5 cells by 5 cells, which corresponds to $\Delta\eta \times \Delta\phi = 0.125 \times 0.125$ over most of the calorimeter. The algorithm finds local maxima of the energy deposited within this size of window, and passes these cluster seeds on to the next stage in the reconstruction.

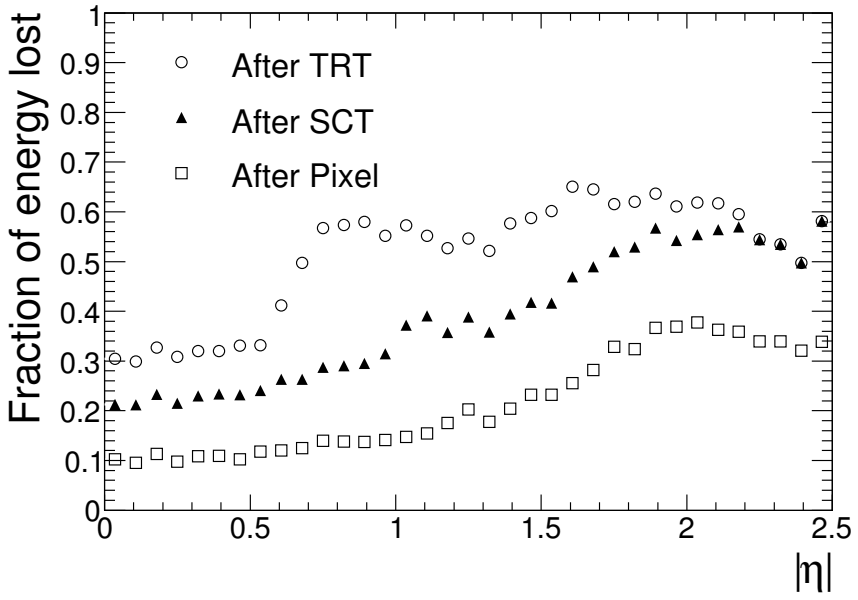

Figure 5.1: Fraction of energy lost on average by electrons with $p_{\mathrm{T}} = 25$ GeV/c after the different ID components as a function of $|\eta|$. From [53]

5.1.2 Track reconstruction and association

Inner Detector tracking is described in detail in Section 10.2.1 of [53], with further technical information in [96]. The process begins with the identification of seed tracks using the Pixel detector and the first layer of the SCT. Additional hits from the SCT are then added to these seeds using a loose selection to form a track candidate. At this point, the candidate track is fitted using a Kalman filter technique. Once this is done, outlying points are removed, ambiguities are resolved and tracks deemed to be fakes are dropped. Finally, the remaining tracks are extrapolated to the TRT and refitted using the calibrated drift circles. Any unused TRT track segments can also be extrapolated back into the SCT in an attempt to locate secondary tracks which may arise from photon conversions or long-lived particle decays.

One of the main difficulties in tracking electrons within the Inner Detector is the high probability of bremsstrahlung occurring within the subdetector volume. High p_{T} electrons typically radiate between 20% and 50% of their energy (depending on $|\eta|$) before leaving the SCT, as seen in Figure 5.1. The radiated photons typically end up very near to the electron energy deposit in the calorimeter, and thus may not be separately resolved. Track reconstruction for electrons may be improved in the future

Table 5.1: Reconstruction window sizes for different classifications of electron and photon candidates. The window granularity (*ie* 1 unit square) is 0.025×0.025 in $\Delta\eta \times \Delta\phi$.

Location	Candidate type	Window size
Barrel	Electron	3×7
	Photon	3×5
	Converted photon	3×7
Endcap	All types	5×5

by using dedicated fitting algorithms, as described in Section 10.2.5 of [53], although these improvements are only significant for electrons with transverse momenta less than approximately 25 GeV/c.

If a cluster seed is associated with a reconstructed track, an electron candidate is formed, or else a photon candidate is formed. This association places a very loose requirement on the spatial separation ($\Delta\eta < 0.05$ and $\Delta\phi < 0.1$) between the cluster and the track. In addition, the ratio E/p of the cluster energy and the track momentum must be less than 10, in order to avoid association with very low momentum tracks probably unrelated to the cluster. If, however, the associated track(s) are consistent with a photon conversion, the cluster seed is deemed to be a converted photon candidate, not an electron.

5.1.3 Full cluster reconstruction

Full reconstruction of the deposits in the electromagnetic calorimeter occurs after electron/photon classification to allow for different optimisations to be used in each case, as described in [95]. Energy deposits are summed to produce clusters in windows which are rectangular in $\eta - \phi$ space. Each choice of window size is optimised as a trade-off between efficient collection of all deposited energy and the reduction of spurious signals, mostly due to noise and pile-up. The window sizes are listed in Table 5.1. In the barrel, electrons and conversions are given wider windows in the ϕ direction to allow for the curvature caused by the magnetic field. This field is weaker in the endcaps, meaning that the windows can all have the same ϕ size regardless of classification.

The calculation of the position and energy after cluster formation is described in detail in the "Calibration and Performance of the Electromagnetic Calorimeter" chap-

ter of [42], with more detail on the energy calibration in [97]. The energy and position of the cluster are corrected for known systematic effects. In the case of the position (η and ϕ), these corrections mainly arise from the finite cell granularity. For the energy calculation, deposits of energy in inactive detector components also need to be accounted for. Expressed briefly, the energy of the cluster is

$$E = E_{\text{cal}} + E_{\text{front}} + E_{\text{back}}, \tag{5.1}$$

where E_{cal} is the energy deposited within the calorimeter, and the other two terms describe energy lost before entering the calorimeter and leaking out of the rear, respectively.

The calorimeter term, E_{cal}, includes a position-dependent calibration factor, and takes account of energy deposited outside the cluster. Both of these corrections vary as a function of the depth of a given cell within the calorimeter and the cluster position in η, but are relatively independent of energy.

The energy lost in front of the calorimeter, E_{front}, is estimated from the depositions within the calorimeter presampler. Where the calorimeter is not instrumented with a presampler ($|\eta| > 1.8$), this component is estimated from the observed shower depth in the calorimeter instead.

The final component, E_{back}, is parameterised again as a function of the shower depth X and position in η. It includes a term proportional to e^X, which represents the rapidly increasing effect of leakage in showers which penetrate more deeply into the calorimeter.

Once all corrections have been made, the energy of the electron candidate is deemed to be the energy of the cluster, as this is a better measure of the true electron energy for high p_{T} electrons than the momentum measurement obtained from the tracking. The Inner Detector however provides a superior angular measurement, and is used to define the η and ϕ coordinates of the candidate. Therefore, the measured p_{T}[10] uses a combination of the calorimeter and tracking information:

$$p_{\text{T}}^{\text{e}} = \frac{E_{\text{clus}}}{\cosh(\eta_{\text{track}})}. \tag{5.2}$$

[10]This combined measurement of the electron transverse momentum will be referred to as p_{T} throughout, reserving E_{T} for the equivalent measurement using the calorimeter alone.

At this point, the electron reconstruction *per se* is complete. All that remains is to apply selection cuts in order to reduce the number of background candidates to acceptable levels, a choice which will be analysis-dependent. This stage is called *identification*.

5.1.4 Electron identification

After reconstruction, the signal to background ratio for electrons is still small. To illustrate this, some results using the filtered sample introduced in Section 3.1.1 are presented here, pending further discussion in Chapter 7. Recall that this sample includes all anticipated sources of reconstructed electrons with $p_{\mathrm{T}} \gtrsim 17$ GeV, which are then filtered to improve the simulation efficiency. In this sample the contribution of electrons from W, Z/γ^* or t decays[11] only accounts for approximately 1 in 10^3 of the total electron candidates with $p_{\mathrm{T}} > 20$ GeV, most of which originate from hadrons wrongly identified as electrons. To improve the signal to background ratio, standard sets of electron identification cuts are applied, which are described in this section.

The largest single background source is from hadronic jets. In many cases, a single charged pion, kaon or proton produces a track in the Inner Detector, which is then associated with a cluster in the EM calorimeter. In other cases, the reconstructed track has no clear origin, but is formed by a combination of hits caused by multiple charged particles or noise. In addition, many real electrons are produced in photon conversions and Dalitz decays of pions. Real electrons from b and c decays are also present, and are expected to form an important background to the $Z/\gamma^* \to e^+e^-$ signal.

The standard ATLAS electron selection consists of a series of simple cuts on variables capable of discriminating signal electrons (*ie* high p_{T} isolated electrons) from these various background sources, and hence provides a robust selection for early analyses. In the long run, electron selection performance may be optimised through the use of multivariate techniques.

A total of 20 variables are considered for selection, based on measurements in the Calorimeter and Inner Detector. The cut values have been optimised as a function of

[11] These will frequently be referred to as *isolated* electrons, as they are typically well separated spatially from other particles in the event

Table 5.2: Variables used for electron identification in cut-based scheme. Where cuts vary as a function of the electron p_{T} and $|\eta|$, the range of cut values is given. The superscripts on E or E_{T} refer to the sampling used (or the whole electromagnetic cluster if no subscript is used), while $n \times m$ refers to rectangular windows of n by m cells. In the first sampling, "max2" refers to the strip with the second highest distinct maximum energy deposit, while "min" refers to the strip with the minimum energy between the maximum and the second maximum. "HThits" refers to high threshold hits in the TRT (see Section 4.3).

			Cut description	Symbol	Cut range
LOOSE			Cluster pseudorapidity	$\lvert\eta^{\mathrm{clus}}\rvert$	< 2.47
			Hadronic leakage	$E_{\mathrm{T}}^{1,\mathrm{had}}/E_{\mathrm{T}}$	$<$ (0.015-0.045)
			Shower width in η	$R_\eta = E^2_{3\times7}/E^2_{7\times7}$	$>$ (0.600-0.910)
			Shower width in ϕ (γ only)	$R_\phi = E^2_{3\times3}/E^2_{3\times7}$	$>$ (0.65-0.92)
			Lateral shower width in 2^{nd} layer	$w_{\eta 2c}$	$<$ (0.0125-0.025)
	MEDIUM		Peak signal in first layer	$\Delta E_{\mathrm{s}} = E^1_{\mathrm{max2}} - E^1_{\mathrm{min}}$	$<$ (0.1-0.3 GeV)
			Deposit in first layer	$R_{\mathrm{max2}} = \frac{E^1_{\mathrm{max2}}}{(1\mathrm{GeV}-0.009E_{\mathrm{T}})}$	$<$ (0.25-0.53)
			Shower width in 1^{st} layer	w_{stot}	$<$ (1.40-4.00)
			Shower width in 3 strips around max. in 1^{st} layer	w_{s3}	$<$ (0.60-0.80)
			Fraction of energy within seven strips in first layer, excluding central 3 strips	F_{side}	$<$ (0.20-0.80)
			N_{hits} in pixels	N_{Pix}	≥ 1
			N_{hits} in pixels and SCT combined	N_{Si}	≥ 9
			Transverse impact parameter	d_0	< 1 mm
			Lateral isolation	$R_{\mathrm{isol}} = E_{\Delta R<0.2}/E$	$<$ (0.20-0.8)
			$\Delta\eta(\mathrm{clus},\mathrm{track})$ in 1^{st} calorimeter layer	$\Delta\eta$	< 0.005
			N_{hits} in pixel b-layer	$N_{\mathrm{b-layer}}$	≥ 1
			$\Delta\phi(\mathrm{clus},\mathrm{track})$ in 2^{nd} calorimeter layer	$\Delta\phi$	< 0.02
			$E^{\mathrm{cluster}}/p^{\mathrm{track}}$	E/p	$>$ (0.70-0.80)
			$E^{\mathrm{cluster}}/p^{\mathrm{track}}$	E/p	$<$ (2.5-5.0)
			N_{hits} in TRT	N_{TRT}	No cut
			$N_{\mathrm{HThits}}/N_{\mathrm{hits}}$ in TRT	R_{TRT}	$>$ (0.08-0.155)

the measured E_{T} and $|\eta|$ of the electron, with up to six bins in the former and seven in the latter. The cuts can all be applied independently, or in groups, to give standard "loose", "medium" and "tight" selections. These have applications in different analyses, with different requirements in terms of signal efficiency and background rejection. The cuts themselves are summarised in Table 5.2, which also shows how the three standard selections are defined. The main characteristics of each selection are:

Loose: Basic anti-hadron selection, using cuts on the shower size and hadronic (longitudinal) leakage.

Medium: Extra rejection of $\pi^0 \to \gamma\gamma$ and photon conversions using extra calorimeter variables. A cut on the lateral isolation reduces backgrounds from electrons within hadronic jets. Rejection of poorly reconstructed tracks using basic track quality cuts.

Tight: Stricter track quality criteria, including matching with the cluster in ϕ and transition radiation information.

5.1.5 Reconstruction and identification performance

Some indicators of electron reconstruction quality are shown in Figure 5.2. This shows the resolution in p_{T} (defined in Equation 5.2), η and ϕ (from the track) in simulated $Z/\gamma^* \to e^+e^-$ events, as well as some example residual distributions. The residuals in each bin are iteratively fitted with a Gaussian, within the range $[\mu - n\sigma, \mu + m\sigma]$. The fit range is restricted in order to reduce the effects of non-Gaussian tails on the calculation. For η and ϕ, $n = m = 2$ (although for ϕ, a uniform constant has also been added to the Gaussian, to improve fit quality). In the case of p_{T}, $n = 1$ and $m = 2$ are used, which avoids the significant bremsstrahlung effects contributing to the low p_{T} tail. It is expected that in the future dedicated track-fitting procedures, aimed at identifying where bremsstrahlung occurs, will be applied to improve the quality of the electron reconstruction [98] (also see Section 10.2.5 of [53]).

The p_{T} resolution is dominated by the calorimeter energy measurement, and is generally around $2 - 3\%$ for electrons with mid-range p_{T} values around 30-50 GeV/c. The resolutions in η and ϕ are generally very good, better than 1×10^{-3}, varying

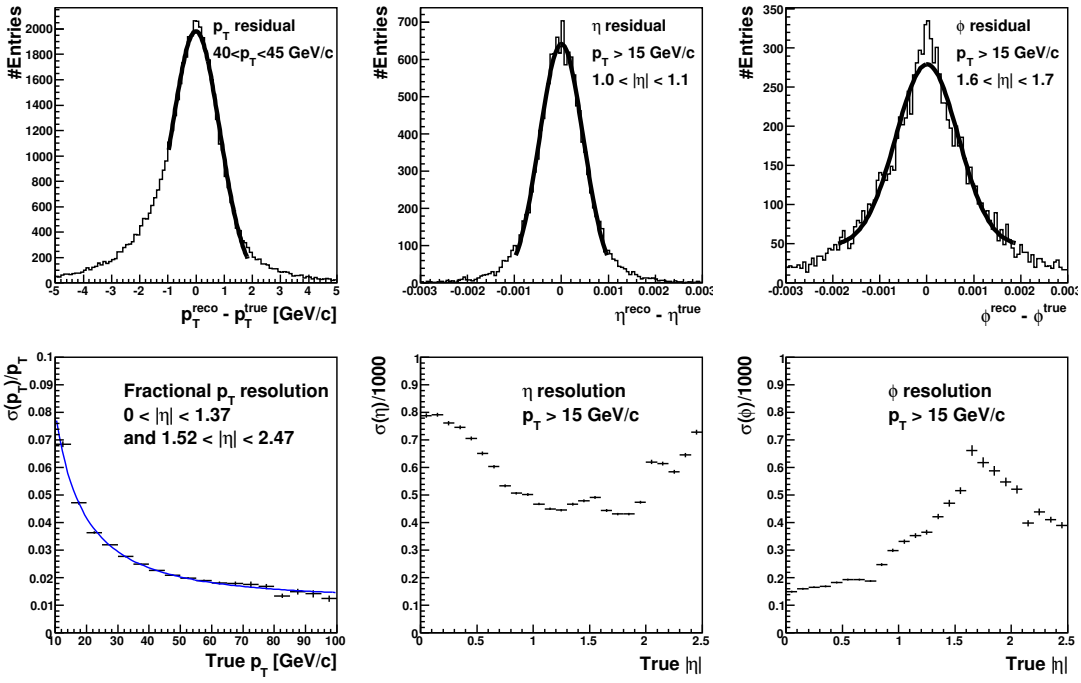

Figure 5.2: Reconstruction performance of electrons in a sample of simulated $Z/\gamma^* \rightarrow e^+e^-$ events. Top row: p_{T}, η and ϕ residual distributions (from left to right). Bottom left: Fractional p_{T} resolution as a function of p_{T}, for electrons outside the barrel-endcap transition region of $1.37 < |\eta| < 1.52$. Bottom middle and right: Resolutions of η and ϕ as a function of $|\eta|$, for electrons with a reconstructed $p_{\mathrm{T}} > 15$ GeV/c.

over $|\eta|$. The measurement in ϕ is very good in the barrel, and somewhat poorer in the endcaps, where the increased amounts of Inner Detector material increase the probability of bremsstrahlung and makes this particular measurement more difficult.

The expected performance of the electron identification cuts is documented in detail in the "Reconstruction and Identification of Electrons" chapter of [42]. On average, the identification efficiencies for electrons in $Z/\gamma^* \rightarrow e^+e^-$ events are 88%, 77% and 64% respectively for loose, medium and tight selection cuts. The expected rejection factors for jets with $E_{\mathrm{T}} > 17$ GeV are 570, 2200 and $9{\times}10^4$, again for the loose, medium and tight selections in turn. These cuts therefore cover a range of different efficiency and purity requirements, suitable for a wide range of different physics studies.

Figures 5.3 and 5.4 show the expected composition of the electron p_{T} and η spectra before and after the application of identification cuts, for high p_{T} electrons. Without any further event selection, the QCD background dominates at every stage until the tight cuts are applied, where real electrons from c and (especially) b decays dominate the

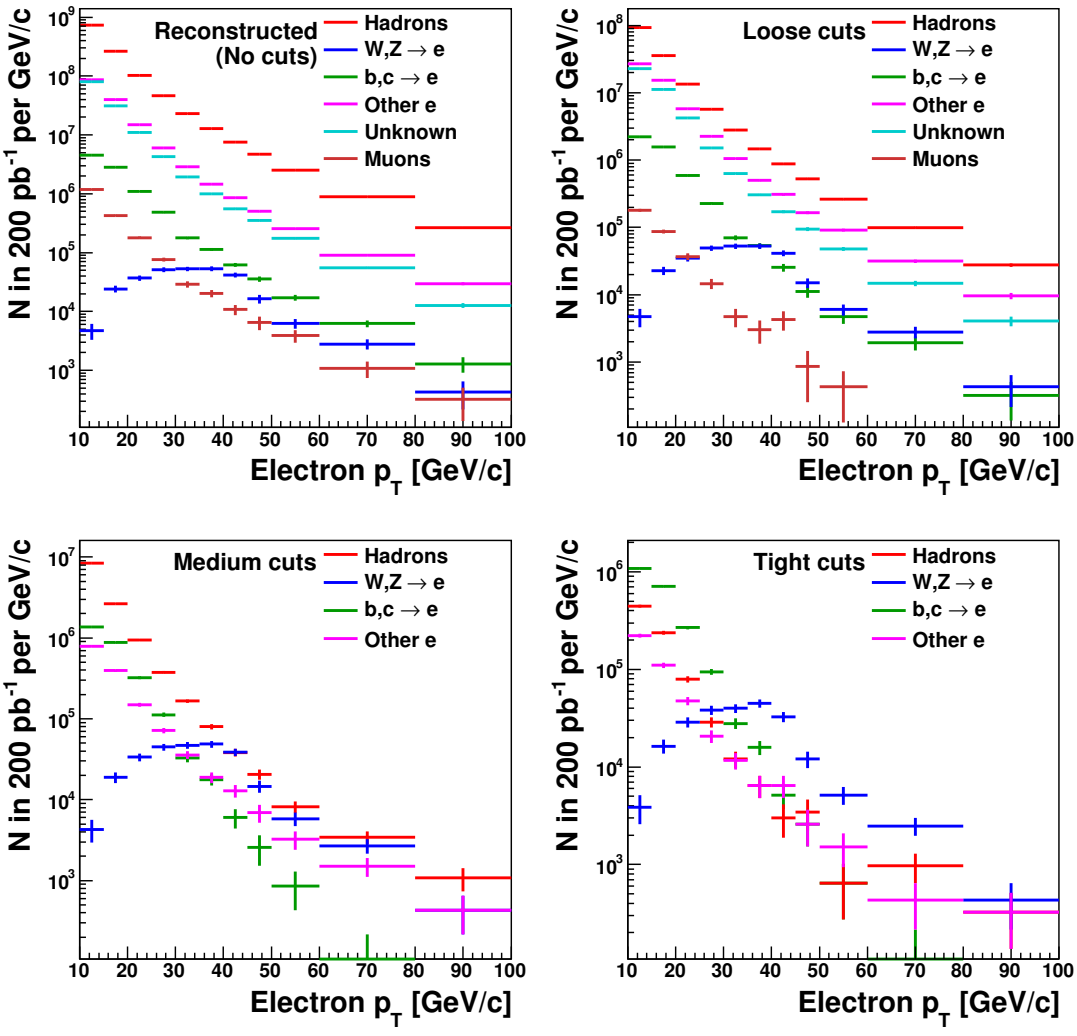

Figure 5.3: Predicted p_{T} spectra of reconstructed electrons, classified according to their true origin. Candidates are shown immediately after reconstruction (top left), and after the loose (top right), medium (bottom left) and tight (bottom right) selections. Candidates labelled "Unknown" could not be associated with any particular truth particle.

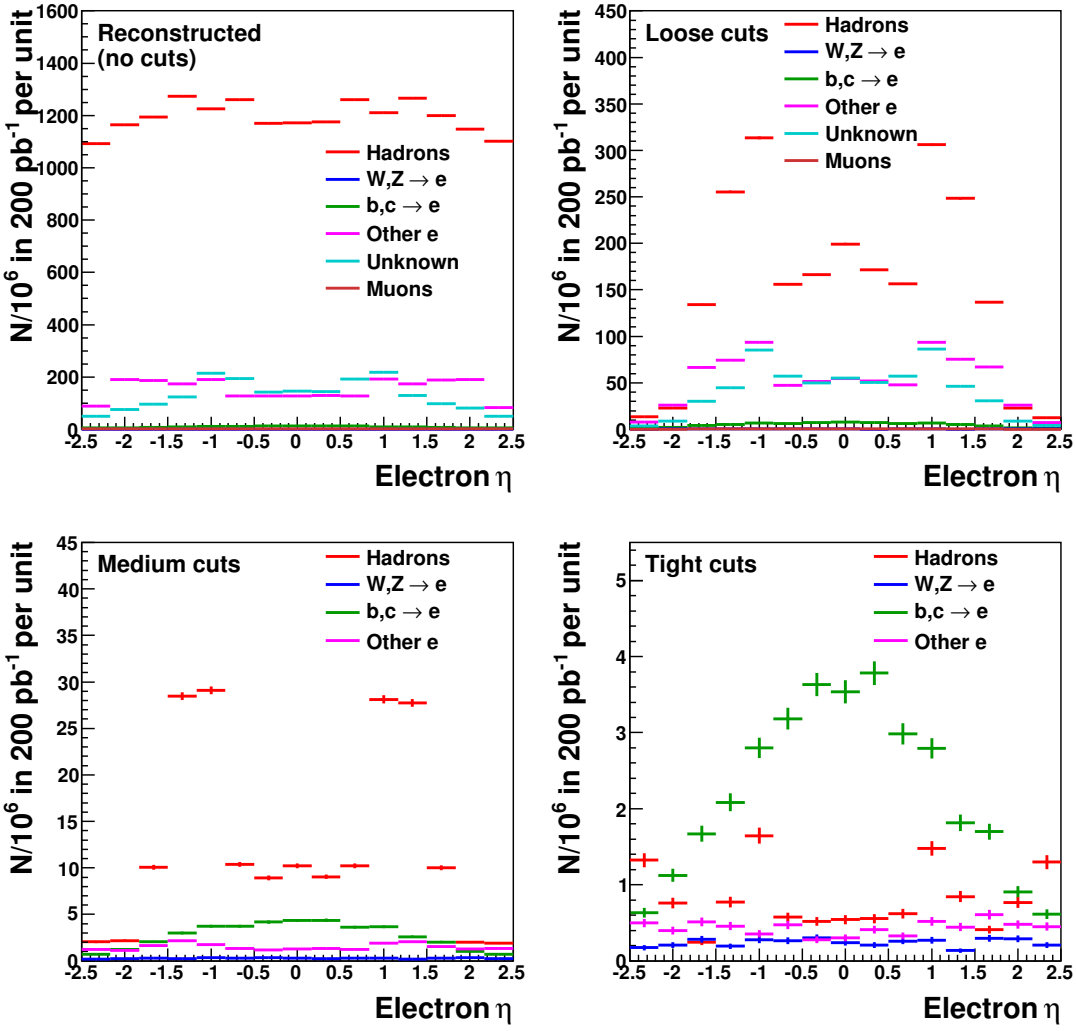

Figure 5.4: Predicted distributions in η of reconstructed electrons, classified according to their true origin. A preselection of $p_{\mathrm{T}}^{\mathrm{e}} > 10$ GeV/c has been applied. Candidates are shown immediately after reconstruction (top left), and after the loose (top right), medium (bottom left) and tight (bottom right) selections. Candidates labelled "Unknown" could not be associated with any particular truth particle.

rate at low p_{T}, while isolated electrons dominate at high p_{T}. To proceed further, more analysis-specific selections are required, which will not be discussed in this chapter.

5.2 Triggering on electrons

At the start of LHC running, approximately a quarter of the available trigger rate in ATLAS will be devoted to selecting electron- and photon-like signatures. In this section, the strategies for the online identification of electrons and photons will be described, following on from the general description of the trigger system in Section 4.7. Electron triggers are central to the ATLAS trigger strategy because high p_{T} electrons are typically associated with relatively rare processes, such as electroweak boson production or physics beyond the Standard Model, rather than QCD-mediated interactions.

The triggers used during data-taking (the *menu*) will vary over time. For example, initially loose trigger selections will need to become tighter as the instantaneous luminosity increases, so as to stay within the limits on the event rate that can be passed between trigger levels. There will also be triggers which run L2 and/or the EF in *pass-through* mode, in which case the RoIs are analysed as normal but no events are rejected. This allows the evalulation of the trigger selections involved. At higher luminosities ($\sim 10^{33}$ cm^{-2}s^{-1} and above), the full trigger selection will need to be applied, especially for low threshold triggers. A selection of looser triggers will remain for monitoring purposes, but these will be heavily prescaled.

Note on trigger chain notation

In this chapter and those that follow, the different triggers are referred to by the names of the relevant *item* (at Level 1) or *chain* (in the HLT, which consists of Level 2 and the Event Filter). These names contain information relating to the trigger level concerned, the E_{T} threshold, isolation applied at Level 1, and the selection applied in the Event Filter. See Table 5.3 for some examples.

The naming pattern for a Level 1 item is L1_NEMXXI. Here, N is the required RoI multiplicity (omitted if $N = 1$), "EM" indicates that this is a trigger for electrons and photons, XX is the E_{T} threshold cut (in GeV) and the optional "I", if present, indicates that isolation cuts were applied.

Table 5.3: Anticipated electron trigger chains for different instantaneous luminosities.

$\mathcal{L}$ / cm^{-2}s^{-1}	Level 1	Level 2	Event Filter
10^{31}	L1_EM7	L2_e10_medium	EF_e10_medium
10^{31}	L1_EM18	L2_e20_loose	EF_e20_loose
10^{32}	L1_EM18	L2_e20_medium1	EF_e20_medium1
10^{33}	L1_2EM7	L2_2e12_tight	EF_2e12_tight
10^{33}	L1_EM18I	L2_e22i_tight	EF_e22i_tight

The naming pattern for the electron triggers in the Event Filter is EF_$NeXX$i_sel, following on from the Level 1 name, and *sel* describes the selection cuts used, either "loose", "medium" or "tight". Level 2 chains have the same name as the EF chain which follows, except they are prefixed with "L2_".

5.2.1 Level 1

As explained in Section 4.7, the Level 1 trigger has no access to tracking information from the Inner Detector. Thus, electron trigger selection at this level is based entirely on the calorimeter, and cannot distinguish between electrons and photons. The EM calorimeter within $|\eta| < 2.5$ is divided into trigger towers of dimension $\Delta\eta \times \Delta\phi = 0.1 \times 0.1$, as was illustrated in Figure 4.8. In total, there are approximately 3100 such towers. A *Region of Interest*, or RoI, consists of four trigger towers arranged in a 2×2 square, with an associated isolation region surrounding these. This RoI and the corresponding extension into the hadronic calorimeters is shown in Figure 5.5. The first step in the Level 1 electron and photon triggers is to identify all suitable RoIs, *ie* those where the energy deposited in the four central towers is a local maximum.

Within an RoI, four possible 1×2 or 2×1 clusters exist (indicated by the Σ signs in Figure 5.5). The principal defining feature of an electron or photon trigger at Level 1 is the minimum transverse energy which must be deposited within this region. For the RoI to be selected, at least one of these four smaller clusters must have sufficient energy to pass this threshold.

At this point, optional isolation criteria may also be applied. The purpose of these is to reject electromagnetic clusters that are associated with jets, which are unlikely to contain electrons and photons from the primary vertex. These cuts therefore will also

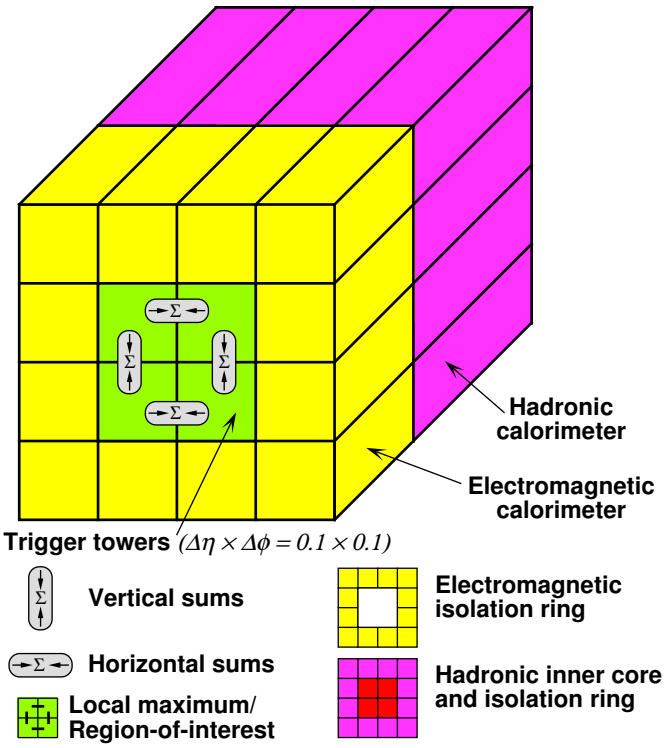

Figure 5.5: Clusters used for the L1 EM and τ triggers, showing the relative positions of the central cluster and the three isolation regions. Figure taken from [53].

remove electrons produced from the decays of b and c quarks, which are typically closely associated with jets. For very energetic electrons, the probability of the electromagnetic shower penetrating into the hadronic calorimeter is increased, and in this case applying isolation criteria may also not be appropriate. However, in the low- to mid-E_{T} range, requiring isolation will be essential at higher luminosities in order to keep the Level 1 pass rate within acceptable bounds.

Three types of isolation cuts may be applied to an RoI. In each case, the transverse energy deposited in a given region must be less than a specified threshold. Studies have shown that the isolation energies are reasonably insensitive to the total shower energy, so taking the ratio of these energies with that of the central RoI is unnecessary, while being detrimental to the timing performance of the Level 1 trigger. The three types of isolation are:

EM isolation The 12-tower ring surrounding the RoI in the EM calorimeter. These are shown in yellow in Figure 5.5.

Hadronic core isolation The 4 towers immediately behind the RoI in the hadronic

calorimeter (red in Figure 5.5).

Hadronic ring isolation The 12 towers immediately behind the EM isolation towers (pink in Figure 5.5).

The four RoI requirements (RoI transverse energy and the three isolation criteria), together with an RoI multiplicity threshold and prescale (if applicable), make up a Level 1 EM/tau *item*, of which a maximum of 16 may be defined. Typically, 8 of these will be used for electron and photon triggers, leaving the remaining 8 items for hadronic tau triggers.

5.2.2 Level 2

As described in Section 4.7, the Level 2 trigger is typically seeded by the Level 1 RoIs. The RoI at Level 2 is defined by a rectangular window of size $\Delta\eta \times \Delta\phi = 0.4 \times 0.4$ around the seed. Within the RoI, a calorimeter cluster is reconstructed with a cluster size of $\Delta\eta \times \Delta\phi = 0.075 \times 0.175$. As with the offline reconstruction, the size in $\Delta\phi$ is larger than that in $\Delta\eta$ to allow for the effects of curvature in the magnetic field.

Once the calorimeter cluster is reconstructed, certain selection criteria are applied before track reconstruction takes place, to optimise the execution time of the algorithm when running online. The exact selection criteria vary between different trigger chains, but the calorimeter variables used are similar to those used in the offline selection. Further details are given in the electron trigger chapter of [42].

Custom tracking algorithms are used at Level 2, designed to reduce combinatorial complexities to a manageable level given the 40 ms Level 2 trigger latency. These algorithms find tracks inside each RoI. Once candidate tracks are found, a Kalman filtering technique is used to improve the position and momentum resolution of these tracks. The primary vertex is also fitted, although the vertex information is not used in the triggers considered here.

The final step in selecting a Level 2 RoI for further processing involves requiring a sufficiently good match between the closest-matching track and the calorimeter cluster. To evaluate this, the track is extrapolated to the calorimeter position, and the resulting separation in $\eta - \phi$ space is calculated. In mid- to high-luminosity running, the ratio

$E_{\mathrm{T}}/p_{\mathrm{T}}$ will also be used, where E_{T} refers to the transverse energy measured in the calorimeter and p_{T} refers to the transverse momentum of the reconstructed track. This last variable will not be used in early data-taking due to uncertainties in the effect of bremsstrahlung, which widens and distorts the tails of the electron $E_{\mathrm{T}}/p_{\mathrm{T}}$ distribution.

5.2.3 Event Filter

As for Level 2, the Event Filter (EF) electron algorithms are seeded by the results of the previous trigger level. The EF electron selection has been based on the offline electron reconstruction and identification, albeit with some necessary simplifications to accommodate for the limited latency of around 4 s. For example, only information from the EM calorimeter is used, meaning that no hadronic leakage information is available for identification purposes.

At the EF, electron calorimeter clusters are made with a constant size of $\Delta\eta \times \Delta\phi = 0.125 \times 0.125$. As in the offline reconstruction, these clusters are corrected for known position-dependent calibration effects. Whereas Level 2 uses very fast, crude tracking algorithms, tracking in the EF is much more similar to the offline tracking. However, time-critical steps have been streamlined, to reduce unnecessary overheads for trigger operations.

Once suitable track/cluster candidates are located, they must pass selection cuts based on essentially the same variables as for the offline selection (Section 5.1.4). Typically, the actual cuts used are slightly looser to allow for the fact that the trigger will be less well calibrated. As in the offline reconstruction, loose medium and tight selection cuts are available, similar to those described in Table 5.2.

Chapter 6

The ATLAS computing model and analysis framework

With nearly 100 million channels being recorded up to 200 times per second, every aspect of ATLAS computing and data management will stretch current computing capabilities. In this chapter, the software available for the analysis of ATLAS data will be described. The ATHENA framework will be introduced in Section 6.1, together with a description of the ATLAS event simulation. This is followed by a short section on the LHC Computing Grid. In Section 6.2, the `LiverpoolAnalysis` package for physics analysis will be described, which was developed during the course of the analysis described in this thesis.

6.1 The ATHENA framework

ATHENA[12] [99] is the software framework used for the generation, simulation, reconstruction and analysis of ATLAS events. It is written in a highly modular style, primarily in C++ and python. Certain tasks are outsourced to external packages, such as file persistency (*ie* the creation of binary files which store data after a program finishes), which is managed by ROOT [100], augmented by POOL [101]. ATHENA is also compatible with Grid computing, to allow highly parallel processing of LHC data.

The ATLAS code is separated into semi-autonomous packages arranged in a tree-like structure, each dedicated to one particular aspect of event processing. For example, the `egammaTools` package contains all of the tools specific to electron and photon recon-

[12] A recent version of the ATHENA workbook explaining its structure may be found at `https://twiki.cern.ch/twiki/bin/view/Atlas/WorkBook`.

struction. The packages contain code which is organised into C++ and python *classes*, which are the basic building blocks of code.

There are four main categories of classes used within ATHENA:

Algorithms: Manage the process flow and use of the other three class types.

Tools: Encapsulated code for accomplishing one specific task, *eg* track extrapolation.

Data objects: Representations of detector elements and particles, usually stored in C++ containers compatible with the Standard Template Library [102].

Services: Provide access to data objects and tools.

These code categories are managed through the use of class inheritance, where a class implementing some analysis or simulation step will inherit from a base class which defines its categorisation. Although most algorithms, tools and services are written in C++, it is also possible for these to be written in python. Whilst these classes manipulate data and perform calculations, data objects merely hold information for transfer between different algorithms and tools. Data objects are managed by a transient data store called `StoreGate`, which is responsible for passing data between the algorithms, tools and services.

An ATHENA job is defined by a list of algorithms, running on a specified set of input files. The job flow is controlled by python scripts called *job options*. These create and configure the sequence of algorithms to be used in the job, as well as the tools and services which the algorithms require. They also define the input data file(s) and the type and location of any output. This python/C++ interface is very powerful, allowing generic algorithms and tools to be configured in many different ways, depending on the needs of the particular user. For example, trigger menus or the reconstruction sequence can be changed at run-time through modification of job options files, without recompilation of the C++ source code.

6.1.1 Event simulation and reconstruction in ATHENA

The steps involved in creating simulated ATLAS data are shown in Figure 6.1. Each step (except event generation) takes the output from the previous stage and processes

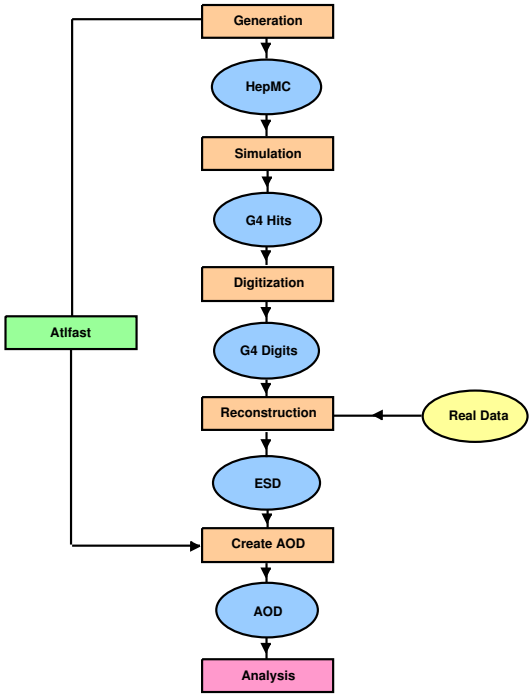

Figure 6.1: Schematic representation of the full ATLAS simulation, reconstruction and analysis chain.

it further before creating its own output file for further processing. This step-by-step approach allows event reprocessing at any point, without having to regenerate new events from scratch. The entry point for real collision data is also shown, as is the fast simulation Atlfast [103], which is not discussed in this thesis. Each step will now be briefly described.

Event generation

Events for collision and cosmic simulations are generated by various external programs, for which interfaces with ATHENA components have been developed. This means that, although each event generator may handle its input and output differently, all can be used in a similar way using ATHENA job options. The generators which can be used are too numerous to list individually, but vary from the commonly used PYTHIA [31, 30], HERWIG [32, 104] and MC@NLO [34] generators to other tools which are better for generating particular processes, such as AlpGen [105] for multi-parton processes and BlackMax [106] for black hole production.

The generated events are recorded in a file which follows the HepMC standard data

format [107], although wrapper classes exist which allow this record to be read using ATHENA data object classes. ATHENA also supports the filtering of the generated events, which can be used to improve simulation efficiency. Some of these filters were described in Section 3.1.1. The resultant HepMC files may be used for generator-level studies, as in Chapter 3, but more often they are then used as inputs for the detector simulation.

Simulation

Event simulation [108] involves modelling the paths of particles as they pass through the various detector components. This includes energy deposition, particle scattering, calorimeter showers and many other effects. This is handled by GEANT 4 [109], which is provided with a realistic description of ATLAS based on current knowledge of the installed components. The event simulation is very time-consuming, taking 10 or more minutes per event, and is generally managed centrally by the ATLAS collaboration. The output from this step is a file of "GEANT 4 hits", which amongst other things describe the energy deposited in each active element of the detector. In order to estimate the uncertainty in the detector performance, additional material and misalignments can be introduced, reflecting the limitations in the knowledge of the detector.

Digitisation

The digitisation step (also described in [108]) takes the GEANT 4 hits and simulates the response of the detectors and electronics to the passing particles or energy deposits. This includes the simulation of electronic noise, and channel-by-channel response variations. This step produces the "GEANT 4 digits" of Figure 6.1, which correspond to the raw channel-by-channel data output from the experimental hardware. This information is stored in a Raw Data Output (RDO) file.

Reconstruction

In the reconstruction step, data from an RDO file, either from the detector digitisation, or from the actual experiment, is interpreted in terms of particle interactions with the detector. The steps involved in reconstruction depend on the object of interest, and are described in detail elsewhere [42, 53], although the reconstruction of clusters and

tracks leading to electron candidates was discussed in Chapter 5. The output is a collection of tracks, calorimeter clusters and reconstructed particle candidates, and is called the ESD, or Event Summary Data. As the ESD contains a complete record of the event, it is quite large, nominally 1 MB per event. Therefore, a smaller summary of the data is also produced, called the AOD (Analysis Object Data). One event stored in AOD format is, on average, about one tenth of the size of an equivalent event stored in ESD format. Thus, the AOD can be copied to more locations worldwide on the Grid. Another, yet smaller, data summary format exists, called Derived Physics Data (DPD), the details of which will not be discussed here.

6.1.2 The LCG

Extensive use has been made of Grid computing in order to both produce and analyse the simulated data used in this thesis. The LHC Computing Grid (LCG [110]), commonly referred to as "the Grid", was developed as a worldwide computing infrastructure capable of supporting the data storage and analysis needs of the LHC experiments. The LCG model involves the hierarchical distribution of data around the world. The primary processing of collision data (*ie* event reconstruction) will take place at Tier 0, located at CERN. Reconstructed data, primarily in AOD and DPD format, will be distributed to national Tier 1 centres, which for the UK is located at the Rutherford Appleton Laboratory in Oxfordshire. Further subsets of data (primarily DPDs, except for simulated events) will be distributed to regional Tier 2 computing centres. Data disks and tapes at a particular location, available for Grid-based analysis, are called *storage elements*.

Apart from Tier 0, no single site is expected to have all collision data stored locally, even in AOD format. Instead, each storage element typically has one or more *computing elements* associated with it, for the processing of data at that storage element. Thus, analysis jobs are distributed over several computing elements in order to access all of the data. This computing model has been under test for several years, first with Monte Carlo simulation and more recently with cosmic and single beam data. ATHENA job submission is facilitated by the use of tools, such as Ganga [111], that allow large distributed analysis jobs to be submitted and monitored, and the results

downloaded for further processing locally. A typical job will run software which uses the ATHENA framework to analyse AOD files and summarise important information in a more compact format. This is described in the next section.

6.2 Analysis strategy

The `LiverpoolAnalysis` package [112] has been designed to analyse ATLAS data, in ESD, AOD or DPD format, while making the best use of the modularity and configurability of the ATHENA framework. Its classes are written to be as generic as possible, so that the same code may be used in different contexts depending on the analysis requirements. For example, it is currently used to study muon reconstruction performance, searches for the Higgs boson and supersymmetry, and Standard Model physics as described in this thesis. There are four main subpackages which make up `LiverpoolAnalysis`:

`LivTools:` ATHENA tools for specific analysis tasks, *eg* matching of trigger RoIs with offline particles.

`LivServices:` Common services for cut flows and event weight storage.

`LivAlgorithms:` Algorithms for performing calculations, usually using the tools in `LivTools`.

`LivDumpers:` Configurable output of ATHENA data object information to a ROOT NTuple.

There are, in addition, a number of analysis-specific subpackages which hold classes and job options relevant for particular analyses. For example, `LivZAnalysis` holds analysis code specifically written for analysis of the Z boson resonance. The `LivTools` package also contains python functions which automate some of the more routine job configuration.

The `LiverpoolAnalysis` classes are fully modular, each designed to do a single specific task. Amongst other things, this exploits the inheritance structures of ATHENA data object classes. For example, some tools match trigger RoIs to reconstructed particles using the distance parameter ΔR. Since all standard ATHENA particle classes

inherit from a common base class describing their 4-momenta (`INavigable4Momentum`), these tools do not need to know which kind of reconstructed particle is being matched. In other words, trigger RoIs can be matched to reconstructed muons, electrons or jets, all using the same tool. The final execution order of algorithms and tools is encoded in the job options, allowing easy insertion or substitution of analysis steps without recompilation of the C++ code.

In the following sections, the principal `LiverpoolAnalysis` classes used in and developed for the analyses in this thesis are described.

6.2.1 `LivTools`

The `LivTools` package contains the most generic code, for specific calculations and tasks needed many times per event. There are several distinct categories of tools, grouped by the sort of task they are designed to do. Each task is described by a tool *interface*, which describes the operations that those tools will perform. The tools then only differ in how they perform that task.

One group of tools are responsible for particle selection. Each tool takes a collection of particles and filters it, writing the list of successful particles to `StoreGate` for further analysis. Selection tools exist for electron, photon, muon, jet and hadronic tau candidates. Missing E_{T} requires a different treatment, as it is a property of the entire event. Particular cuts are written into the class code, but the cut values are fully configurable through the job options, allowing full control over the exact particle selection. Multiple independent selections can be made in parallel, which allows the simultaneous examination of the effect of different cuts and other complex operations.

Another group already mentioned consists of tools for trigger and offline particle association. Three tools exist: one for matching between offline particles (*eg* for jet-electron overlap studies), one for matching to HLT RoIs, and a third for matching to Level 1 electron and photon RoIs. Each tool manages one particular collection of objects, for instance selected particles of a particular type, or Event Filter RoIs which passed a particular trigger. These then take particles supplied by client algorithms and find the closest matching object in their collection, using separation in ΔR as the discriminating variable.

One of the other important tools deals with information provided by the event generator, called the `SingleBosonTruthTool`. This tool takes the truth-level particles and looks for a (user-defined) $1 \rightarrow 2$ decay, such as $Z/\gamma^* \rightarrow e^+e^-$ or $W \rightarrow e\nu_e$. Its main job is to provide convenient (one line) access to the particles involved in this reaction, namely the intermediary boson, colliding quarks and final state decay products, including radiated photons. The tool used for this thesis is only capable of reading events generated by PYTHIA, but it is currently being updated to make it capable of reading MC@NLO events.

Further tools exist for studies of particle isolation, impact parameters, smearing and recalibration. These are not discussed here.

6.2.2 `LivAlgorithms`

The classes in `LivAlgorithms` are needed because tools cannot be executed on their own, they must be called by some other component. Most algorithms in this package simply extract a collection of data objects, apply one or more tools to those objects, and record the results in `StoreGate`. Some others alter the job flow by signalling that the execution of a particular algorithm sequence should stop (for example, if no reconstructed particles pass selection cuts). The mapping of tools to algorithms is not necessarily one-to-one. For example, `ParticlePreselection` iterates through several selection tools and executes each in turn. As the selection tools are defined via their common interface, this one algorithm can in principle manage an arbitrary complex event selection. Separate algorithms exist for applying a trigger selection and selection based on missing E_{T} and related variables.

The main exception to this general pattern is the algorithm `Combine2Particles`. This uses existing ATHENA functionality to construct so-called composite particles, usually representing unstable intermediaries reconstructed from the 4-momenta of their decay products. Each composite particle (of which there may be more than one per event) is made of exactly two components, usually reconstructed particles. These component particles may be of the same type (*eg* for $Z/\gamma^* \rightarrow e^+e^-$), or of different types (*eg* $Z/\gamma^* \rightarrow \tau^+\tau^-$, where one τ decays hadronically and one leptonically). Composite particles are recorded in `StoreGate` for further analysis. Composite particles can

themselves be combined with other particles, so three instances of `Combine2Particles` can reconstruct the entire $H \rightarrow ZZ \rightarrow 2e2\mu$ decay chain for example, including the intermediate Z bosons. At the same time, cuts can be made on the mass and charge of the composite particles.

These are the algorithms most used in this thesis. Other algorithms exist for particular studies, such as the recalculation of electron and photon calorimeter clusters, and event reconstruction using the collinear approximation for τ leptons.[13]

6.2.3 `LivServices`

The `LivServices` package contains two services for the recording of data relevant to an entire event. One records a cut flow, and is designed to work with the `ParticlePreselection` algorithm described above. This records the number of events which pass each selection stage, producing a ROOT histogram and text file summarising the results. The other service stores user-defined event weights used in physics analysis.

6.2.4 `LivDumpers`

This package exists so that information about an event can be recorded in a ROOT tree for further analysis. The algorithms in `LivDumpers` can record information about reconstructed particles (electrons, photons, muons, jets, composite particles, *etc*), event level variables (missing E_{T}, trigger results, run/luminosity block, *pdf* information, *etc*) and some more detailed detector-level information (reconstructed tracks, calorimeter cells and clusters). Classes also exist which use the matching tools in `LivTools` to record the ΔR distances between various types of trigger RoIs and reconstructed particles, including the components of composite particles. Details of the objects themselves need to be recorded separately.

Each `LivDumpers` class is configurable, allowing full control of the level of detail recorded, including (for particles) basic kinematic information, variables used for particle identification, and so on. In addition, the job configuration controls the stage at which information is dumped (*ie* before/after preselection, after recalibration, *etc*) and controls the output file structure (*ie* one or several ROOT trees, or even several files).

[13] This is where the neutrino associated with a τ lepton decay is assumed to travel in the same direction as the original τ

Thus, the entire structure and content of the output tree(s) can be controlled through the job options, and need not be known until run-time.

6.2.5 `LivZAnalysis`

The classes already described are generic enough to perform most common analysis procedures. However, a small amount of analysis-specific code is still necessary. `LivZAnalysis` contains just three algorithms. Two are for specific ROOT tree dumps of $Z/\gamma^* \to e^+e^-$ and $Z/\gamma^* \to \tau^+\tau^-$ events, which record identification information for the components (electrons and taus respectively) of composite particles (reconstructed Z/γ^* bosons). In all other respects, they are similar to the classes in `LivDumpers`.

The final algorithm, `FullZeeMatching`, is used to relate the true Z/γ^* boson decay to reconstructed calorimeter clusters and electrons. This accesses the generator-level truth supplied by the `SingleBosonTruthTool` and records the matching clusters and electrons in `StoreGate`. It can also, if required, record some supplementary information, such as the ΔR distances between the true and reconstructed electrons, in a ROOT tree, in a manner compatible with the `LivDumpers` package.

Chapter 7

QCD backgrounds to electron identification

The reconstruction of electrons in ATLAS (described in Chapter 5) is designed to meet the challenging prospect of efficiently selecting real electrons from various sources while minimising the contamination from mis-reconstructed non-electrons. The identification cuts in Table 5.2 were developed for this purpose. In [42], it is estimated that the rejection power of the "medium" selection on jets with $p_{\mathrm{T}} > 17$ GeV/c is $\mathcal{O}(2000)$, which is sufficient for many applications. However, this high performance, in combination with the large jet cross section, requires very large numbers of simulated background events to ensure that sufficient numbers are left for a statistically meaningful background estimate once the signal selection cuts have been applied.

For example, assuming the above rejection power of 2000 for jets, approximately 4 million QCD jet events would need to be simulated to get just one event passing a basic $Z/\gamma^* \to e^+e^-$ event selection. Many more than this would be needed to properly estimate the background, at least several hundred million. This would require a large investment of time and computing resources (including storage of the simulated events), one which is too great at the present time.

Utilising Grid computing, approximately 9.5 million filtered events (principally QCD jet events) have been simulated, corresponding to an integrated luminosity of approximately 90 nb^{-1}. This sample contains all anticipated sources of reconstructed electrons, and is filtered for events likely to include reconstructed high p_{T} electrons as described in Section 3.1.1. Figure 7.1 shows the di-electron mass spectrum for events passing a basic $Z/\gamma^* \to e^+e^-$ selection. Both electrons must pass the "medium" electron

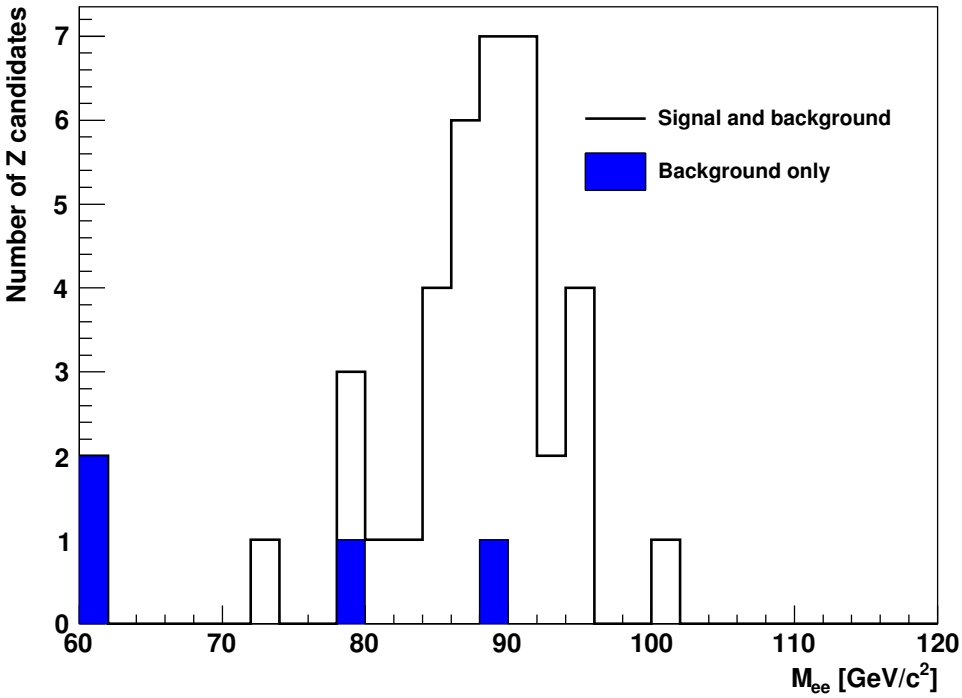

Figure 7.1: Direct application of Z/γ^* selection criteria to the filtered event sample. The line in black shows $Z/\gamma^* \rightarrow e^+e^-$ candidates, including signal events, while the blue histogram shows the background component. Both electrons must have a reconstructed p_{T} greater than 10 GeV/c and pass the "medium" electron selection. No other cuts have been applied, and the events have not been scaled.

selection cuts, in addition to a preselection of $p_{\mathrm{T}}^{\mathrm{e}} > 10$ GeV/c. The $Z/\gamma^* \rightarrow e^+e^-$signal can clearly be seen above the remaining background, which amounts to just four events with $M_{ee} > 60$ GeV/c^2.

Clearly, the QCD background for $Z/\gamma^* \rightarrow e^+e^-$ events must be estimated in some other way. In this chapter, an event scaling method based on the probability of single reconstructed electrons to pass identification cuts is presented, and shown to improve the statistical power of the filtered event sample. Firstly, in Section 7.1, a scheme for classifying the real origins of reconstructed electrons will be introduced. Then, in Section 7.2, the calculation of identification and triggering efficiencies will be described, followed by details of the event weighting method itself. The method is validated using very loose event selection criteria in Section 7.3, and results for more realistic event selections are presented in Section 7.4.

7.1 Sources of background in $Z/\gamma^* \to e^+e^-$ events

The filtered event sample used throughout this chapter, as mentioned above, includes all collision processes which are expected to give rise to high p_{T} reconstructed electrons or photons in ATLAS. The events are generated using PYTHIA for 10 TeV pp collisions before being run through the full ATLAS detector simulation. The generated processes include W, Z/γ^* and t production, which can of course give rise to real final-state electrons. Heavy flavour (b and c quark) decays to electrons are also included, as is single photon production. Finally, there are generic $2 \to 2$ QCD-mediated processes producing high p_{T} jets. After filtering, but before further cuts are applied, the last process dominates, due to the large QCD cross section.

It is important to understand the true origins of any reconstructed electrons, as different categories can have very different efficiencies. Each reconstructed electron is classified according to a scheme which uses the fact that they all have an Inner Detector track by construction. Individual hits on this track are matched to particles in the event history produced by the GEANT 4 detector simulation. Following [42], each electron candidate is classified as one of the following types:

Isolated electrons True electrons, originating from a W, Z/γ^*, t, τ or μ decay.

Unisolated electrons True electrons, originating from J/ψ, B or D meson decays.

Background electrons Electrons from other sources, including photon conversions, Dalitz decays of pions, and other baryonic or mesonic decays.

Hadron A hadron (eg $\pi^{\pm}$) reconstructed as an electron.

Muon A muon reconstructed as an electron.

Unknown A reconstructed electron candidate with no source that could be identified. In other words, the track is deemed to be fake.

These six classes are used and referred to throughout this chapter. Note that this classification says nothing about the origin of the calorimeter cluster, which in many cases will contain energy deposits from many particles within a hadronic jet.

Table 7.1: Yield before cuts of the different classes of electron candidates within the filtered event sample, and efficiencies for the electron identification cuts listed in Table 5.2. A p_{T} cut of 15 GeV/c has been applied. Numbers in brackets indicate the statistical uncertainty on the last digit(s).

Candidate type	Total #	$\epsilon_{\mathrm{Loose}}$/%	$\epsilon_{\mathrm{Medium}}$/%	$\epsilon_{\mathrm{Tight}}$
Isolated Electrons	707	97.2(6)	89.4(1.2)	78(2)%
Unisolated Electrons	11259	52.7(5)	28.3(4)	23.3(4)%
Background Electrons	157424	38.1(1)	1.04(3)	0.31(1)%
Hadrons	1091135	13.12(3)	0.915(9)	$8.1(3)\times10^{-4}$
Muons	1778	20.0(1.0)	0.4(1)	$< 6 \times 10^{-4}$
Unknown	117937	36.2(1)	0.003(2)	$8(8)\times10^{-6}$

7.2 Background estimation method

7.2.1 Efficiency and fake rate calculation

Reconstructed electrons from the different sources listed in Section 7.1 will in general pass the electron identification cuts with different probabilities. In the case of signal electrons, this probability is the signal selection efficiency, while for backgrounds it is a fake rate. The calculation of both quantities is identical, and they shall both be referred to as efficiencies for brevity. These efficiencies have been calculated using events from the filtered event sample where one or more electrons have been reconstructed. Here, "reconstructed" means that an electron candidate with $p_{\mathrm{T}} > 10$ GeV (p_{T} is defined in Equation 5.2) has been found that passes the standard ATLAS electron preselection. This eliminates any need to specifically calculate track association efficiencies for these electron candidates, or artificially assign a reconstructed charge. There are more than 1.3 million electron candidates in the sample as a whole at this stage.

The yields and averaged identification efficiencies for those candidates with $p_{\mathrm{T}} >$ 15 GeV/c are shown in Table 7.1. The identification criteria used in the table and elsewhere in this chapter were summarised in Table 5.2. It can be seen that each class of candidate electrons behaves differently under the selection cuts. As expected, isolated electrons are selected very efficiently, while hadrons and background electrons are rejected more stringently with each set of cuts. Unisolated electrons have a lower efficiency than isolated electrons because they are typically embedded within hadronic jets. The number of candidates which are really "Muons" or "Unknown" become negligible once the medium electron selection is applied, as this includes more stringent

shower shape and track quality cuts than the loose electron selection.

The identification efficiency for a preselected electron is calculated separately for each electron type using the following ratio:

$$\begin{aligned} \epsilon^e_{\rm id} &= \frac{N_{\rm identified}}{N_{\rm all}} \\ \delta\epsilon^e_{\rm id} &= \sqrt{\frac{\epsilon^e_{\rm id}(1-\epsilon^e_{\rm id})}{N_{\rm all}}}. \end{aligned} \tag{7.1}$$

For simplicity, standard binomial uncertainties have been used. To find the trigger efficiencies, trigger RoIs passing the required selection are matched to the offline electron candidates by requiring them to be located within a cone of $\Delta R < 0.1$ of each other.[14] This cut is chosen as it is comparable to the size of reconstructed clusters in the EM calorimeter, and an RoI clearly cannot be associated with the cluster if it is further away than this. The trigger efficiency is calculated with respect to the offline identification used:

$$\begin{aligned} \epsilon^e_{\rm t} &= \frac{N_{\rm id+trigger}}{N_{\rm identified}} \\ \delta\epsilon^e_{\rm t} &= \sqrt{\frac{\epsilon^e_{\rm t}(1-\epsilon^e_{\rm t})}{N_{\rm identified}}}. \end{aligned} \tag{7.2}$$

In general, identification and trigger efficiencies vary significantly as a function of the main kinematic variables of the event, such as the $p_{\rm T}$ and η of the electron candidate. In addition, the transverse momentum of the hard scatter in the centre of mass frame of the partonic collision (or $p_\perp$) is very important. The distribution of $p_\perp$ in the filtered event sample is shown in Figure 7.2, where it should be noted that the filtered events are generated with a cut of $p_\perp > 15$ GeV/c. In events with two reconstructed high $p_{\rm T}$ electrons, the $p_\perp$ distribution peaks at around 50 GeV/c, with a long tail out to high values of $p_\perp$, where the probability of reconstructing two high $p_{\rm T}$ electrons is greater.

Identification efficiencies for the "medium" electron selection are shown in Figure 7.3,[15] as a function of the calorimeter $E_{\rm T}$ and η, as well as the event $p_\perp$. The track information has not been used in the efficiency binning, as in many cases the track

[14] The distance ΔR is defined as $\sqrt{\Delta\eta^2 + \Delta\phi^2}$.

[15] Efficiencies for the "Muon" and "Unknown" electron types are not shown in the plots as they are considerably smaller than those illustrated. They are considered in the total background estimation nevertheless.

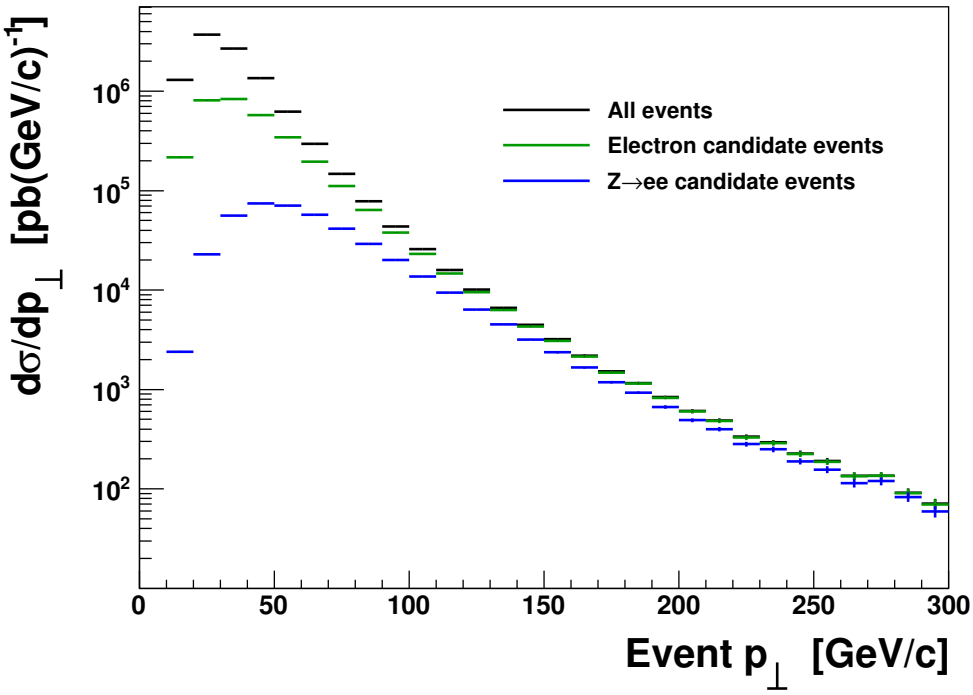

Figure 7.2: Distribution of the event $p_\perp$ variable in filtered events. The distribution is shown for all events in black, and those with at least one and two reconstructed electrons with $p_\mathrm{T} > 10$ GeV/c in green and blue respectively.

will be a poor match to the cluster. The efficiency for a hadron or unisolated electron to be identified shows a very clear downward trend as the electron E_T increases, although the hadron efficiency flattens out above 50 GeV. In contrast, the efficiency for background electrons is nearly flat over the whole E_T range. As a function of η, the efficiency for unisolated electrons is slightly lower in the endcaps than the barrel, while the hadron efficiency histogram shows some structure. This structure is caused by the hadronic leakage cut (see Table 5.2) being affected by the complex geometry of the barrel-endcap transition region. This issue has been fixed in more recent versions of the ATLAS software, where information from the whole hadronic calorimeter is used for this cut within the affected region, not just the first layer. The efficiencies are all symmetrical in η, suggesting that it would be sufficient to use $|\eta|$ instead, resulting in some statistical gain. All candidate types except isolated electrons show a very strong dependence on the event $p_\perp$ variable.

Figure 7.4 shows the e10_medium trigger efficiencies with respect to the medium electron selection. In comparison to the identification efficiencies in Figure 7.3, these

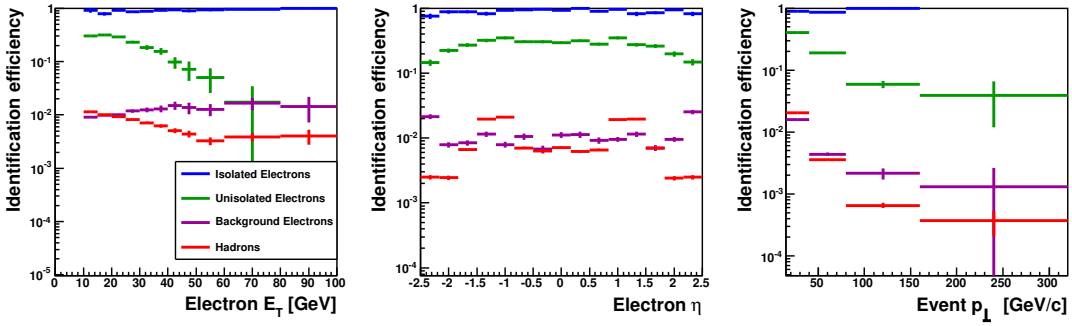

Figure 7.3: Combined selection efficiency for a "medium" electron selection (*cf* Section 5.1.4). Left: As a function of the reconstructed E_{T}. Middle: As a function of η, for electrons with $p_{\mathrm{T}} > 15$ GeV/c. Right: As a function of the event $p_{\perp}$, with the same p_{T} cut. See text for details on the event classification.

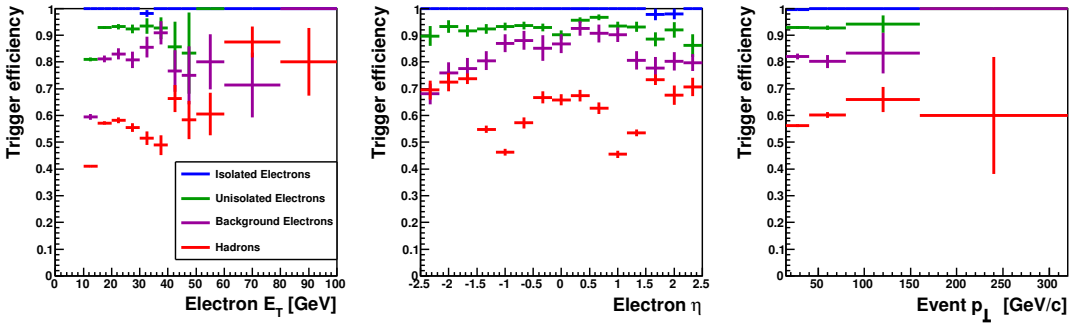

Figure 7.4: Efficiency of the e10_medium trigger for reconstructed electrons which pass the "medium" electron selection. Left: As a function of the reconstructed E_{T}. Middle: As a function of η, for electrons with $p_{\mathrm{T}} > 15$ GeV/c. Right: As a function of the event $p_{\perp}$, with the same p_{T} cut. See text for details on the event classification.

efficiencies are high and reasonably flat as a function of all the variables. They are relatively high because the trigger selection is very similar to the offline selection which has already been applied.

7.2.2 Event weighting method

Once identification and triggering efficiencies are calculated, they can be used to scale background events which have two reconstructed electrons. Of the nearly 9.6 million events in the simulated filtered event sample, over 104,000 di-electron pairs are produced which pass basic kinematic cuts of $p_{\mathrm{T}}^{\mathrm{e}} > 15$ GeV/c and $M_{ee} > 40$ GeV/c^2. As there are six electron classes described in Section 7.1, there are thirty-six possible combinations if the electrons are kept in p_{T}-ordered pairs. The full breakdown of the available electron pair candidates is shown in Table 7.2. Before further cuts, the largest individual contri-

Table 7.2: Yield of electron pairs in the filtered event sample used in this chapter. The classification refers to the terms defined in the text, where the row indicates the higher p_{T} electron candidate and the column the lower p_{T} candidate. A preselection of $E_{\mathrm{T}}^{e} > 15$ GeV and $M_{ee} > 40$ GeV/c^2 has been applied.

		Electrons			Non-electrons		
		Isolated	Unisolated	Background	Hadron	Muon	Unknown
Elec.	Isolated	46	1	1	20	0	3
	Unisolated	0	10	56	532	2	47
	Background	1	45	664	6810	16	604
Non-elec	Hadron	5	486	6120	75684	203	6423
	Muon	0	1	12	126	2	17
	Unknown	1	44	450	5495	11	525

bution comes from events where two hadrons are both mis-reconstructed as electrons. There are, in addition, some large off-diagonal components, in particular events where the ee pair consists of one hadron and one background electron.

Using the identification efficiencies described in Section 7.2.1, the probability for a given electron pair to be fully identified may be calculated as the product of the individual efficiencies:

$$\begin{aligned} \epsilon_{\mathrm{id}} &= \epsilon_{\mathrm{id}}^{e1}\ \epsilon_{\mathrm{id}}^{e2} \\ \delta\epsilon_{\mathrm{id}} &= \epsilon_{\mathrm{id}}^{e2}\ \delta\epsilon_{\mathrm{id}}^{e1}\ \oplus\ \epsilon_{\mathrm{id}}^{e1}\ \delta\epsilon_{\mathrm{id}}^{e2}. \end{aligned} \tag{7.3}$$

Here, $\oplus$ means that terms are added in quadrature (*ie* $A \oplus B = \sqrt{A^2 + B^2}$). The indices 1 and 2 refer to the two electron candidates, classified appropriately.

For an event to trigger using the trigger chains considered here, only one electron needs to pass the corresponding selection. The probability of this, given $\epsilon_{\mathrm{t}}^{e1}$ and $\epsilon_{\mathrm{t}}^{e2}$, is:

$$\begin{aligned} \epsilon_{\mathrm{t}} &= \epsilon_{\mathrm{t}}^{e1}\ +\ \epsilon_{\mathrm{t}}^{e2}\ -\ \epsilon_{\mathrm{t}}^{e1}\ \epsilon_{\mathrm{t}}^{e2} \\ \delta\epsilon_{\mathrm{t}} &= (1-\epsilon_{\mathrm{t}}^{e2})\ \delta\epsilon_{\mathrm{t}}^{e1}\ \oplus\ (1-\epsilon_{\mathrm{t}}^{e1})\ \delta\epsilon_{\mathrm{t}}^{e2}. \end{aligned} \tag{7.4}$$

Recalling that the trigger efficiency is calculated for electrons which have already passed the offline identification criteria, the total probability to fully identify and trigger the electron candidate pair as a $Z/\gamma^* \rightarrow e^+e^-$ candidate is the product of the above terms:

$$\begin{aligned} \epsilon &= \epsilon_{\mathrm{id}}\ \epsilon_{\mathrm{t}} \\ \delta\epsilon &= \epsilon_{\mathrm{t}}\ \delta\epsilon_{\mathrm{id}}\ \oplus\ \epsilon_{\mathrm{id}}\ \delta\epsilon_{\mathrm{t}}. \end{aligned} \tag{7.5}$$

Equations 7.3, 7.4 and 7.5 define the weight used for each electron pair. This is done separately for each of the truth-level classifications shown in Table 7.2, although those involving isolated electrons are not included in the final background estimate because these backgrounds are better estimated using dedicated Monte Carlo simulations. This also excludes real $Z/\gamma^* \to e^+e^-$ decays from the background count.

7.3 Validation

It is possible to test the scaling methods presented above by using a much looser selection than would be used in a real $Z/\gamma^* \to e^+e^-$ analysis. If this selection does not cut too hard on the background events, a statistically significant number will remain when these cuts are applied directly to the sample (in contrast to the example in Figure 7.1). There are three cuts that must be made sufficiently loose: the offline electron selection, the trigger selection, and the p_{T} threshold. Of the different offline selection choices, only the "loose" cuts are suitable, and the same logic rules out many of the trigger choices, such as e10_medium. Also, raising the p_{T} threshold has a dramatic effect on the number of successful electron pairs, due to the rapidly falling p_{T} distributions for the backgrounds.

For these trials therefore, a relatively low p_{T} cut of 15 GeV/c has been used. Either one or both electron candidates are required to pass the loose offline electron selection, but no trigger selection has been applied. The efficiency of the loose identification cuts for each type of electron has been binned two-dimensionally in two different ways. In both cases, the electron cluster E_{T} is one of these dimensions, while the other dimension is either the electron cluster $|\eta|$ or the event variable $p_\perp$ introduced in Section 7.2.1. The binning along each axis was chosen to account for known changes in the detector response (in $|\eta|$) and to equalise statistics in each bin (in E_{T} and $p_\perp$). The final result is two scaled estimates of the number of events which should be left in the simulated sample after the cuts are applied, which can each be compared to the actual number left.

Table 7.3 shows the number of candidates over the full mass range (with $M_{ee} >$ 40 GeV/c^2) for each of the 36 electron pair classes, where just one of the two recon-

Table 7.3: Estimated number of events with two reconstructed electrons with $p_{\mathrm{T}} > 15$ GeV/c and $M_{ee} > 40$ GeV/c^2, where one passes the "loose" selection critera. The simulated sample corresponds to approximately 0.1 pb^{-1}. Figures are obtained by both applying cuts directly (black) and by scaling preselected events. The scaling factors are binned in the electron E_{T} and either the event $p_{\perp}$ (blue) or the cluster pseudorapidity (red). Electron candidates are ordered in the reconstructed p_{T}, as shown.

$p_{\mathrm{T}}^{\mathrm{e1}} \geq p_{\mathrm{T}}^{\mathrm{e2}}$			Electron candidate 2					
			Electrons			Non-electrons		
			Isolated	Unisolated	Background	Hadron	Muon	Unknown
Electron candidate 1	Electrons	Isolated	35 ± 6	1.0 ± 1.0	0	15 ± 4	0	3.0 ± 1.7
			35 ± 6	1.0 ± 1.0	0	14.8 ± 3.8	0	3.0 ± 1.7
			35 ± 6	1.0 ± 1.0	0	15 ± 4	0	3.0 ± 1.7
		Unisolated	0	6.0 ± 2.5	24 ± 5	168 ± 13	1.0 ± 1.0	22 ± 5
			0	5.4 ± 1.9	24 ± 4	181 ± 9	1.0 ± 0.7	21 ± 3
			0	6.1 ± 2.2	31 ± 5	228 ± 11	1.1 ± 0.8	26 ± 4
		Background	1.0 ± 1.0	18 ± 4	226 ± 15	1547 ± 40	6.0 ± 2.5	195 ± 14
			1.0 ± 1.0	16.7 ± 3.0	232 ± 11	1602 ± 24	4.4 ± 1.2	200 ± 10
			1.0 ± 1.0	22 ± 4	313 ± 14	2436 ± 35	7.0 ± 1.9	282 ± 13
	Non-electrons	Hadron	5.0 ± 2.2	154 ± 12	1278 ± 36	7357 ± 86	17 ± 4	1187 ± 35
			4.9 ± 2.2	175 ± 9	1282 ± 20	7830 ± 40	24.2 ± 2.3	1239 ± 19
			5.0 ± 2.2	232 ± 12	2154 ± 32	14480 ± 60	47 ± 4	2220 ± 30
		Muon	0	0	1.0 ± 1.0	13 ± 4	0	3.0 ± 1.7
			0	0.6 ± 0.6	2.6 ± 0.9	15.6 ± 2.1	0.6 ± 0.4	3.8 ± 1.1
			0	0.8 ± 0.8	5.7 ± 1.9	28.3 ± 3.1	0.6 ± 0.5	7.0 ± 1.9
		Unknown	1.0 ± 1.0	19 ± 4	145 ± 12	1110 ± 30	4.0 ± 2.0	159 ± 13
			0.9 ± 0.9	19 ± 3	149 ± 8	1184 ± 20	3.8 ± 1.3	164.5 ± 8.5
			1.0 ± 1.0	24 ± 4	216 ± 11	1926 ± 29	5.4 ± 1.7	251.5 ± 12.0

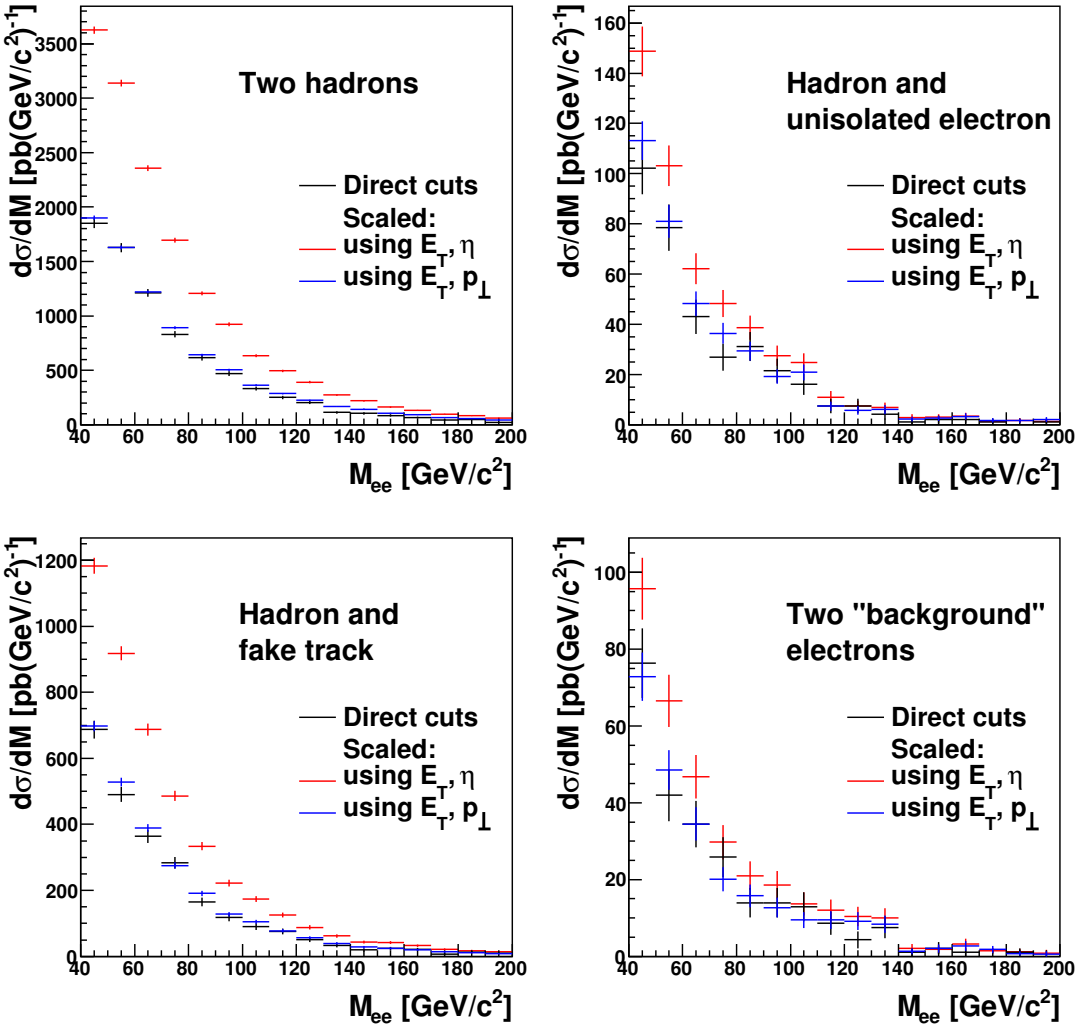

Figure 7.5: Estimated M_{ee} spectra from different background sources, for validation of the scaling method described in the text. Events have two reconstructed electrons with $p_{\mathrm{T}} > 15$ GeV/c, one of which passes the "loose" selection critera. The simulated sample corresponds to approximately 0.1 pb^{-1}. Figures are obtained by both applying cuts directly (black) and by scaling preselected events. The scaling factors are binned in the electron E_{T} and either the event $p_{\perp}$ (blue) or the cluster pseudorapidity (red). Top left: Both electrons are really hadrons. Top right: One hadron, one unisolated electron. Bottom left: One hadron, one fake track. Bottom right: Two "background" electrons.

structed electrons is required to pass the loose electron selection cuts. The M_{ee} spectra for some selected categories have also been plotted in Figure 7.5. As the offline selection in this case is only applied to one of the electrons, the weights are calculated using an equation equivalent to Equation 7.4.

It is interesting to compare Table 7.3 with the candidate numbers before selection in Table 7.2, as each category in general has a different average electron pair efficiency. In principle, those categories with the lowest efficiencies test the scaling method more thoroughly. Note especially the case where both "electrons" are really hadrons, with $\epsilon \sim 0.1$. In these cases, using $|\eta|$ as a binning variable for the efficiency leads to an overestimate of the background by as much as a factor of 2. The results using the event $p_\perp$ are much more accurate in general, and correctly predict the shapes and normalisations of the M_{ee} spectra in Figure 7.5. The agreement is typically within 6% when the statistical uncertainties allow a sensible comparison of the numbers. In addition, the statistical gain of weighting compared to cutting events can be seen even with this very loose selection, where the uncertainty on the directly cut events is up to a factor two worse than in the scaled events, depending on ϵ.

The same behaviour is observed when the cuts are tightened, requiring both electron candidates to pass the loose electron selection cuts. This directly tests the application of Equation 7.3 to the offline electron selection. Results are shown in Table 7.4 and Figure 7.6. The number of events after weighting, using efficiencies binned in the event $p_\perp$, generally agree well with the numbers found by directly applying the cuts, although there are some significant discrepancies of up to 30% in some categories. As before, using efficiencies binned in $|\eta|$ leads to background estimates which are in general significantly higher than the actual background found by applying cuts directly. In particular, the important hadron-hadron background is overestimated by more than a factor of 3.

A likely reason for the discrepancy observed when efficiencies are binned in E_{T} and $|\eta|$ is the implicit integration over $p_\perp$. In Figure 7.3, the electrons identification efficiency for the medium electron selection was shown to have a strong dependence on $p_\perp$, and a similar variation is observed for the loose electron selection. Furthermore,

Table 7.4: Estimated number of events with two reconstructed electrons with $p_{\mathrm{T}} > 15$ GeV/c and $M_{ee} > 40$ GeV/c^2, where both pass the "loose" selection critera. The simulated sample corresponds to approximately 0.1 pb^{-1}. Figures are obtained by both applying cuts directly (black) and by scaling preselected events. The scaling factors are binned in the electron E_{T} and either the event $p_{\perp}$ (blue) or the cluster pseudorapidity (red). Electron candidates are ordered in the reconstructed p_{T}, as shown.

$p_{\mathrm{T}}^{\mathrm{e1}} \geq p_{\mathrm{T}}^{\mathrm{e2}}$			Electron candidate 2					
			Electrons			Non-electrons		
			Isolated	Unisolated	Background	Hadron	Muon	Unknown
Electron candidate 1	Electrons	Isolated	35 ± 6 33 ± 6 35 ± 6	0 0.6 ± 0.6 0.5 ± 0.5	0 0 0	1.0 ± 1.0 3.0 ± 0.8 2.0 ± 0.6	0 0 0	2.0 ± 1.4 1.1 ± 0.7 0.7 ± 0.5
		Unisolated	0 0 0	4 ± 2 1.6 ± 0.6 2.1 ± 0.87	6.0 ± 2.5 4.5 ± 0.8 7.8 ± 1.3	12 ± 3 12.6 ± 0.8 24.7 ± 1.5	0 0.11 ± 0.08 0.18 ± 0.13	5.0 ± 2.2 3.8 ± 0.8 6.2 ± 1.1
		Background	1.0 ± 1.0 0.5 ± 0.5 0.4 ± 0.4	4.0 ± 2.0 3.0 ± 0.68 6.0 ± 1.2	48 ± 7 40.6 ± 2.3 70.1 ± 3.5	84 ± 9 110.9 ± 2.1 268.2 ± 4.5	1.0 ± 1.0 0.35 ± 0.14 0.92 ± 0.28	27 ± 5 30.8 ± 1.8 59 ± 3
	Non-electrons	Hadron	0 1.0 ± 0.5 0.8 ± 0.4	13 ± 4 15.6 ± 1.0 24.9 ± 1.5	107 ± 10 100.8 ± 2.0 221 ± 4	308 ± 18 355.3 ± 2.3 1002 ± 5	0 1.26 ± 0.16 3.7 ± 0.4	92.0 ± 9.6 91.3 ± 1.8 222.8 ± 3.7
		Muon	0 0 0	0 0.10 ± 0.11 0.22 ± 0.22	0 0.22 ± 0.10 1.2 ± 0.5	2.0 ± 1.4 0.90 ± 0.16 2.3 ± 0.3	0 0.02 ± 0.01 0.05 ± 0.06	0 0.35 ± 0.14 0.9 ± 0.3
		Unknown	1.0 ± 1.0 0.3 ± 0.3 0.4 ± 0.4	4.0 ± 2.0 3.7 ± 0.7 6.3 ± 1.2	17 ± 4 24.0 ± 1.8 44.7 ± 2.6	62 ± 8 79.0 ± 1.8 202.0 ± 3.6	0 0.41 ± 0.16 0.80 ± 0.26	31 ± 6 23.8 ± 1.6 50.5 ± 2.6

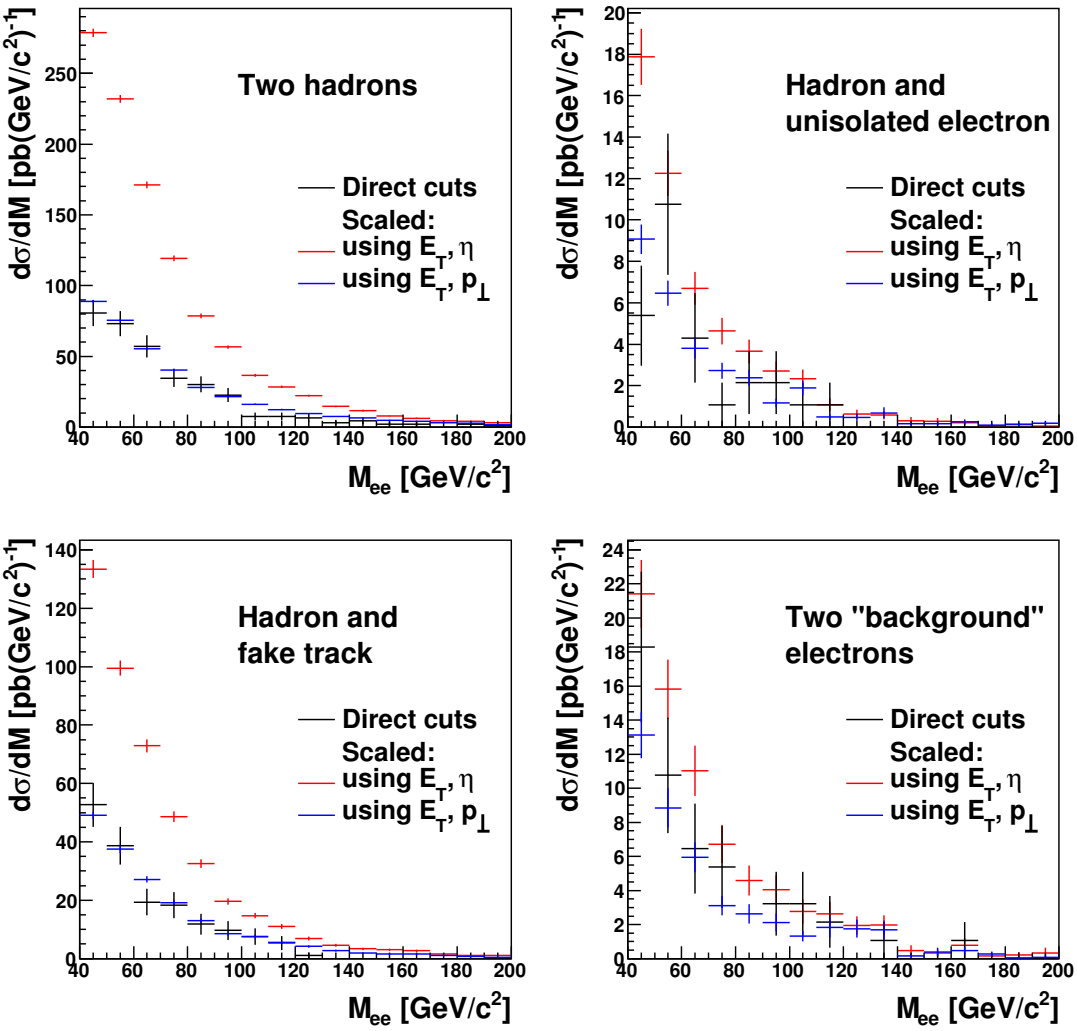

Figure 7.6: Estimated M_{ee} spectra from different background sources, for validation of the scaling method described in the text. Events have two reconstructed electrons with $p_{\mathrm{T}} > 15$ GeV/c, both passing the "loose" selection critera. The simulated sample corresponds to approximately 0.1 pb^{-1}. Figures are obtained by both applying cuts directly (black) and by scaling preselected events. The scaling factors are binned in the electron E_{T} and either the event $p_{\perp}$ (blue) or the cluster pseudorapidity (red). Top left: Both electrons are really hadrons. Top right: One hadron, one unisolated electron. Bottom left: One hadron, one fake track. Bottom right: Two "background" electrons.

Table 7.5: Event selection criteria used in final background estimations.

Selection #	Trigger	$p_{\mathrm{T}}^{\mathrm{cut}}$	Electron selection
1	e10_medium	15 GeV/c	Medium
2	e20_loose	25 GeV/c	Medium
3	e20_loose	25 GeV/c	Loose

Figure 7.2 showed that the events used for calculating the identification efficiencies (with at least 1 electron) are biased towards lower values of $p_{\perp}$ compared with $Z/\gamma^{*} \rightarrow e^{+}e^{-}$ candidate events (with at least 2 electrons). As electron identification efficiencies are generally higher in events with low $p_{\perp}$, this could explain why not accounting for the dependence on the event $p_{\perp}$ causes an overestimation of the background levels. This does not occur when efficiencies are binned in $p_{\perp}$.

This validation clearly demonstrates that a reliable background estimate requires that the electron identification efficiencies are binned in the event variable $p_{\perp}$, in addition to the binning in E_{T}. It is this set of efficiencies which will be used in the next section. Upon adding all background components together (excluding those involving isolated electrons), it is found that the scaled estimate in Table 7.3 is 5% higher than the actual background found by cutting events, while in Table 7.4 the scaled background estimate is 7.8% too high. As the selection tightens and the scaling factors decrease, any bias in the event scaling is expected to increase, and thus a more conservative systematic uncertainty of 10% is assumed to apply to events scaled in this manner. This is considerably smaller than other uncertainties, such as the jet cross section, which are relevant for the total background estimation. These will be considered further in Section 9.2.7. The event scaling itself thus contributes only a marginal amount to the total systematic uncertainty.

7.4 Results

In the previous section, unrealistically loose event selection criteria were used in order to test the accuracy of the background scaling method. In a real analysis, the three principal cuts considered (p_{T}, trigger and offline electron identification selections) are all important, and must all be applied. Table 7.5 lists the three combinations of cuts

considered in this section, based principally on the available triggers which are anticipated for running at 10^{31} cm^{-2}s^{-1}. In all cases, the p_{T} cut is chosen to be 5 GeV/c above the trigger cut. This has the double effect of significantly reducing the background as well as avoiding trigger turn-on effects. In addition to the cuts listed, the raw di-electron candidates are required to have $40 < M_{ee} < 200$ GeV/c^2. It would also normally be required that the reconstructed electrons have opposite charges. This has not been applied at the preselection stage (although it could be), in order to boost the number of events in certain background categories, especially those involving unisolated electrons. Instead, the event weights have all been divided by two, assuming a charge-symmetric background.

The mass spectra of the major sources of background in these three cases are shown in Figure 7.7, together with the summed total after applying a smoothing procedure described below. All of the histograms are normalised to 200 pb^{-1} of luminosity, and the predicted background levels are compared to the expected $Z/\gamma^* \rightarrow e^+e^-$ signal obtained using a dedicated simulation of this process. Note that backgrounds involving genuine isolated electrons have been explicitly excluded from this particular background estimate, *ie* W and t production, as well as $Z/\gamma^* \rightarrow \tau^+\tau^-$.

The results presented here are a clear statistical improvement over Figure 7.1. In the top two rows of Figure 7.7, the "medium" offline electron selection cuts have been used, and the background has a similar composition despite the different p_{T} cuts applied. Just under half of the overall background is due to two misidentified hadrons, while most of the remainder involves unisolated electrons from J/ψ, B or D meson decays (either two unisolated electrons or one hadron and one unisolated electron). There is also an important contribution from the so-called "background" electrons (conversions *etc*) in combination with a misidentified hadron. The higher E_{T} threshold for selection 2, shown in the middle row, serves to drastically reduce the background levels by almost an order of magnitude, in addition to changing the shape of the background in the first few M_{ee} bins. The lowest row of Figure 7.7 shows the prediction for Selection 3. The background in this case is significantly increased compared to selection 2, due to the loosening of the electron selection cuts. Events with two misidentified hadrons still

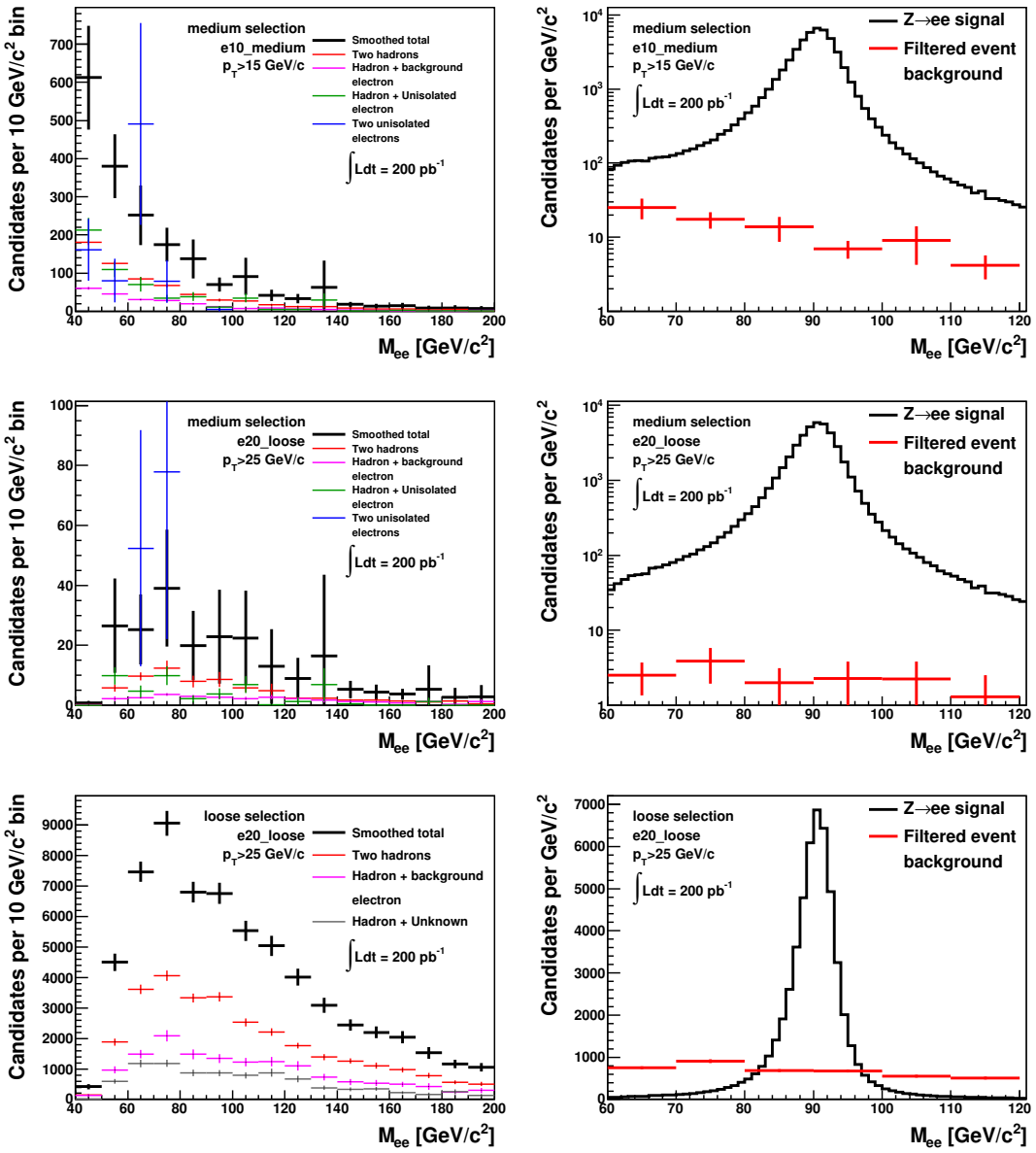

Figure 7.7: Estimated background levels for different selection scenarios. Top: e10_medium trigger, $p_{\mathrm{T}}^{\mathrm{e}} > 15$ GeV/c and medium offline electron selection. Middle: e20_loose trigger, $p_{\mathrm{T}}^{\mathrm{e}} > 25$ GeV/c and medium offline electron selection. Bottom: e20_loose trigger, $p_{\mathrm{T}}^{\mathrm{e}} > 25$ GeV/c and loose offline electron selection. The major individual background components are shown on the left, normalised to 200 pb^{-1}, along with the total after smoothing. On the right, this total is compared to the expected $Z/\gamma^* \to e^+e^-$ signal for the same luminosity. The uncertainties shown are statistical only.

account for approximately half of the total, events with a single misidentified hadron combined with background electron or "Unknown" candidates being the other major contributors. The contribution from unisolated electrons is negligible in this case, due to their smaller production cross section.

In the top two rows of Figure 7.7, the statistical fluctuations in the histograms involving unisolated electrons are significant. This arises primarily from the low number of preselected electron pairs, *cf* Table 7.2. However, the relatively high selection efficiency of unisolated electrons means that they can still form a significant part of the background after selection. Ideally, events involving the decays of b and c quarks to electrons should be simulated separately, but there is no such simulation available at the present time. Thus, there are just 10 preselected events with two unisolated electrons, so the statistical uncertainty on that particular contribution can never be better than approximately $1/\sqrt{10} \approx 32\%$. Additionally, the few available electron pairs only populate the low mass bins, therefore their background contribution directly underneath the Z/γ^* mass peak is potentially underestimated.

To smooth out the low-statistics background components, the following procedure has been adopted. Instead of simply adding contributions from all 25 components in each mass bin, only those with more than 50 initial candidates (over the full mass range) have been added in initially. This fixes the shape of the background. All components with fewer initial pairs are assumed to follow the same distribution, and only contribute to the normalisation of the total background. This is done by scaling the previously obtained background shape to account for all components. The uncertainty in each bin is also scaled to account for the resulting uncertainty in the normalisation. This is most clearly seen with selection 2, where just two events with two unisolated electrons pass the preselection. When scaled with the appropriate efficiencies, they account for almost 30% of the total background. After scaling, all bins in the black histogram are 30% higher than they would otherwise have been, with correspondingly increased errors.

Using this procedure, the background can be estimated within specific mass bins, including all sources of background (except those involving isolated electrons). The estimated backgrounds are listed in Table 7.6 for three possible mass ranges, and these

Table 7.6: Top: Estimated number of background events for the three selections of Table 7.5 in different mass ranges. These numbers are obtained after application of the scaling and smoothing procedures described in the text. Bottom: Estimated background contributions relative to the signal from $Z/\gamma^* \to e^+e^-$ events in different mass ranges, for the same selections. Numbers are calculated for 200 pb^{-1} of 10 TeV collision data. The displayed uncertainties are statistical only.

Background events from filtered sample			
Mass range	$60 - 120$ GeV/c^2	$70 - 110$ GeV/c^2	$80 - 100$ GeV/c^2
Selection 1	767 ± 116	473 ± 85	207 ± 54
Selection 2	142 ± 36	104 ± 31	42 ± 19
Selection 3	$(40.7 \pm 0.9) \times 10^3$	$(28.1 \pm 0.7) \times 10^3$	$(13.6 \pm 0.5) \times 10^3$
Background fraction for filtered events			
Mass range	$40 - 200$ GeV/c^2	$70 - 110$ GeV/c^2	$80 - 100$ GeV/c^2
Selection 1	$(14.4 \pm 2.2) \times 10^{-3}$	$(9.1 \pm 1.6) \times 10^{-3}$	$(4.3 \pm 1.1) \times 10^{-3}$
Selection 2	$(3.1 \pm 0.8) \times 10^{-3}$	$(2.3 \pm 0.7) \times 10^{-3}$	$(1.0 \pm 0.5) \times 10^{-3}$
Selection 3	0.74 ± 0.02	0.52 ± 0.01	0.27 ± 0.01

are compared to the expected signal from $Z/\gamma^* \to e^+e^-$ events in the same ranges. In general, with the medium offline electron selection, background levels from the filtered event sample should be of the order 1% or less. It is clear that Selection 3 will not give a good signal to background ratio, and so only the medium offline electron selection will be considered further in Chapter 9.

Chapter 8

Trigger efficiency determination from data

The ATLAS trigger, described in Section 4.7, is a critical system for the success of the whole experiment. At design luminosity, over 99.99% of all events will be rejected by the trigger system, never to be recorded to disk. Therefore, if poorly configured or monitored, the system has the potential to overlook crucial physics events, reducing the potential for new discoveries. This chapter describes one aspect of trigger commissioning, that of measuring electron trigger efficiencies using $Z/\gamma^* \to e^+e^-$ events. The electron triggers themselves were described in Section 5.2.

A trigger's efficiency is one of its primary figures of merit, along with the event rate at different levels. Given the high particle density in a typical LHC bunch crossing, most triggers will have to offer a compromise between efficiency and rate, meaning that some signal events are necessarily lost due to cuts designed to ensure an acceptable background rate. Monitoring these efficiencies and understanding any nonuniformities will be vital for any physics studies using the triggered events. This is especially important in the "turn-on" region of each trigger, near its particular threshold.

The results presented in this chapter are necessarily derived from the ATLAS trigger simulation, but the techniques described will be used when collisions begin later in 2009. They will come into full use when the instantaneous luminosity increases. At $\mathcal{L} = 10^{33}$ cm^{-2}s^{-1}, the $Z/\gamma^* \to e^+e^-$ production rate is approximately 2 Hz in 14 TeV pp collisions. With an expected acceptance of roughly 40% and a reconstruction efficiency for each electron of 80%, this translates into a detected rate of approximately 0.5 Hz. If the trigger is 90% efficient with respect to the offline selection, the overall efficiency

could be measured to within a 1% statistical precision with about 30 minutes of data-taking, allowing run-by-run monitoring of the electron triggers. Over longer periods, the efficiency measurement could be binned in variables such as the electron p_{T} or pseudorapidity.

This chapter begins with an outline of the mathematical framework used to calculate electron trigger efficiencies from data, in Section 8.1. Details of the analysis procedure are presented in Section 8.2, including a short discussion on potential kinematic biases. Results are presented in Section 8.3, where global and differential electron trigger efficiencies obtained using the tag and probe method on simulated data are shown. Background removal techniques are discussed in Section 8.4, and the extension from single electron trigger efficiencies to event-level trigger efficiencies in $Z/\gamma^* \rightarrow e^+e^-$ events is considered in Section 8.5. The chapter concludes with two studies illustrating both the robustness of the tag and probe technique, and its potential use in refining the trigger selection. Whilst the focus of this work is on measuring electron trigger efficiencies, the offline identification efficiency can be measured in a very similar way. Where relevant, these measurements will be discussed together.

8.1 Mathematical framework

The so-called "tag and probe" method allows the reconstruction efficiency or trigger efficiency of a physics object to be estimated using real data, without relying on Monte Carlo simulations. This is important, as the detector simulation may not represent the detector correctly in early data-taking. The tag and probe method relies on having two objects available for selection, such as the two electrons in $Z/\gamma^* \rightarrow e^+e^-$ events. One of these acts as the *tag*, improving the purity of the sample, allowing the measurement of the other electron's efficiency (the *probe*). A typical set of cuts is given in Table 8.1, for one particular efficiency measurement.

Cuts on the tag electron and the event in general exist purely for the reduction of backgrounds, and can be made reasonably stringent if required. The tag electron is also responsible for triggering the event, so that it is recorded to disk. The selection cuts applied to the probe electron are divided into two parts. All probe electrons passing

Table 8.1: Example event selection criteria for a tag and probe trigger measurement. The cuts listed are for a measurement of the e10_medium trigger efficiency with respect to the medium offline electron selection. Terms are explained in the text.

Tag selection	$E_{\mathrm{T}} > 15$ GeV, $\lvert\eta\rvert < 2.5$, crack region excluded, tight offline selection, passes e10_medium cuts.
Probe preselection	$E_{\mathrm{T}} > 15$ GeV, $\lvert\eta\rvert < 2.5$, crack region excluded, medium offline selection.
Event selection	Two reconstructed electrons with oppositely charged tracks, $70 < M_{ee} < 100$ GeV/c^2.
Probe requirement	Probe passes e10_medium cuts.

the *probe preselection* enter into the denominator of the efficiency ratio, while only those additionally passing the *probe requirement* contribute to the numerator. Thus, the measured efficiency is that of the probe requirement, relative to that of the probe preselection. The cuts in Table 8.1 therefore define the e10_medium trigger efficiency for electrons which satisfy the medium offline selection cuts.

As the method presented here uses tag-probe pairs (rather than events) as the fundamental unit, it is possible for there to be more than one tag-probe pair in any given event. In a typical well-reconstructed $Z/\gamma^* \to e^+e^-$ event, each electron could be a tag in turn, with the other being the corresponding probe. To calculate the efficiency and its error correctly, it is necessary to keep track of different classes of events. It is sufficient to consider separately events where exactly one tag-probe pair exists and those where two such pairs exist. In the former case, the probe could pass ("1p" events) or fail ("1f") the probe requirement. In the latter case ("2p"), it will be assumed that the tag selection is at least as tight as the probe requirement, so that all probes in this category pass.

If N Z bosons decaying into electrons were produced in some specified time period, the actual number of events found in an analysis will be reduced by the detector acceptance $\mathcal{A}$, the electron reconstruction efficiency ϵ_{r} and the electron trigger efficiency ϵ_{t} (it is not necessary to consider the smearing correction $\mathcal{S}$ introduced in Section 3.2 at the present time). Note that ϵ_{r} and ϵ_{t} may be different for the tag and probe electrons. In addition, background events will occasionally be reconstructed as signal, giving a contribution of N_{bkg} to the total number of detected events. These numbers may apply to the whole detector (to calculate an averaged "global" efficiency) or to a particular

bin in a differential efficiency measurement. In this section, a global measurement is assumed, with the extension to binned measurements discussed in Section 8.1.1.

Given the above definitions, the numbers of events in each category are given by the following expressions:

$$\begin{aligned} N_{1\mathrm{f}} &= N\mathcal{A} \cdot 2\epsilon_{\mathrm{r,tag}}\epsilon_{\mathrm{r,probe}}\epsilon_{\mathrm{t,tag}}(1-\epsilon_{\mathrm{t,probe}}) + N_{\mathrm{bkg,1f}}, \\ N_{1\mathrm{p}} &= N\mathcal{A} \cdot 2\epsilon_{\mathrm{r,tag}}\epsilon_{\mathrm{t,tag}}(\epsilon_{\mathrm{r,probe}}\epsilon_{\mathrm{t,probe}} - \epsilon_{\mathrm{r,tag}}\epsilon_{\mathrm{t,tag}}) + N_{\mathrm{bkg,1p}}, \\ N_{2\mathrm{p}} &= N\mathcal{A} \cdot \epsilon^2_{\mathrm{r,tag}}\epsilon^2_{\mathrm{t,tag}} + N_{\mathrm{bkg,2p}}. \end{aligned} \tag{8.1}$$

It is assumed in these expressions that each efficiency is sufficiently uniform as a function of the implicitly integrated variables ($p^{\mathrm{e}}_{\mathrm{T}}$, $|\eta^e|$, *etc*), such that each electron falling within that region has the same probability of passing the relevant selection criteria. It may be that the efficiencies vary significantly as a function of one or more variables (*eg* in the turn-on region near the trigger's p_{T} threshold). If this is the case, the efficiencies in Equation 8.1 necessarily refer to some appropriately weighted average efficiency. In Section 8.2.2 this is discussed as a potential source of bias.

Defining $N_{1\mathrm{f}}{}'$ to be equal to $N_{1\mathrm{f}} - N_{\mathrm{bkg,1f}}$ and so on, the above equations can be rearranged to give an estimate of $\epsilon_{\mathrm{t,meas}}$, the single electron trigger efficiency for reconstructed electrons:

$$\epsilon_{\mathrm{t,meas}} = \frac{N'_{1\mathrm{p}} + 2N'_{2\mathrm{p}}}{N'_{1\mathrm{f}} + N'_{1\mathrm{p}} + 2N'_{2\mathrm{p}}}. \tag{8.2}$$

The variables used so far have been chosen such that they are statistically independent, simplifying the calculation of the statistical uncertainty of $\epsilon_{\mathrm{t,meas}}$.[16] Writing $N'_{1\mathrm{f}} + N'_{1\mathrm{p}} + N'_{2\mathrm{p}}$ as $N_{\mathrm{T}}{}'$, and $N'_{1\mathrm{p}} + N'_{2\mathrm{p}}$ as $N_{\mathrm{p}}{}'$, we have

$$\begin{aligned} \langle \delta\epsilon_{\mathrm{t}}{}^2 \rangle &= \sum_{N'_{\mathrm{i}}} \left[\frac{\partial\epsilon}{\partial N'_{\mathrm{i}}}\right]^2 \langle \delta N'^2_{\mathrm{i}} \rangle \\ &= \left[\frac{-\epsilon_{\mathrm{t}}}{N'_{\mathrm{T}}}\right]^2 \langle \delta N'_{1\mathrm{f}}{}^2 \rangle + \left[\frac{1-\epsilon_{\mathrm{t}}}{N'_{\mathrm{T}}}\right]^2 \langle \delta N'_{1\mathrm{p}}{}^2 \rangle \\ &\quad + \left[\frac{2(1-\epsilon_{\mathrm{t}})}{N'_{\mathrm{T}}}\right]^2 \langle \delta N'_{2\mathrm{p}}{}^2 \rangle \\ &= \frac{1}{N'_{\mathrm{T}}{}^2}\left[(1-2\epsilon_{\mathrm{t}})\langle \delta N'^2_{\mathrm{p}} \rangle + \epsilon^2_{\mathrm{t}}\langle \delta N'_{\mathrm{T}}{}^2 \rangle + 2(1-\epsilon_{\mathrm{t}})^2 \langle \delta N'_{2\mathrm{p}}{}^2 \rangle\right]. \end{aligned} \tag{8.3}$$

[16] For brevity, $\epsilon_{\mathrm{t,meas}}$ will be referred to simply as ϵ_{t} from now on.

In the background-free case, this can be simplified still further as $\langle \delta {N_{\mathrm{i}}}^2 \rangle = N_{\mathrm{i}}$, giving (unprimed quantities are now used, indicating the absence of background)

$$\begin{aligned} \langle \delta {\epsilon_{\mathrm{t}}}^2 \rangle &= \frac{1}{N_{\mathrm{T}}^2} \left[(1-2\epsilon_{\mathrm{t}}) N_{\mathrm{p}} + \epsilon_{\mathrm{t}}^2 N_{\mathrm{T}} + 2(1-\epsilon_{\mathrm{t}})^2 N_{2\mathrm{p}} \right] \\ &= \frac{\epsilon_{\mathrm{t}}(1-\epsilon_{\mathrm{t}})}{N_{\mathrm{T}}} \cdot \left[1 + \frac{(1-\epsilon_{\mathrm{t}})}{\epsilon_{\mathrm{t}}} \frac{2N_{2\mathrm{p}}}{N_{\mathrm{T}}} \right]. \end{aligned} \tag{8.4}$$

The first factor in Equation 8.4 can be recognised as a conventional binomial uncertainty, as used for example in Equation 7.1. The second factor corrects the uncertainty to account for events with two tag-probe pairs, and always increases the statistical uncertainty because the "2p" events get counted twice when calculating ϵ_{t}, but do not have double the statistical significance of the other events.

The difference between Equation 8.4 and the standard binomial uncertainty is generally small. The second term in Equation 8.4 is largest when $N_{1\mathrm{p}} = 0$, *ie* $\epsilon_{\mathrm{t}} = 2N_{2\mathrm{p}}/N_{\mathrm{T}}$. In this case, the expression in Equation 8.4 gives an uncertainty $\Delta\epsilon_{\mathrm{t}} = \sqrt{\langle \delta {\epsilon_{\mathrm{t}}}^2 \rangle}$ that is up to 40% larger than the simpler binomial efficiency if ϵ_{t} is very small, but this difference decreases rapidly as ϵ_{t} increases. For example, for $\epsilon_{\mathrm{t}} = 90\%$, the binomial uncertainty differs from Equation 8.4 by just 5%.

8.1.1 Differential detector efficiency

The equations in the previous section provide average efficiency numbers, but it is also desirable to be able to determine efficiencies binned in some variable, either of the individual leptons (*eg* p_{T}^{ℓ}) or of the event (*eg* $p_{\mathrm{T}}^{\mathrm{Z}}$). The equations derived in Section 8.1 can be used for this purpose, after appropriate reinterpretation of the terms. In principle, decomposition of the trigger efficiency can be performed in as many dimensions as required, limited only by the statistical precision of each result.

The simplest case is where an event-level variable is used. In this case, analysis proceeds as in Section 8.1, except that only events within a given bin are used in that bin's calculation. Therefore, this kind of "differential" binned efficiency is just a series of independent global efficiency measurements.

In the case of an efficiency binned in an electron variable (say, the probe electron p_{T}), each bin can again be regarded as a separate efficiency measurement, one where the relevant electron is constrained to lie within that bin. It is not necessary to kine-

matically restrict the other electron. In this case, $N'_{2\mathrm{p}}$ in Equation 8.2 effectively counts only those events where *both* electrons fall into that particular bin. If one electron falls outside, it cannot be considered a probe for this measurement, so the tag-probe pair is of the "1f" or "1p" type. With these definitions, the calculation of ϵ_{t} is unchanged.

Note that for the majority of this chapter, the variables used to describe binned efficiencies will be those of the offline reconstructed electrons. The variables measured by the trigger cannot be used as they may not be available if the electron fails to trigger. Due to the finite detector resolution, bin migrations may occur, and it will be assumed that in a physics analysis that uses tag and probe results, these effects will be accounted for separately.

8.2 Analysis procedure

All of the results presented in this chapter are derived from the simulated datasets with $\sqrt{s} = 14$ TeV listed in Table 3.1. The electron trigger menu is extensive, and documented in the trigger chapters of [42]. Results for just a few critical triggers will be presented here. These follow the naming convention introduced in Section 5.2, where for example e10_medium refers to a trigger with a medium electron selection applied at the Event Filter and a threshold of $p_{\mathrm{T}} > 10$ GeV/c.

All trigger efficiencies shown are measured relative to the corresponding offline electron selection. This follows the pattern used in [42], where the complete studies of the tag and probe method were presented. The measurements were made in three stages, referring to electron reconstruction (*ie* cluster formation and track association), identification (*ie* the loose, medium and tight offline selections) and finally triggering. The results presented here constitute this third step: the measurement of the probability that an offline identified electron passes a given trigger chain. This set of definitions is consistent in the sense that the total electron identification and trigger efficiency is the product of the three separate measurements.

As in [42], the efficiencies of specific trigger levels will be examined, in addition to the efficiency of all trigger levels combined. These efficiencies are shown relative to the preceeding trigger level unless otherwise stated. For example, the efficiency of Level 2

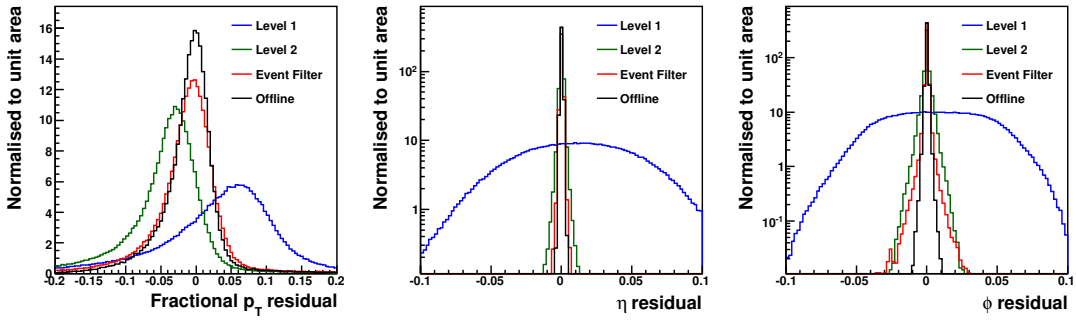

Figure 8.1: Residuals of the trigger and offline electron variables with respect to the corresponding true values. The quantities plotted are $(p_{\mathrm{T}}^{\mathrm{reco}} - p_{\mathrm{T}}^{\mathrm{true}})/p_{\mathrm{T}}^{\mathrm{true}}$ (left), $(\eta^{\mathrm{reco}} - \eta^{\mathrm{true}})$ (middle) and $(\phi^{\mathrm{reco}} - \phi^{\mathrm{true}})$ (right).

is measured only for electrons which pass the preceeding Level 1 item in addition to the offline selection.

Most of the triggers examined in this chapter, such as e10_medium, are designed for low luminosity running and hence have relatively loose cuts. A more restrictive trigger, e22i, has also been studied. This is a proposed trigger for mid luminosity running ($\mathcal{L} = 10^{33}$ cm^{-2}s^{-1}), and will be optimised using low luminosity data. Unlike the other triggers examined here, the e22i trigger does not have a (loose, medium, tight) suffix in its name, because its EF selection does not correspond closely to any of the offline electron selections.

8.2.1 Trigger object association

With the software available at the time of these studies, access to the event-level trigger decision and the trigger RoIs was possible, but the trigger decision associated with a specific RoI was not (this is now possible in more recent versions of the ATLAS software). Therefore, it was necessary to re-calculate the trigger selection at each level, based on the RoI information. This re-calculation was cross-checked against the event-level decision for consistency. Figure 8.1 illustrates the reconstruction performance of each trigger level as well as that of the offline reconstruction. The residuals with respect to the true value of the electron p_{T}, η and ϕ are shown. The much reduced resolution at Level 1 is caused by the relatively coarse measurement granularity, where the E_{T} of an RoI is measured in integral multiples of 1 GeV, and η and ϕ are each measured with a granularity of approximately 0.1. Level 2 performs better, already

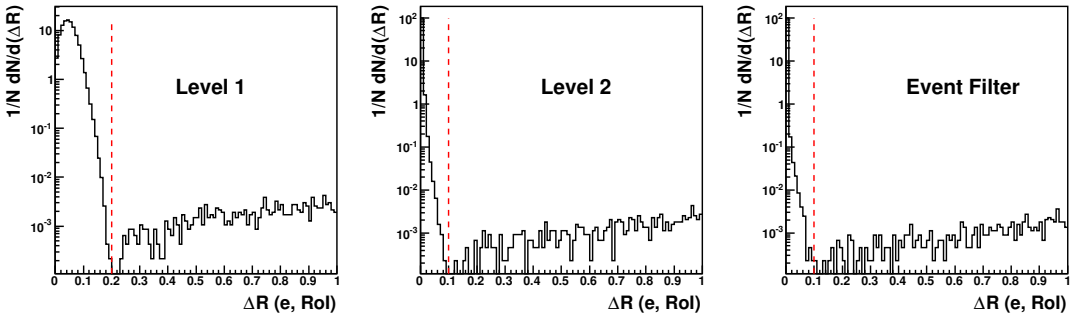

Figure 8.2: ΔR separation between reconstructed electrons and electron trigger RoIs. The vertical lines show the applied cuts for trigger association.

approaching the quality of the offline reconstruction. There is, however, a 3% bias on the p_{T} measurement at this level, but the resolution is small, approximately 2.7%. The Event Filter performance is very close to the offline performance, with only a slightly worse p_{T} resolution (2.4% as compared to 1.9% for offline) and larger tails in the bending direction ϕ.

Trigger RoIs passing the relevant selection were associated with reconstructed electron candidates based on their proximity in the $\eta - \phi$ plane, $\Delta R = \sqrt{\Delta\eta^2 + \Delta\phi^2}$. Distributions of ΔR at each trigger level are shown in Figure 8.2. Each distribution shows a sharp peak near $\Delta R = 0$ associated with correctly matched RoIs, with a somewhat worse resolution at Level 1. If a reconstructed electron is not directly associated with an RoI, the nearest RoI may be from another source, explaining the small number of entries at larger ΔR values. The association cuts used were $\Delta R < 0.2$ at Level 1 and $\Delta R < 0.1$ for the HLT.

8.2.2 Truth-level comparisons

When testing the methods presented in this chapter on simulated data, a crucial test is the comparison with efficiencies derived using the generator-level truth information. Truth-level electrons, coming from the Z decay, are matched to reconstructed electrons by requiring a separation ΔR of less than 0.1. If a true electron is reconstructed, identification and trigger criteria can be applied exactly as in the tag and probe analysis. This allows binned efficiencies to be plotted as a function of the reconstructed variable, as is done for the tag and probe efficiencies.

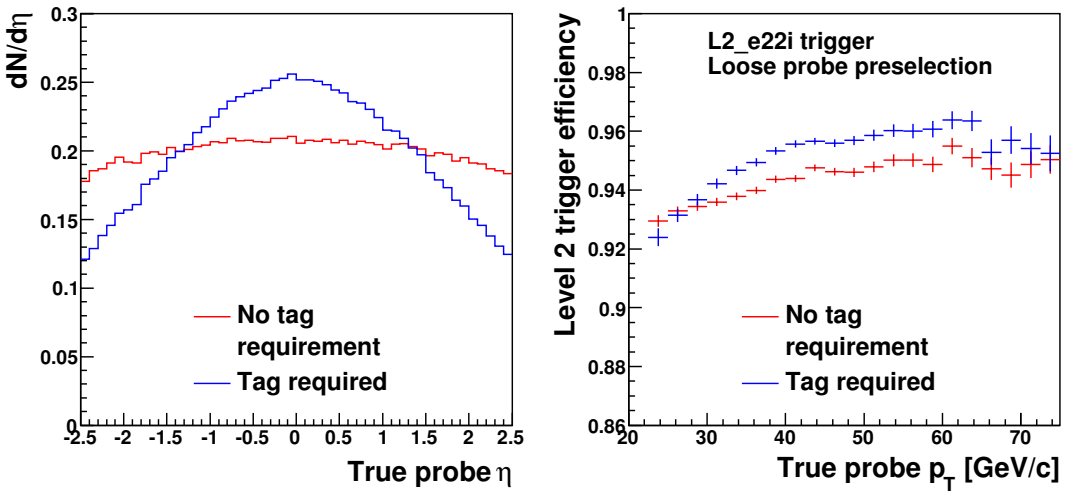

Figure 8.3: Left: Normalised pseudorapidity distributions of probe electrons with and without a tag requirement. Right: Truth-level efficiency for the L2 part of the e22i trigger as a function of the electron p_{T}. Only reconstructed probe electrons passing Level 1 were considered, but no offline electron identification criteria were applied beyond this.

Kinematic bias arising from the tag electron

In a tag and probe analysis, reconstructing the tag electron is mandatory. In general this means that the tag electron's kinematics must satisfy $|\eta| < 2.5$ and a p_{T} cut as well. As the kinematics of the two electrons from the Z decay are correlated, this changes the kinematic distributions of the probe electron, as illustrated in the left panel of Figure 8.3, where it can be seen that requiring a tag electron biases the probe distribution towards central rapidities. The right panel of Figure 8.3 shows the potential effect of this on a truth-level efficiency measurement as a function of p_{T}. The trigger illustrated (L2_e22i) has been deliberately chosen because its efficiency varied strongly as a function of $|\eta|$ due to a problem with the reconstruction which has now been fixed (this version of the trigger reconstruction software is also used in Section 8.6.2). Thus, when a tag is required, a tag and probe measurement of this trigger is biased towards regions of higher efficiency. To allow a direct comparison to the true efficiencies, all true efficiencies compared with tag and probe results in this chapter have been constructed requiring the presence of a tag electron satisfying kinematic cuts equivalent to those used in the tag and probe analysis.

This confirms that efficiencies obtained with the tag and probe method are only

strictly applicable to electrons with a kinematic distribution similar to that of the probes in the measurement. To avoid bias if the distributions are different, it will be necessary to bin the efficiencies in more than one dimension, for example in the electron p_{T} and $|\eta|$ simultaneously. The issue of potential bias will become less important as data accumulates and the bins over which the efficiency is measured get smaller, and hence the efficiency variation within the bins decreases.

8.3 Results

Trigger efficiencies have been measured with the tag and probe method for the triggers e10_loose, e10_medium, e15_medium, e20_loose and e22i. The first four triggers are designed for early running at an instantaneous luminosity of 10^{31} cm^{-2}s^{-1}. The e10_loose trigger is part of the double object trigger 2e10_loose, while e10_medium has tight enough selection criteria to be used as a single object trigger. In studying the e10_loose trigger using the tag and probe technique, the tag is required to pass the single object e10_medium trigger. The e15_medium trigger is a backup trigger for e10_medium, and it may also be used for running at $\mathcal{L} = 10^{32}$ cm^{-2}s^{-1}. The e20_loose trigger is the lowest threshold single electron trigger with a loose EF selection planned for running at $\mathcal{L} = 10^{31}$ cm^{-2}s^{-1}. Finally, the e22i trigger, introduced in Section 8.2, is proposed for running at an instantaneous luminosity of 10^{33} cm^{-2}s^{-1}. All efficiencies were determined on a signal-only simulation corresponding to 150 pb^{-1} of data. Backgrounds will be discussed further in Section 8.4.

Global tag and probe efficiencies for these five triggers, together with their statistical uncertainties and bias relative to the true efficiency, are shown in Table 8.2. As may be expected, the triggers which apply a medium electron selection at the Event Filter have a low efficiency with respect to the loose offline electron selection, but perform well when measured with respect to the medium or tight offline selections. The e22i trigger shows less variation with the offline electron selection because the EF selection of this trigger is not directly related to the loose, medium or tight offline selections.

Overall, the bias of the tag and probe results is small, less than 0.1% in most cases. The bias is generally greater when the measured efficiencies are further from 100%, and

Table 8.2: Table of single object trigger efficiencies from tag and probe analyses for various triggers, as described in the text, on a simulated sample of $Z/\gamma^* \to e^+e^-$ events equivalent to 150 pb^{-1} of data. Each efficiency is calculated with respect to a particular offline selection. The "Bias" column shows the discrepancy ($\epsilon_{\mathrm{t,meas}} - \epsilon_{\mathrm{t,true}}$) between the tag and probe compared to the truth-level result.

Trigger	Loose		Medium		Tight	
	ϵ	Bias	ϵ	Bias	ϵ	Bias
e10_loose	97.07(5)%	0.13%	98.56(4)%	0.09%	99.58(2)%	0.07%
e10_medium	86.74(10)%	0.36%	98.00(4)%	0.11%	99.14(3)%	0.08%
e15_medium	87.34(10)%	0.35%	98.13(4)%	0.08%	99.15(3)%	0.05%
e20_loose	96.98(5)%	0.04%	98.48(4)%	-0.02%	99.41(3)%	-0.02%
e22i	90.76(9)%	0.03%	93.83(8)%	-0.06%	94.91(8)%	-0.06%

could be due to remaining kinematic biases. As these depend on the specific trigger and offline selections used, they need to be estimated on a case-by-case basis. As noted in Section 8.2.2, differential distributions must be considered in order to avoid more serious biases when applying tag and probe efficiencies to other types of events. A selection of binned differential efficiencies are now presented. As an illustration of the expected precision achievable with very early data, differential results for $\mathcal{L} = 10^{31}$ cm^{-2}s^{-1} triggers have been shown for a reduced dataset, equivalent to 50 pb^{-1}, except for Figure 8.7.

Figure 8.4 shows the efficiency of the e10_loose trigger measured for electrons passing the tight offline selection cuts, as a function of the reconstructed electron p_{T} and η. The efficiency of this trigger is extremely high, well over 99% over most of the kinematic range considered. This is partly because of the very loose selection applied (*ie* no L1 isolation and loose cuts at the EF), but mainly because the efficiency is shown for electrons which have already passed the tight offline electron identification cuts. Nevertheless, it clearly shows the turn-on at the p_{T} threshold for each trigger level, which is lower for Level 1. It can also be seen that the Level 2 trigger loses approximately 5% of electrons which are reconstructed in the calorimeter crack region around $|\eta| = 1.4$. Away from the turn-on region, the tag and probe and true efficiencies agree to within 0.5% or better.

The efficiency of the e10_medium trigger for electrons passing the medium offine

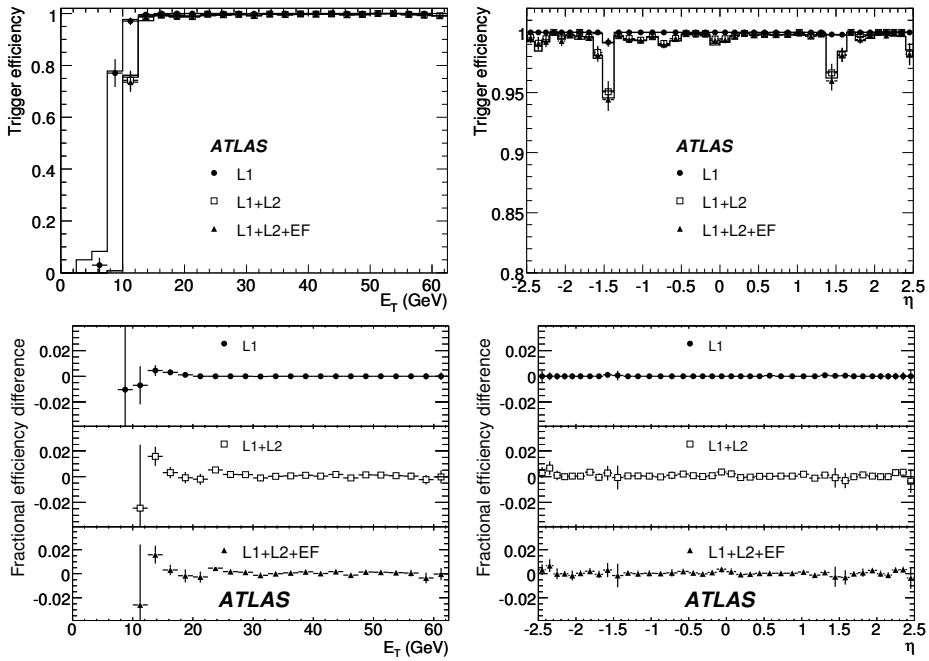

Figure 8.4: Efficiency of the e10_loose trigger with respect to the "tight" electron selection. Tag and probe results (corresponding to 50 pb^{-1} luminosity) are shown by the points, the corresponding true efficiency by lines. The lower plots show the fractional efficiency difference between the two.

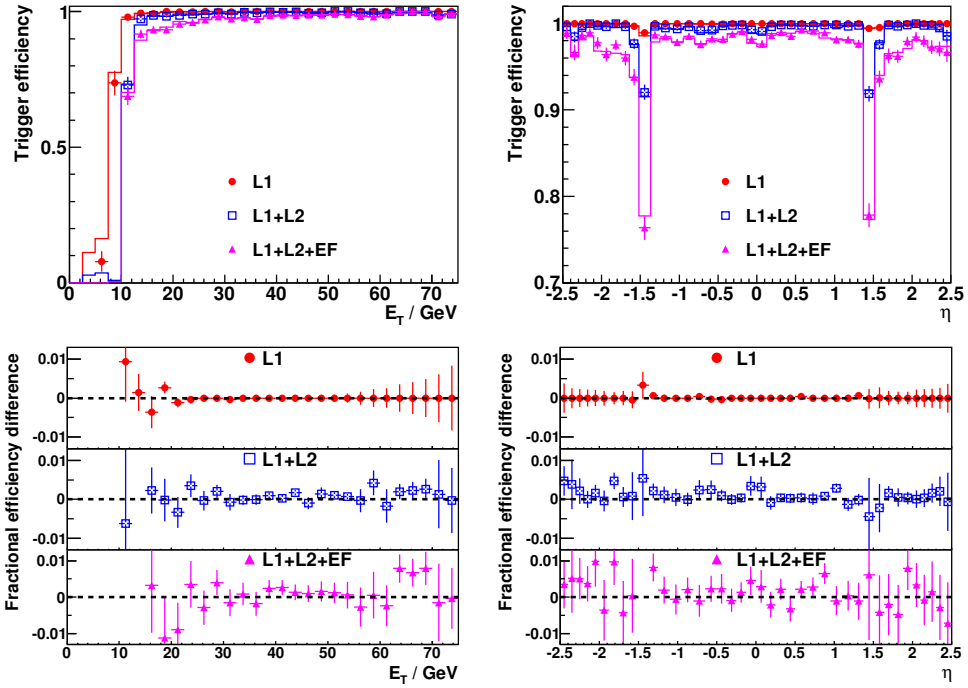

Figure 8.5: Efficiency of the e10_medium trigger with respect to the "medium" electron selection. Tag and probe results (corresponding to 50 pb^{-1} luminosity) are shown by the points, the corresponding true efficiency by lines. The lower plots show the fractional efficiency difference between the two.

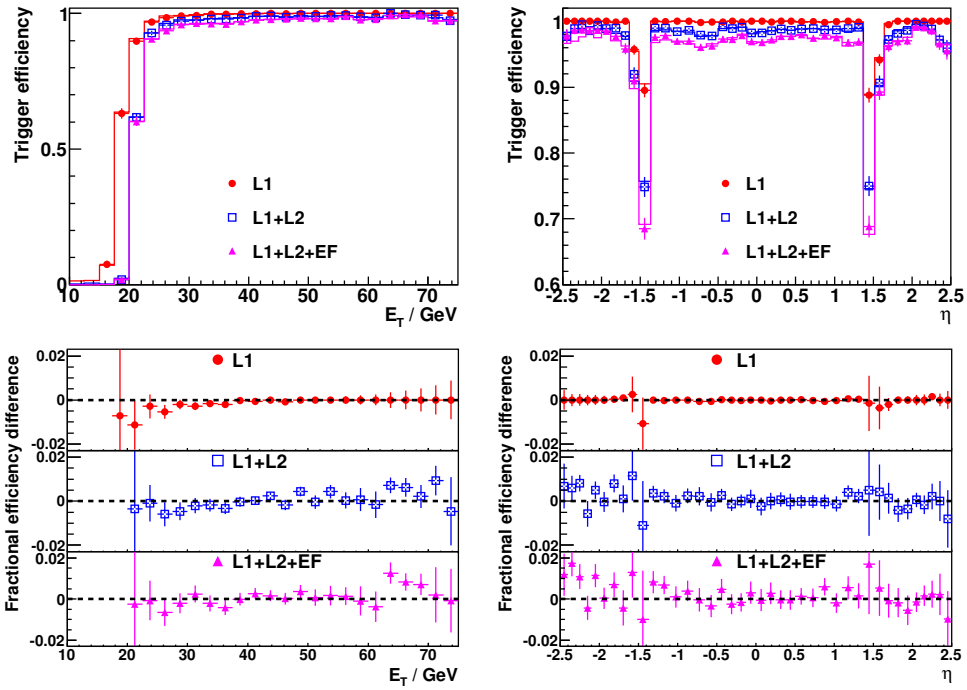

Figure 8.6: Efficiency of the e20_loose trigger with respect to the "loose" electron selection. Tag and probe results (corresponding to 50 pb^{-1} luminosity) are shown by the points, the corresponding true efficiency by lines. The lower plots show the fractional efficiency difference between the two.

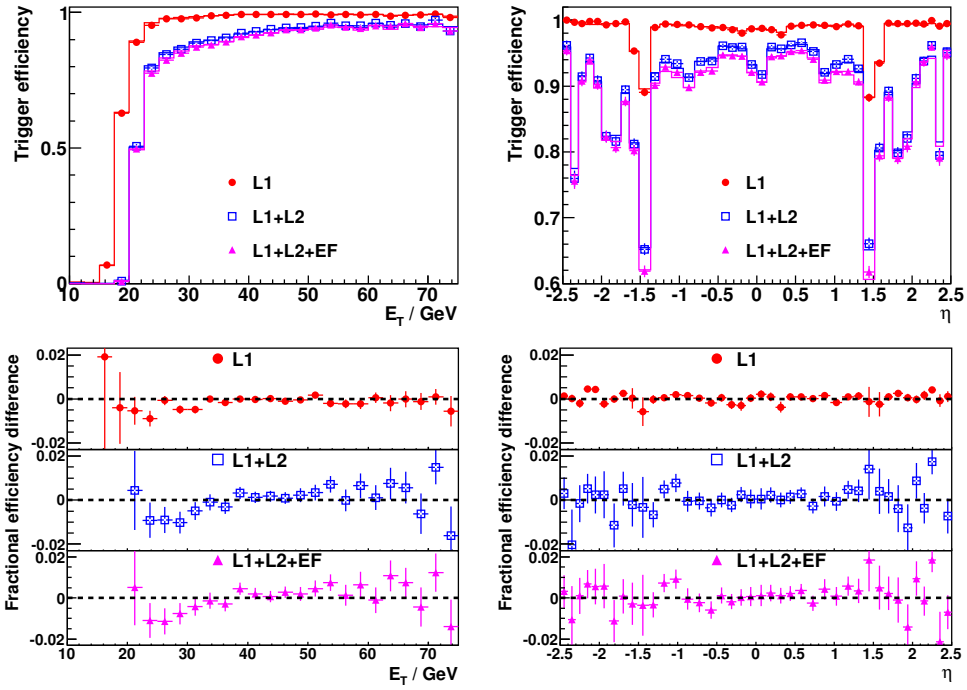

Figure 8.7: Efficiency of the e22i trigger with respect to the "loose" electron selection. Tag and probe results (corresponding to 150 pb^{-1} luminosity) are shown by the points, the corresponding true efficiency by lines. The lower plots show the fractional efficiency difference between the two.

selection cuts is shown in Figure 8.5. This is foreseen to be the lowest threshold unprescaled single electron trigger for a luminosity of 10^{31} cm^{-2}s^{-1}. The p_{T} turn-on curve is similar to that in Figure 8.4. As a function of η, Levels 1 and 2 have a near 100% efficiency outside of the crack region, whilst the efficiency of the Event Filter is approximately 98%. This 2% inefficiency is due to the medium selection cuts not having quite the same definition in the trigger and offline regimes. Again, the measured uncertainties are accurate to within about 0.5%.

Figure 8.6 shows the e20_loose trigger efficiency for electrons passing the loose offline selection. Away from the turn-on region, this trigger is approximately 97% efficient. In η, a reduced performance in the crack region is again clearly visible, and some nonuniformities in the endcap efficiency can also be seen, especially at Level 2. In the central region ($|\eta| < 1.37$), the tag and probe results and the true efficiencies match to within about 0.5%, with some possibly larger discrepancies ($\mathcal{O}(1\%)$) visible in one endcap ($\eta < -1.37$).

Finally, Figure 8.7 shows the efficiency of the e22i trigger for reconstructed electrons which pass the loose offline selection. This trigger is significantly less efficient than the others considered, as it needs to achieve a higher background rejection factor. Therefore, it is also subject to larger statistical uncertainties (*cf* Equation 8.4), despite the greater integrated luminosity (150 pb^{-1}) used for this figure. The turn-on curve above a p_{T} value of 20 GeV/c is measured with a precision of about 1%. The efficiency varies rapidly as a function of the electron η, especially in the forward regions. The tag and probe results successfully measure all of these variations with around 1% precision.

In this section, it has been shown on signal-only simulated samples of $Z/\gamma^* \to e^+e^-$ events that trigger efficiencies can be measured accurately in early data using the tag and probe method. Global efficiencies, applicable only to $Z/\gamma^* \to e^+e^-$ events, can be measured with about 0.1% precision with 150 pb^{-1} of data, if the offline probe preselection is at least as tight as the trigger selection. One-dimensional binned distributions can be measured to within 0.5% and 1% precision, with between 50 and 150 pb^{-1} of data, depending on the trigger and offline selections. A procedure for the removal of background events is discussed next.

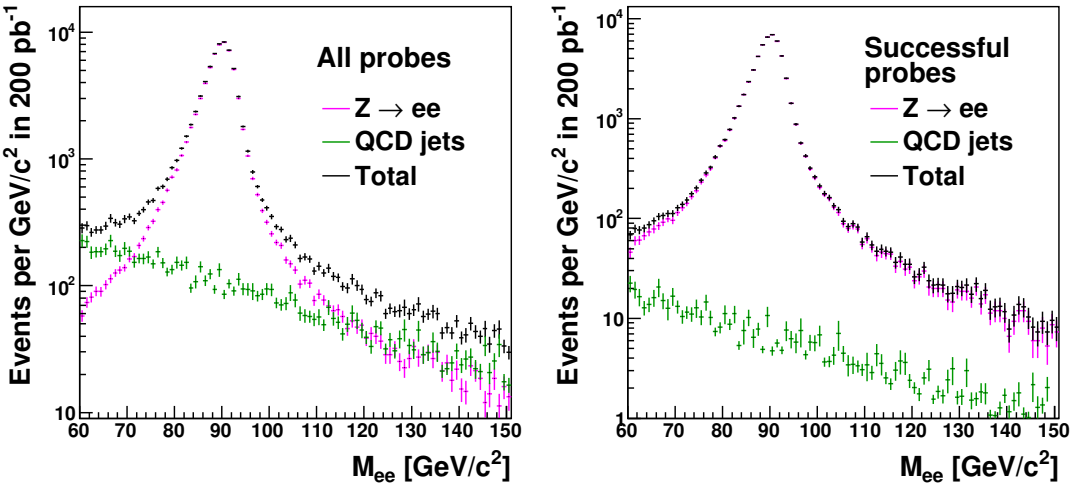

Figure 8.8: Signal and background estimates for a tag and probe analysis of the e22i trigger with respect to the loose electron selection. The tag electron in this analysis is required to pass the tight offline selection cuts, and both electrons must have $p_{\mathrm{T}} > 25$ GeV/c. Both the signal and estimated background are shown before (left) and after (right) the probe trigger selection.

8.4 Background removal

As shown in Chapter 7, the background levels for reconstructed $Z/\gamma^* \rightarrow e^+e^-$ events are expected to be small. As the combination of event and tag preselections also amounts to requiring a triggered event with two selected electrons, this is also true for the tag and probe measurement of trigger efficiencies. Background levels for a difficult, but not unrealistic, tag and probe analysis have been estimated,[17] and are shown in Figure 8.8 for a measurement of the e22i trigger efficiency with respect to the loose offline electron selection (although the tag is required to pass the tight electron selection cuts). While the signal dominates the M_{ee} spectrum after the probe selection, the background levels at the preselection stage are small but significant, and need to be accounted for. One might reasonably expect this to be the case for most trigger efficiencies measured with respect to the loose offline electron selection, and even more so for the measurement of the offline reconstruction and identification efficiencies.

As neither the total jet cross section nor the probability for a jet to pass the electron selection is expected to be well known for the earliest measurements, it is important to

[17]The background component has been estimated using methods similar to those in Chapter 7, with weights calculated separately for jets containing b and c quarks

be able to measure background levels from data. In this section, an approach based on fitting the full M_{ee} distribution, including the signal and background shapes, will be investigated.

One immediate issue is the treatment of the Drell-Yan continuum. As Figure 8.8 shows, this can dominate the background, requiring a consistent treatment in order to avoid bias. In purely physical terms, the Drell-Yan continuum cannot be logically separated from the on-shell Z peak, but for the purposes of a tag and probe analysis, this is irrelevant. As the purpose is to identify well-reconstructed electrons, the Drell-Yan component can be treated as "background" if required, which may simplify the analysis considerably.

8.4.1 The M_Z lineshape

An accurate fit of the reconstructed di-electron mass distribution for signal events requires an appropriate description of the Z/γ^* lineshape, and a realistic treatment of the experimental resolution. Following Equation 10.15 of [19], the theoretical Z/γ^* lineshape can be described by the following:

$$\sigma(\hat{s}) \sim \frac{A}{\hat{s}} \left(\frac{m_0}{\sqrt{\hat{s}}} \right)^{\beta} \left\{ f_{u/d} I_u(\hat{s}) + I_d(\hat{s}) \right\}. \tag{8.5}$$

In Equation 8.5, $\hat{s}$ is the parton collision energy as defined in Equation 2.23, I_u and I_d are the terms relating to up-type and down-type quark interactions, and β will be called the *parton luminosity* factor. This last term parameterises the effect of the *pdf*s on the lineshape, and is normalised to an energy scale m_0, where $f_{u/d}$, the ratio of up-type quark to down-type quark contributions to $\sigma(\hat{s})$, is calculated. It is assumed that $f_{u/d}$ is not dependent on $\hat{s}$. A is a normalisation constant.

The functions $I_u(\hat{s})$ and $I_d(\hat{s})$ describe the Z/γ^* invariant mass distribution, including the Breit-Wigner Z mass peak as well as photon and interference terms. Representing a generic quark by q, this yields

$$I_q(\hat{s}) = C_q^{\gamma} + \frac{\hat{s} M_Z^2}{(\hat{s} - M_Z^2)^2 + \Gamma_Z^2 M_Z^2} \left[(\hat{s} - M_Z^2) C_q^{Z\gamma} + \hat{s} M_Z^2 C_q^{Z} \right]. \tag{8.6}$$

M_Z and Γ_Z are the mass and width of the Z boson, while the coupling constants depend

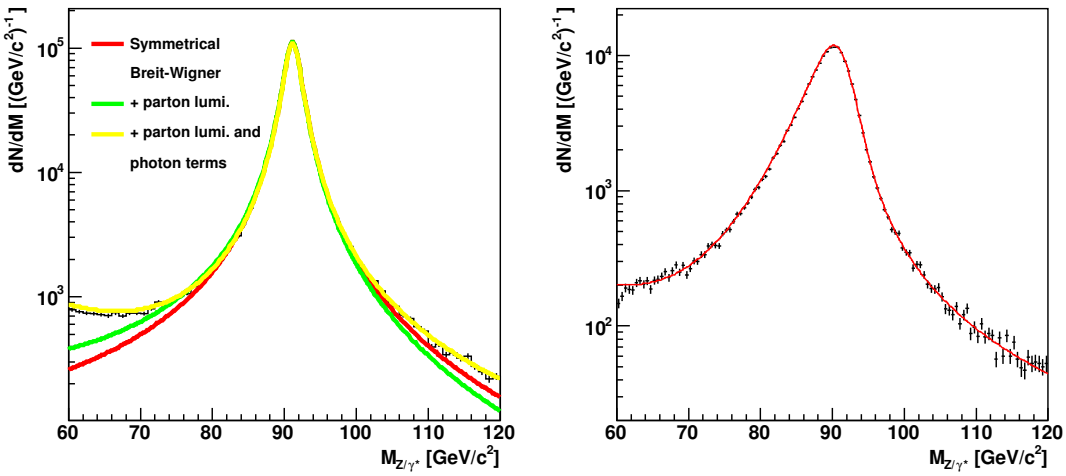

Figure 8.9: Left: Figure showing the effect on the M_{Z/γ^*} distribution of the photon, interference and parton luminosity terms, compared to the PYTHIA truth level distribution. Right: Fit to simulated data of a convolution between the expressions in Equation 8.5 and Equation 8.7. The parton luminosity factor β is obtained from the fit of the yellow curve in the left panel.

on the fundamental quark and electron couplings defined in Table 2.2:

$$\begin{aligned} C_q^{\gamma} &= Q_q, \\ C_q^{Z\gamma} &= 2Q_e Q_q (c_Z^{e_L} + c_Z^{e_R})(c_Z^{q_L} + c_Z^{q_R})\kappa, \\ C_q^{Z} &= 4({c_Z^{q_R}}^2 + {c_Z^{q_L}}^2)({c_Z^{e_R}}^2 + {c_Z^{e_L}}^2)\kappa^2, \\ \kappa &= \frac{\sqrt{2}G_F}{4\pi\alpha} = \frac{1}{4M_W^2 \sin^2\theta_W}. \end{aligned}$$

The photon and interference terms are important when $\sqrt{\hat{s}}$ is far from M_Z, as shown in the left plot in Figure 8.9. This shows a fit of Equation 8.5 to data generated using PYTHIA, with only β and the overall normalisation varied as free parameters. Curves with $\beta = 0$ and without the photon and interference terms are also shown. It is clear from the figure that Equation 8.5 gives the best description of the M_{ee} distribution. However, in the peak region the simple Breit-Wigner also gives a good description. In a combined signal and background fit, using the latter may be more robust as the extra parameters in Equation 8.5 may increase the uncertainty on the fitted fractional background.

8.4.2 Detector resolution

In order to account for imperfect detector resolution, a *Crystal Ball* function has been used [113]. This is defined as follows:

$$f(x) = \begin{cases} Ne^{-\frac{(x-\bar{x})^2}{2\sigma_x^2}} & \text{for } x > (\bar{x} - \alpha), \\ N \cdot \left(\frac{n}{|\alpha|}\right)^n \cdot e^{-\alpha^2/2} \cdot \left(\frac{n}{|\alpha|} - |\alpha| - \frac{x-\bar{x}}{\sigma_x}\right)^{-n} & \text{otherwise.} \end{cases} \tag{8.7}$$

This formula consists of a conventional Gaussian, with mean $\bar{x}$ and width σ_x, attached to a power law distribution with power n such that both the function and its first derivative are continuous. When applied to electron reconstruction, the power law section forms a low energy tail which accounts for bremsstrahlung. The plot on the right of Figure 8.9 shows a fit of the convolution of Equations 8.5 and 8.7 to reconstructed electrons in simulated $Z/\gamma^* \rightarrow e^+e^-$ events. The fit is very good across the full M_Z range considered. For this fit, β from Equation 8.5 was fixed to the fitted value from the left panel of Figure 8.9, while the Crystal Ball component was treated as a resolution function with unit normalisation. A benefit of this approach is that the bias and width of the mass peak can be estimated. The bias, which will include real physics effects related to final state photon radiation, was found to be (-0.84 ± 0.03) GeV/c^2, and the fitted resolution was (1.48 ± 0.02) GeV/c^2, where the uncertainties are statistical.

8.4.3 Tests on simulated FDR data

The *Full Dress Rehearsal* (or FDR [114]) was a chiefly technical exercise undertaken in 2007 and 2008. Its main purpose was to test the computing facilities in place for reconstructing, storing and distributing ATLAS events in real time. During these tests, different models of trigger streaming were tried, and the distributed analysis model (*ie* file replication on the Grid) was tested. The two stages of the FDR are called FDR-1 and FDR-2; only results from FDR-1 are considered here. The files produced for the FDR-1 exercise were generated to have an approximately realistic mix of signal and background events, after the trigger had been taken into account. As such, this was an extremely useful sample on which to test tag and probe methods.

The trigger menu used for FDR-1 consisted of a number of very loosely selecting triggers, each of which was essentially 100% efficient with respect to the offline

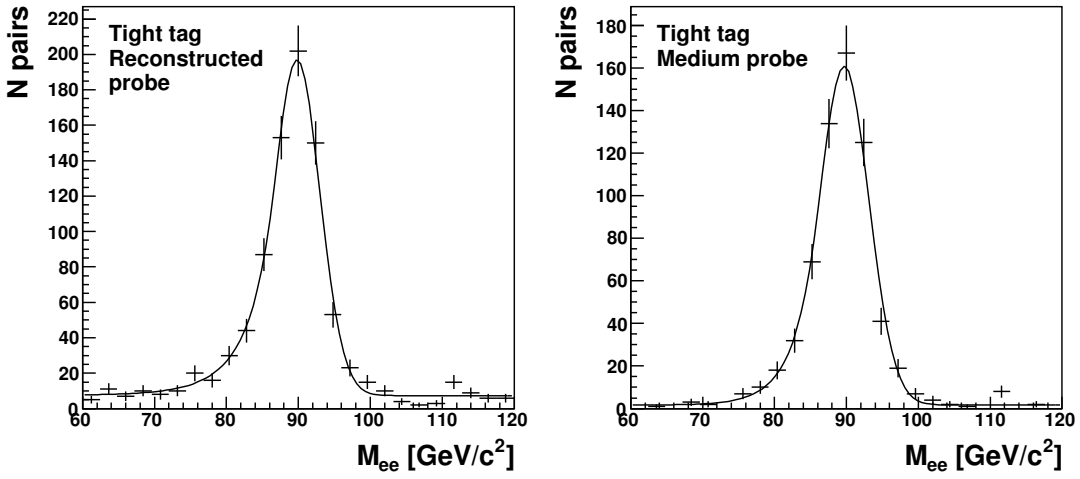

Figure 8.10: Mass distributions from a tag and probe analysis of the medium offline electron identification efficiency using data from the FDR (see text). Distributions include a fit to the invariant mass consisting of a Crystal Ball function added to a constant background. Left: Tag/probe pairs passing the tag and event preselection. Right: Pairs passing the preselection and probe selection.

selection. The subsamples used for tag and probe measurements of these trigger efficiencies were found to suffer from negligible levels of background contamination. More challenging was the measurement of the offline selection efficiency. Fits to the M_{ee} distributions used to calculate the efficiency of the "medium" offline selection are shown in Figure 8.10. The change in background levels from denominator (left) to numerator (right) is clearly visible, while the fits are similar within the peak region.

Due to the limited size of the sample (equivalent to approximately 270 nb^{-1}), only a limited number of bins in M_{ee} could be used for the fit, and only a single average efficiency could be computed. To reduce the number of free parameters in the fit, the Breit-Wigner term was removed, leaving just a Crystal Ball function with an extra term for the background. This is equivalent to assuming that the experimental resolution dominates the observed width. Initially, the background was assumed to follow a falling exponential distribution, $B \sim e^{-\alpha m}$. However, in practice, the constant α was found to be consistent with zero, and the results were refitted using a constant background.

Using this procedure, the "medium" electron identification efficiency was found to be $85 \pm 2\%$, consistent (within the relatively large statistical error) with the efficiency measured on an equivalent signal-only Monte Carlo simulation ($87.7 \pm 0.1\%$). This is

Table 8.3: Table of trigger efficiencies for entire $Z/\gamma^* \to e^+e^-$ events in which both reconstructed electrons passed the specified offline selection. The efficiencies are obtained using the truth information from the simulation, and are given with the uncertainty on the final digit in brackets. The "Bias" columns show the deviation $(\epsilon_{\text{meas}} - \epsilon_{\text{true}})$ from these results when using the tag and probe results binned in η to calculate the event-level trigger efficiency.

Trigger	Loose		Medium		Tight	
	ϵ_{true}	Bias	ϵ_{true}	Bias	ϵ_{true}	Bias
e10_medium	99.60(2)%	-1.3%	99.72(2)%	0.24%	99.978(7)%	0.014%
e15_medium	99.61(2)%	-1.2%	99.72(2)%	0.25%	99.977(7)%	0.015%
e20_loose	99.73(2)%	0.18%	99.83(2)%	0.15%	99.988(5)%	0.008%
e22i	97.81(6)%	1.3%	98.42(5)%	1.2%	99.74(3)%	-0.019%

to be compared with results obtained assuming no background, by simply counting the entries in each histogram. This gives a low, incorrect, efficiency of $72.5 \pm 1.7\%$, thus illustrating the importance of correctly accounting for background effects, and the efficacy of even a relatively crude fitting procedure.

8.5 Systematic uncertainties on the event-level trigger efficiency

The ultimate purpose of measuring the individual electron efficiencies in this context is to calculate the probability that an entire $Z/\gamma^* \to e^+e^-$ event passes the trigger selection. The results of these calculations are shown in Table 8.3. Four triggers have been considered, and the table shows the true probability of a $Z/\gamma^* \to e^+e^-$ event to trigger given that both electrons have passed the stated offline selection, together with the observed bias of a tag and probe estimate of the same efficiency. This efficiency could be estimated using the global single electron efficiencies in Table 8.2, but as the electrons in a $Z/\gamma^* \to e^+e^-$ event are kinematically correlated, this would not be expected to give the correct result. Instead, it has been calculated from the tag and probe results of ϵ_{t} binned in η, with a binning chosen to reflect the structure of the calorimeter.

In the cases where the Event Filter trigger selection is more stringent than the offline selection, large $\mathcal{O}(1\%)$ biases are observed. In the more realistic cases, where the offline selection is at least as tight as that at the Event Filter, biases are still larger than statistical uncertainties but relatively small in absolute terms ($\mathcal{O}(0.2\%)$).

These biases have not been investigated further in this context, but may indicate that a finer binning or a binning in more dimensions of the tag and probe efficiencies would be required to correctly account for kinematic correlations between the two electrons. Similar results are obtained if efficiencies binned in p_{T} are used.

8.6 Tag and probe case studies and robustness tests

As well as providing essential information for physics analyses and validation of the detector simulation, tag and probe efficiency measurements can also be used to detect problems with the detector, the reconstruction or the trigger definitions. This section shows some results, obtained on simulated signal-only samples, which demonstrate the use of tag and probe efficiency measurements to commission or debug the trigger performance.[18]

8.6.1 Study 1: Isolation at Level 1

In Section 5.2.1, the Level 1 selection for electron and photon triggers is described. The primary cut is on the energy within the central towers of the RoI, especially during initial, low luminosity running. However, at medium to high luminosity, it will be essential to introduce further cuts on lateral and longitudinal isolation. The effect of these cuts on the trigger efficiency must be carefully evaluated using data, as shown in this section.

Figure 8.11 shows the tag and probe efficiency of the L1_EM18I trigger as a function of η as the cut on hadronic ring isolation is varied. The L1_EM18I trigger item at Level 1 seeds the e22i trigger in the HLT, which is designed for use at luminosities of 10^{33} cm^{-2}s^{-1} and above. As can be seen in the figure, the trigger efficiency in the central barrel region varies strongly depending on the value of this cut (which is restricted to integer multiples of 1 GeV, a cut of 2 GeV was the default at the time of this study). An overly restrictive cut on this variable can have a significant impact on the trigger performance. This was found to be primarily due to calorimeter noise, which most affects the ring isolation in the central region due to the large calorimeter

[18]The results in this section explore some issues present in one particular version of the trigger software, described in the text. These issues affected only the Level 1 and Level 2 triggers, and are not present in results presented elsewhere unless explicitly noted.

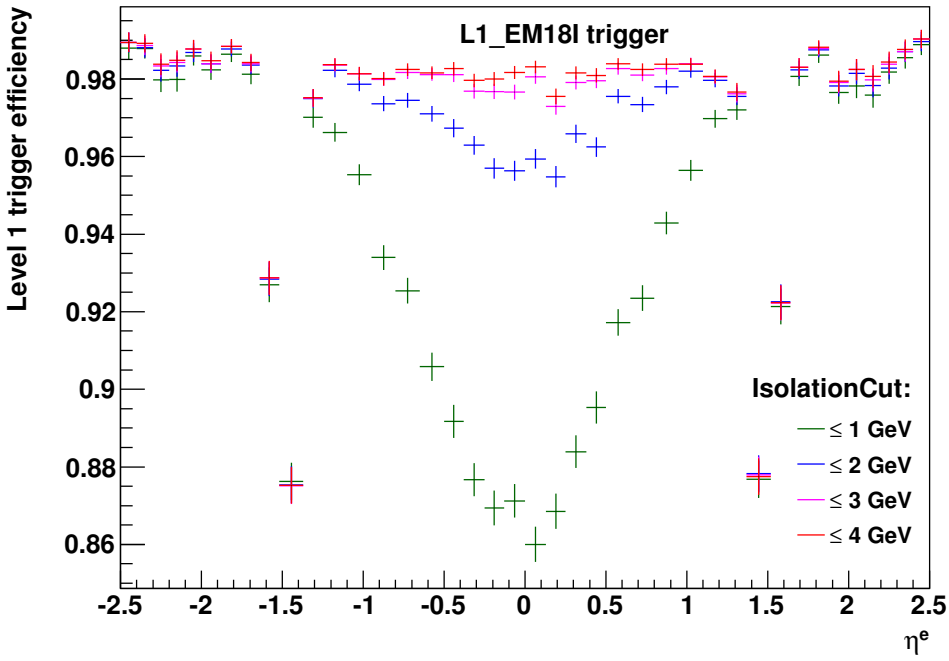

Figure 8.11: Tag and probe efficiency of the L1_EM18I trigger (part of the e22i chain) as a function of the reconstructed η value. Different curves represent different values used for the hadronic isolation cut, where 2 GeV was the default. The efficiency is measured with respect to the offline electron reconstruction.

volumes used in its calculation (see Figure 5.5). Inefficiencies can also be seen in the calorimeter crack region ($|\eta| \sim 1.5$), caused by the relatively poor resolution of the electron E_{T} in this region.

Although Figure 8.11 was produced with simulated events using the tag and probe method, similar studies could be made on real data. Since the tag electron triggers the event, the trigger selection on the probe can be varied offline in an unbiased way. Not only can different trigger levels be examined in isolation, but the effects of individual cuts can also be disentangled relatively easily. It is also possible, and invaluable, to check the performance of more restrictive triggers before they are activated. In summary, trigger performance studies with the tag and probe method allow the verification of trigger definitions on real data as well as checking various aspects of detector performance, such as calorimeter noise.

8.6.2 Study 2: Tracking in Level 2

Figure 8.12 shows the Level 2 efficiency for the e22i trigger for reconstructed electrons passing L1_EM18I. In the particular simulation used, there was an issue with the Inner Detector simulation which had a detrimental effect on the efficiency of the trigger at forward angles, as can be clearly seen in the results shown in red in the top panel of Figure 8.12. The tag and probe results correctly follow the variations in the true efficiency across the full η range, including the complex shapes in the endcap regions. The two-dimensional plot in the lower panel shows that the efficiency also varied strongly as a function of ϕ within the affected regions.

The reason for the poor efficiencies above $|\eta| \sim 1.5$ was that some sections of the SCT endcaps were not correctly positioned in the simulation of the Level 2 trigger. This meant that the probability of fully reconstructing a track was reduced, as well as the chance for reconstructed tracks to pass the quality checks required for selection. The green line in Figure 8.12 shows the efficiency in a resimulated sample after the problem was fixed. The error bars for the resimulated sample are relatively large because only a subset of events were resimulated for this study.

This is an extreme example, which clearly shows how tag and probe measurements can be used to find and debug problems with the trigger, simulation or detector. It also demonstrates that, even in a case where the detector performance is poor (and not understood), the tag and probe method, when used to measure binned efficiencies, produces correct results and is robust against very significant regional variations in the efficiency.

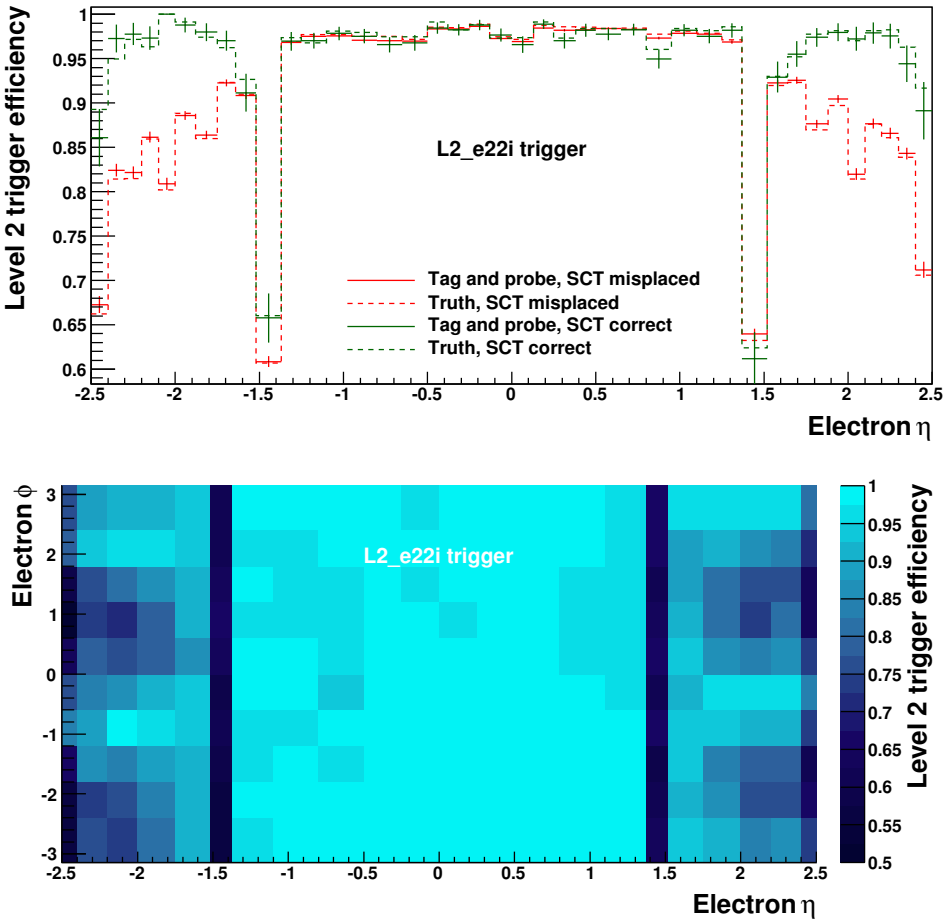

Figure 8.12: Efficiency of the L2_e22i trigger. The efficiency is measured with respect to the offline reconstruction and the Level 1 selection. Top: Efficiencies binned in the reconstructed η value, both with (red) and without (green) the SCT placement bug. Points show tag and probe results, dashed lines show the corresponding true efficiencies. Bottom: Tag and probe efficiency as a function of the electron η and ϕ for the sample with the SCT bug.

Chapter 9

Measuring the inclusive $Z/\gamma^* \rightarrow e^+e^-$ cross section

The previous chapters have dealt with various aspects relating to a measurement of the inclusive $Z/\gamma^* \rightarrow e^+e^-$ cross section in ATLAS. Specifically, various theoretical considerations were discussed in Chapter 3, improved methods for estimating the main backgrounds were presented in Chapter 7, and methods for measuring the electron trigger efficiency from data were introduced in Chapter 8.

For the purposes of this thesis, a likely scenario for early data-taking had to be assumed, and hence all results in this chapter are based on simulated event samples with $\sqrt{s} = 10$ TeV, and the assumption that 200 pb^{-1} of data is obtained. The trigger menu used assumes an average instantaneous luminosity of 10^{31} cm^{-2}s^{-1}, and data has been simulated without pile-up. In the discussion in Chapter 10 the effects of changes in the integrated luminosity and the beam energy will briefly be discussed.

This chapter starts by defining the equations used for extracting the Z/γ^* cross section in Section 9.1. The event selection is described in detail in Section 9.2, which is followed by a description of an event-by-event efficiency corrections method in Section 9.3. Other corrections, for the acceptance, resolution and luminosity are discussed in Section 9.4, and the chapter finishes with a summary of the different uncertainties and some tests of the whole procedure using simulated events in Section 9.5.

9.1 Cross section definitions

The cross section of a process, such as Drell-Yan Z/γ^* boson production in pp collisions, is esentially a measure of its rate, after the delivered luminosity has been accounted

for. Given an instantaneous luminosity $\mathcal{L}$, the event rate R for a process with cross section σ is

$$R = \sigma\mathcal{L} \quad \text{events s}^{-1}. \tag{9.1}$$

In the context of this thesis, σ is the cross section for Drell-Yan production of e^+e^- pairs through the Z/γ^* intermediate state. Thus, it is equal to the total Z/γ^* production cross section multiplied by the branching fraction for the decay into two electrons.

In a perfect experiment, Equation 9.1 could then be used directly to deduce the cross section for a given process given the number of times it occurred in a time interval Δt. However, in practice further corrections are needed, to account for inefficiencies and other detector effects, as introduced in Chapter 3:

$$\sigma_{Z/\gamma^* \to e^+e^-} = \frac{N - B}{\mathcal{A}\mathcal{S}\epsilon \int \mathcal{L}dt}. \tag{9.2}$$

Here, N is the number of selected events in the given luminosity period. B is the total number of background events which pass the selection. The acceptance $\mathcal{A}$, examined in Chapter 3, is an extrapolation factor into unobserved regions of phase space, and must be calculated theoretically. The efficiency ϵ will be defined in such a way that it is a purely experimental quantity that can be measured using the techniques outlined in Chapter 8. It is the probability that electron pairs which are within the detector acceptance will pass all identification and trigger selection cuts. The resolution term $\mathcal{S}$ links ϵ to $\mathcal{A}$ by relating the measured electron parameters to their "true" counterparts.

Equation 9.2 may also be written in terms of the background fraction $f = B/N$. Using this variable, Equation 9.2 becomes

$$\sigma_{Z/\gamma^* \to e^+e^-} = \frac{N(1 - f)}{\mathcal{A}\mathcal{S}\epsilon \int \mathcal{L}dt}. \tag{9.3}$$

The calculation of $\mathcal{A}$ may be improved upon by future theoretical developments, for example as new *pdf* parameterisations become available. It is therefore useful to define a second cross section, which is restricted to the kinematic range considered in the analysis. This will be referred to as the *kinematic* cross section, $\sigma^{\text{kin}}_{Z/\gamma^* \to e^+e^-}$, and it accounts for all detector-level effects, but involves no theoretical extrapolation outside the observed kinematic region:

$$\sigma^{\text{kin}}_{Z/\gamma^* \to e^+e^-} = \frac{N - B}{\mathcal{S}\epsilon \int \mathcal{L}dt} = \frac{N(1 - f)}{\mathcal{S}\epsilon \int \mathcal{L}dt}. \tag{9.4}$$

The total and kinematic cross sections are related simply by

$$\sigma^{\text{kin}}_{Z/\gamma^* \to e^+e^-} = \mathcal{A}\sigma_{Z/\gamma^* \to e^+e^-}, \tag{9.5}$$

and both shall be considered in this analysis.

9.2 Backgrounds and event selection

Many processes in high energy pp collisions have the potential to be falsely reconstructed as $Z/\gamma^* \to e^+e^-$ candidate events. Some of the most important processes were considered in Chapter 7, including the hadronic QCD backgrounds, electrons from the decays of heavy flavour mesons and baryons, and fake tracks combined with EM calorimeter deposits. Other backgound processes include semi- and fully-leptonic $t\bar{t}$ events and the electroweak boson decay channels $W \to e\nu_e$, $W \to \tau\nu_\tau$ and $Z/\gamma^* \to \tau^+\tau^-$, all of which have been simulated separately. The details of these simulated events, including generator-level filters, were given in Chapter 3, and all quoted selection efficiencies are measured with respect to these samples. The cross sections of most processes considered are known to at least NLO precision in QCD. However, as the NLO correction to the filtered event sample cross section is not known, and as this is the major source of background for this analysis, LO cross sections have been used throughout. The only exception is for the $t\bar{t}$ sample, which was generated using MC@NLO. For this process alone, the NLO cross section was used.

To separate the $Z/\gamma^* \to e^+e^-$ signal from these backgrounds, a number of cuts have been applied. These cuts are listed in Table 9.1, and the number of events passing each set of selection criteria are given in Table 9.2. The various cuts are considered in detail below.

9.2.1 Trigger

The electron triggers serve a twofold purpose. Firstly, they act as an initial event selection, designed to discriminate between real electrons and QCD jets. Secondly, they filter out low p_{T} electrons, which tend to come from low-Q^2 processes. The two main single electron triggers anticipated for $\mathcal{L} = 10^{31}$ cm^{-2}s^{-1} running are called e10_medium and e20_loose (recall the trigger naming convention introduced in Section 5.2). In Chapter 7,

Table 9.1: Event selection cuts for the $Z/\gamma^* \rightarrow e^+e^-$ analysis in the order in which they are applied.

Cut #	Description
1	Event passes "e10_medium" trigger.
2	Preselection: Two reconstructed electrons with $p_{\mathrm{T}}^{\mathrm{e}} > 10$ GeV/c and $M_{ee} > 40$ GeV/c^2.
3	Acceptance cuts: $p_{\mathrm{T}}^{\mathrm{e}} > 15$ GeV/c and $\lvert\eta^e\rvert < 2.47$, with $1.37 < \lvert\eta^{\mathrm{calo}}\rvert < 1.52$ excluded.
4	"Medium" electron selection cuts applied.
5	Require opposite charge tracks.
6	Invariant mass: 70 GeV/$c^2 < M_{ee} < 110$ GeV/c^2.

event selections based on both of these triggers were considered. Here, e10_medium will be used because of its greater potential acceptance. It can be seen in Table 9.2 that the (predominantly hadronic) background in the filtered event sample is reduced by a factor of over 100 by the application of this trigger. Over half of the simulated $t\bar{t}$ events also fail the trigger, although this is expected as many of these events feature muonic, not electronic, W decays. The backgrounds involving high p_{T} tau leptons ($W \rightarrow \tau\nu_\tau$ and $Z/\gamma^* \rightarrow \tau^+\tau^-$) are also supressed by the trigger, due to a combination of acceptance effects and the $\tau \rightarrow e$ branching fraction.

9.2.2 Preselection

Following the trigger requirements, a loose preselection is applied in order to pick out events of interest for the main analysis. This preselection requires the event to have two reconstructed electrons with $p_{\mathrm{T}}^{\mathrm{e}} > 10$ GeV/c, and $M_{ee} > 40$ GeV/c^2. This preselection essentially amounts to requiring a second (very loose) electron-like object in addition to the electron already selected by the trigger.

This is a very effective cut because for most of the backgrounds (except $t\bar{t}$), no second high p_{T} electron is present. In these cases, the second electron would usually come from a misidentified hadronic jet. Even if reconstructed as electron candidates, these are unlikely to pass further identification cuts required later.

Table 9.2: Cut flow for the e10_medium selection. For the filtered event sample (described in Section 3.1.1), the figures in the last three rows are estimated using the techniques of Chapter 7. Only statistical uncertainties are shown.

		Number of events / 1000		
	Cut	$Z/\gamma^* \to e^+e^-$	Filtered Events	$t\bar{t}$
0	No cuts	219.64(10)	$2.0629(7) \times 10^7$	40.57(3)
1	Trigger	172.96(9)	$1.014(5) \times 10^5$	13.55(2)
2	Preselection	91.30(6)	5270(110)	10.12(2)
3	Acceptance	75.99(6)	1890(60)	8.087(15)
4	Selection	57.57(5)	4.2(4)	0.430(3)
5	Charge	57.14(5)	2.1(2)	0.404(3)
6	Inv. mass	54.59(5)	0.52(9)	0.130(2)
	Cut	$W \to e\nu_e$	$W \to \tau\nu_\tau$	$Z/\gamma^* \to \tau^+\tau^-$
0	No cuts	2062.6(9)	731.5(12)	225.7(3)
1	Trigger	1252.5(7)	110.2(5)	22.26(9)
2	Preselection	57.0(2)	4.74(9)	3.66(4)
3	Acceptance	32.08(12)	2.84(7)	2.28(3)
4	Selection	0.126(7)	0.004(3)	0.277(10)
5	Charge	0.084(6)	0.002(2)	0.271(10)
6	Inv. mass	0.025(3)	0.002(2)	0.029(3)

9.2.3 Acceptance

Next, the full kinematic selection is applied. One of the principal kinematic constraints on electron reconstruction is the acceptance of the Inner Detector, which can reconstruct charged tracks within $|\eta| < 2.5$. However, the acceptance cut has been placed at $|\eta| = 2.37$, where the EM calorimeter technology changes. In particular, the first calorimeter layer, useful for background rejection, is less finely segmented in $|\eta|$ at higher pseudorapidities. It is assumed that the forward regions of the EM calorimeter will not be fully understood in the first data. Furthermore, the transition region between the barrel and endcaps of the electromagnetic calorimeter has been removed from consideration, as increased dead material in this region for services and cryostats degrades the calorimeter's energy resolution. This corresponds to the region $1.37 < |\eta| < 1.52$, where $|\eta|$ is from the calorimeter measurement.

The other cut applied at this stage is one of $p_{\mathrm{T}}^{\mathrm{e}} > 15$ GeV/c. The value of this cut has been chosen 5 GeV/c higher than the trigger p_{T} cut, which will eliminate trigger turn-on effects and further reduce the QCD backgrounds. These cuts together remove 64% percent of the background from the filtered event sample, for less than a 17% reduction in signal. A significant portion of the loss of signal comes from removal of the calorimeter crack region. The other backgrounds typically involve high p_{T} particles, and are less affected by these cuts than the QCD background.

9.2.4 Selection

In Section 5.1.4, the three main levels of electron identification were described. These are called the "loose", "medium" and "tight" selections, in increasing order of background rejection power (and decreasing signal efficiency). It was shown in Chapter 7 that the loose selection does not ensure a sufficiently pure $Z/\gamma^* \rightarrow e^+e^-$ signal for precision analysis. It was also shown that the medium electron selection should be sufficient to reduce background levels to $\mathcal{O}(1-2\%)$. Using the tight selection would reduce the backgrounds even further, but this appears to be unnecessary, especially as these cuts are more than 10% less efficient than the medium electron selection [42]. Therefore, the medium selection will be used in this analysis.

As noted above, the "second" electron in background events often originates from a jet or an electron from a leptonic b or c decay embedded in a jet. The application of the medium selection criteria to both electrons reduces the combined backgrounds from the filtered event sample to a level smaller than the $Z/\gamma^* \to e^+e^-$ signal for the first time, and from this point on the number of background events is obtained using the scaling method described in Chapter 7. The other backgrounds, except those from $Z/\gamma^* \to \tau^+\tau^-$, are all reduced by at least an order of magnitude.

9.2.5 Charge

The electrons from a Z/γ^* boson decay are expected to have opposite reconstructed charges, in the absence of misreconstruction. This is not expected to be true for the dominant QCD backgrounds, which are assumed to be reduced by 50% upon applying this requirement. This assumption has been checked on events in the filtered sample which pass the selection (rather than being scaled), and it appears to be accurate within the very limited available statistics. The amount by which this cut rejects the other backgrounds varies depending on the degree of charge correlation between the reconstructed electron candidates in these events.

9.2.6 Di-electron mass

Finally, a cut is imposed on the invariant mass of the electron pair. This serves to reduce the contribution from the Drell-Yan continuum and also from the backgrounds, which are largely non-resonant. The $Z/\gamma^* \to \tau^+\tau^-$ background is resonant, but the neutrinos in the τ lepton decays shift the mean di-electron mass down to approximately 50 GeV/c^2. Only electron pairs with $70 < M_{ee} < 110$ GeV/c^2 are kept in this analysis. This mass range should encompass the entire Z mass peak including resolution effects.

9.2.7 Resultant background

The M_{ee} spectrum for the signal and all considered backgrounds is shown in Figure 9.1, after application of all cuts except the di-electron invariant mass cut. The filtered event sample forms the largest single background component, approximately 5 times larger than the $t\bar{t}$ background. The overall background level is small however,

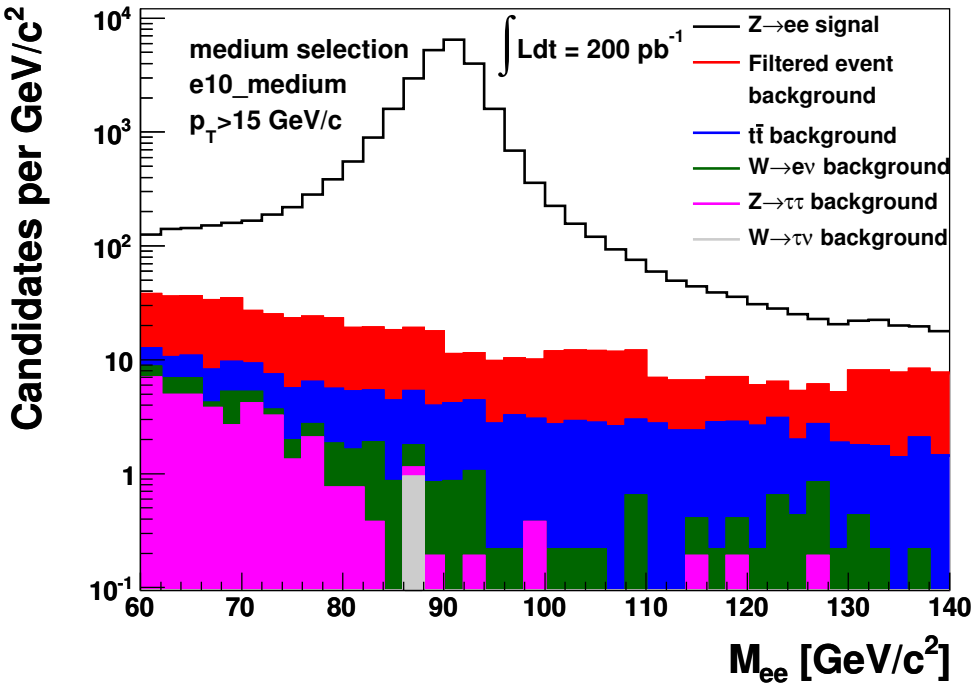

Figure 9.1: Cumulative expected signal and background as a function of M_{ee} for 200 pb^{-1} after cut 5 of Table 9.1. The contribution from filtered events has wider binning than the other components, and it is produced as described in Chapter 7.

and the signal even dominates in the tail regions far from $M_{ee} = M_Z$. Within the window $70 < M_{ee} < 110$ GeV/c^2, the estimated total background is approximately 1.3% of the $Z/\gamma^* \rightarrow e^+e^-$ signal. The statistical uncertainty on this ratio is about 10%, but the uncertainties in the background scaling method, QCD jet cross section and electron selection performance are significantly larger. In Chapter 7, it was estimated that the scaling method itself may introduce a systematic uncertainty of 10% on the total number of background events from the filtered event sample. Various estimates exist for the uncertainty of the jet cross section itself. Furthermore, electron fake rates in data may not correspond to those in the simulation during early ATLAS operation. Following the studies of inclusive electroweak boson cross section measurements in [42], an uncertainty of 100% shall be assumed on the combination of all these factors, applied to the filtered event sample. The uncertainties on the other backgrounds will be neglected as they contribute less to the total background and their cross sections are known with much greater precision.

In the future, the uncertainty on the QCD background (which in this case includes

$b, c \rightarrow e$ decays) will be reduced by various measurements made with ATLAS. The jet cross section can be directly constrained by the measurement of high p_{T} jets, with and without flavour identification. Additionally, the shape of the background M_{ee} spectrum can be measured using reconstructed electron candidates before selection or with inverted selection cuts, to obtain a sample in which QCD backgrounds dominate. The normalisation of the QCD background can be obtained by fitting distributions of control variables, as has been done in the CDF experiment [115, 116]. Finally, the contributions from heavy flavour decays could be reduced by applying further cuts on the lateral isolation of the electron candidates.

9.3 Event-level efficiency corrections

Once all cuts are applied, it is necessary to correct for detector effects, notably electron reconstruction and identification inefficiencies. With a uniform detector response, these corrections could be applied as a single factor ϵ, but it will be shown that the various corrections vary over the electron kinematic phase space. For this reason, corrections are applied on an event-by-event basis.

It is intended that these efficiency corrections can be measured from data, and therefore they refer entirely to reconstructed quantities. These corrections are not applied following the order in which the cuts are applied, but follow the scheme presented in Section 8.2 and used throughout [42]. This scheme corrects back to reconstructed calorimeter clusters within the applied acceptance cuts. In the ATLAS simulation, over 99.8% of true electrons within $|\eta| < 2.5$ and $p_{\mathrm{T}} > 10$ GeV/c are associated with a reconstructed cluster, leaving a small residual correction for resolution effects that is accounted for in the smearing correction $\mathcal{S}$ described later.

Using reconstructed calorimeter clusters as a starting point, corrections are applied sequentially to allow for the efficiencies of electron reconstruction (*ie* very loose track association), electron identification cuts, correct charge association and the trigger selection. This facilitates the combination of different performance measurements obtained from data, allowing each to be understood separately. Each efficiency is measured relative to the last, and calculated in terms of the E_{T} and η of the electro-

magnetic cluster. These have been calculated on simulated $Z/\gamma^* \to e^+e^-$ events using the following equations:

$$\epsilon^e_{\text{reco}} = \frac{N^e_{\text{reco}}(E^{\text{clus}}_{\text{T}}, \eta^{\text{clus}})}{N^e_{\text{clus}}(E^{\text{clus}}_{\text{T}}, \eta^{\text{clus}})}, \tag{9.6}$$

$$\epsilon^e_{\text{id}} = \frac{N^e_{\text{reco+id}}(E^{\text{clus}}_{\text{T}}, \eta^{\text{clus}})}{N^e_{\text{reco}}(E^{\text{clus}}_{\text{T}}, \eta^{\text{clus}})}, \tag{9.7}$$

$$\epsilon^e_{q} = \frac{N^e_{\text{reco+id+charge}}(E^{\text{clus}}_{\text{T}}, \eta^{\text{clus}})}{N^e_{\text{reco+id}}(E^{\text{clus}}_{\text{T}}, \eta^{\text{clus}})}, \tag{9.8}$$

$$\text{and} \quad \epsilon^e_{\text{trig}} = \frac{N^e_{\text{reco+id+charge+trig}}(E^{\text{clus}}_{\text{T}}, \eta^{\text{clus}})}{N^e_{\text{reco+id+charge}}(E^{\text{clus}}_{\text{T}}, \eta^{\text{clus}})}. \tag{9.9}$$

The above efficiencies are then combined into one overall event efficiency for each electron pair:

$$\begin{aligned} \epsilon_{\text{Event}} &= \epsilon_{\text{reco}} \cdot \epsilon_{\text{id}} \cdot \epsilon_q \cdot \epsilon_{\text{trig}} \\ &= (\epsilon^{e1}_{\text{reco}}\epsilon^{e2}_{\text{reco}}) \cdot (\epsilon^{e1}_{\text{id}}\epsilon^{e2}_{\text{id}}) \cdot (\epsilon^{e1}_{q}\epsilon^{e2}_{q}) \cdot (\epsilon^{e1}_{\text{trig}} + \epsilon^{e2}_{\text{trig}} - \epsilon^{e1}_{\text{trig}}\epsilon^{e2}_{\text{trig}}). \end{aligned} \tag{9.10}$$

The efficiency of each event is then used to calculate N_{corr}, the number of events corrected to the level of reconstructed EM calorimeter clusters within the acceptance:

$$N_{\text{corr}} = \sum_{\text{Events}} \frac{1}{\epsilon_{\text{Event}}}. \tag{9.11}$$

This term replaces the factor N/ϵ in the equations of Section 9.1.

Constructing the event efficiency in this way allows all of the efficiency factors in Equation 9.11 to be measured from data using tag and probe techniques (as discussed in Chapter 8 for ϵ_{trig}). It is expected that such measurements in early data may result in corrections to the simulated efficiencies or modifications to the assigned systematic uncertainties. As more data accumulates, it may be possible to replace the simulated estimates entirely by tag and probe measurements. The terms making up ϵ_{Event} and the other correction factors in Equations 9.2 and 9.4 will now be discussed.

9.3.1 Reconstruction efficiency

Recalling Section 5.1, electron reconstruction in ATLAS consists first of locating energy deposits in the electromagnetic calorimeter, and then associating tracks with these clusters. The electron reconstruction efficiency defined in Equation 9.6 measures the

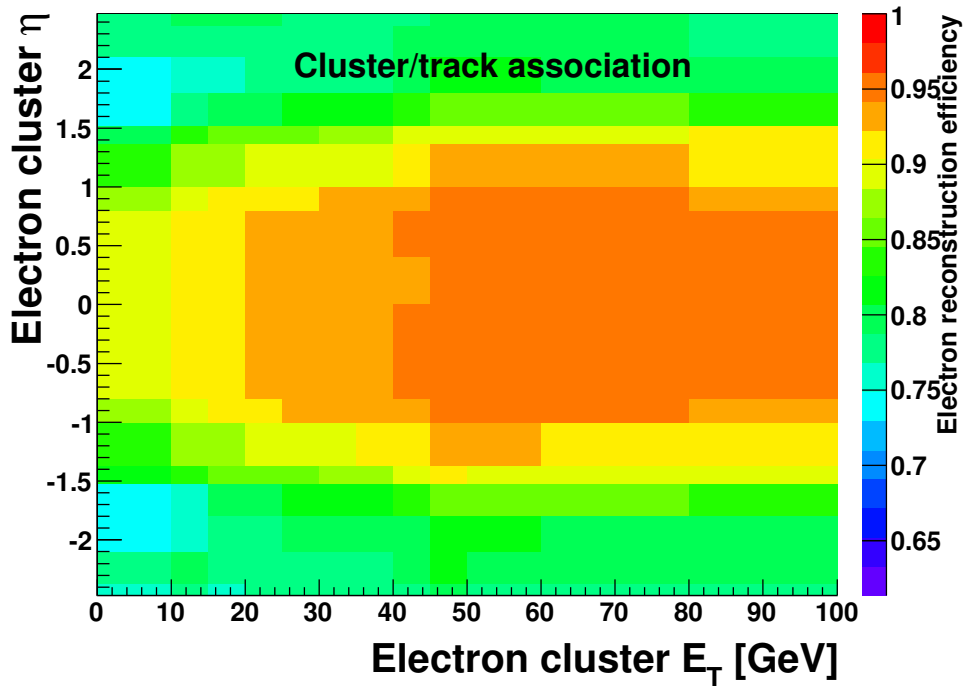

Figure 9.2: Electron reconstruction efficiency as a function of the cluster E_{T} and η in $Z/\gamma^* \to e^+e^-$ events. "Reconstruction" refers to basic track and cluster matching, before electron identification cuts are applied. The cluster reconstruction efficiency is greater than 99.8%. Statistical uncertainties vary from below 0.2% at $E_{\mathrm{T}} = 40$ GeV, to 0.75% at high E_{T}, and larger in the crack regions.

track association probability for reconstructed clusters, and it is shown in Figure 9.2. Centrally produced electrons with $E_{\mathrm{T}} \gtrsim 40$ GeV have about a 95% chance of being reconstructed, while those in the forward regions and at low E_{T} have a lower chance of being reconstructed. The track reconstruction efficiency for high p_{T} electrons in the forward regions (above $|\eta| \approx 1$) averages around 80%, due to significant increases in the amount of Inner Detector material in these regions causing increased multiple scattering and bremsstrahlung. Electrons with low p_{T} (hence low measured E_{T}) are more affected by material in all regions of the detector, causing up to a 5% drop in efficiency for clusters with $E_{\mathrm{T}} < 15$ GeV. These results are in good agreement with those presented in the Tracking chapter of [42]. At a later stage of running, more advanced tracking algorithms may be used to detect bremsstrahlung, and hence recover some of the efficiency losses.

A direct measurement of the electron reconstruction efficiency on data using the tag and probe method is expected to be difficult. This is because the probe elec-

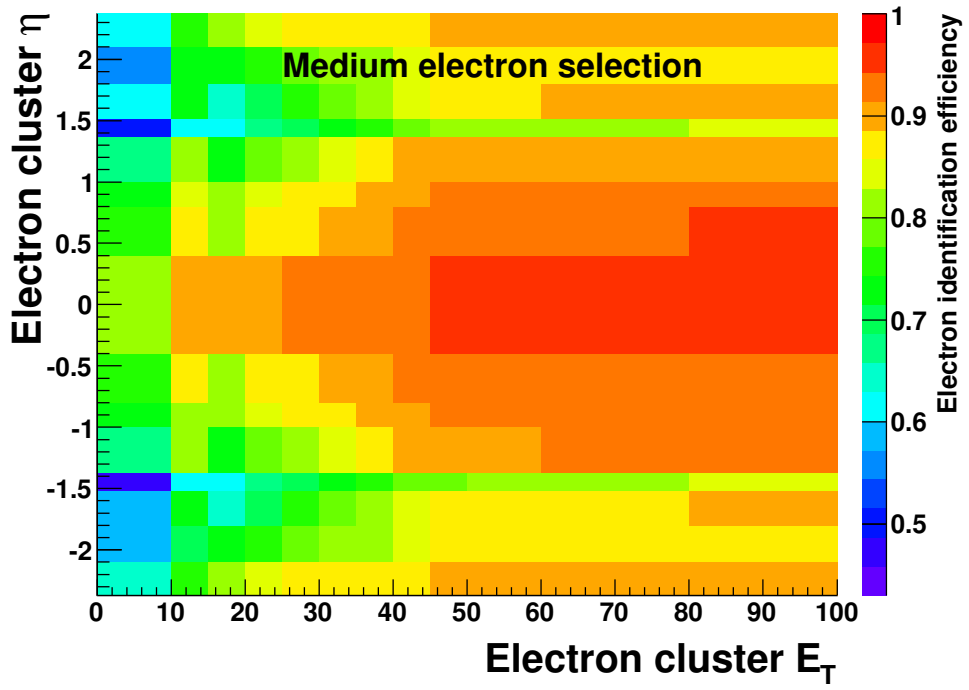

Figure 9.3: Efficiency of the medium electron selection cuts for reconstructed electrons as a function of the cluster E_{T} and η in $Z/\gamma^* \rightarrow e^+e^-$events. Statistical uncertainties vary from below 0.2% at $E_{\mathrm{T}} = 40$ GeV, to 0.6% at high and low E_{T}, and larger in the crack regions.

tron must begin with an extremely loose selection (*ie* just an energy deposit in the EM calorimeter), which introduces significant background contributions. The measurement is however feasible using lineshape fitting procedures such as those discussed in Section 8.4. The systematic uncertainty on ϵ_{reco} will be treated in combination with the identification efficiency discussed below.

9.3.2 Identification efficiency

Once an electron is reconstructed, further identification cuts are applied in order to reduce the background contribution. The probability for a reconstructed electron to pass the medium selection cuts is shown in Figure 9.3. The average identification efficiency is around $85 - 90\%$, but efficiencies vary significantly over the E_{T} and η range considered. Efficiencies are lower in the forward regions ($|\eta| > 1.5$) and at low E_{T}. In the forward regions, the efficiency is reduced due partly to extra Inner Detector material, but also due to changes in the applied selection cut values, aimed at improving the rejection of jets in this region. At low E_{T}, it is more difficult to

discriminate between electromagnetic and hadronic particles using shower shape cuts, resulting in a lower efficiency. A more complete description of these points can be found in the "Reconstruction and Identification of Electrons" chapter of [42].

This chapter of [42] also includes a discussion on how accurately the electron reconstruction and identification efficiencies can be measured using the tag and probe method on early data. Overall, it was estimated that the product $\epsilon^e_{\text{reco}}\epsilon^e_{\text{id}}$ could, on average, be measured with a 2% precision with 50 pb^{-1} of data. That study was made using simulated events with $\sqrt{s} = 14$ TeV. Assuming a similar result at $\sqrt{s} = 10$ TeV, this is expected to yield a 1% precision with 200 pb^{-1} of data, as the uncertainties on the measured efficiencies are primarily statistical. These uncertainties are taken as the systematic uncertainties on the simulated efficiencies. Assuming that these uncertainties are in general correlated between the electrons (which is the most conservative assumption), the corresponding uncertainty on the product $\epsilon_{\text{reco}}\epsilon_{\text{id}}$ for the event is approximately 2%.

9.3.3 Charge misidentification

Figure 9.4 shows the probability of misidentifying the charge of an electron which has passed the medium selection cuts. In the central region ($|\eta| < 1.5$), this probability is generally below 0.5%. It increases in the forward direction, where charged particles experience less of the Inner Detector's magnetic field and where increased multiple scattering can lead to an incorrect charge assignment. The charge misidentification probability is also higher for high p_{T} tracks, as they have a smaller sagitta than low p_{T} tracks, making charge assignment more challenging.

The charge identification efficiency could be measured using a variant of the tag and probe method presented in Chapter 8, to compare the number of $Z/\gamma^* \to e^+e^-$ candidates with oppositely charged electrons to the total number of candidates with no charge requirement. Equivalently, events with like-sign electron tracks could be examined to measure the charge misidentification rate. In either case, bias from mismeasured tracks on the reconstructed electron kinematics (p_{T}, η, ϕ) should be avoided by taking these measurements from the matching calorimeter clusters.

The low charge misidentification rate ensures that the charge-matching correction

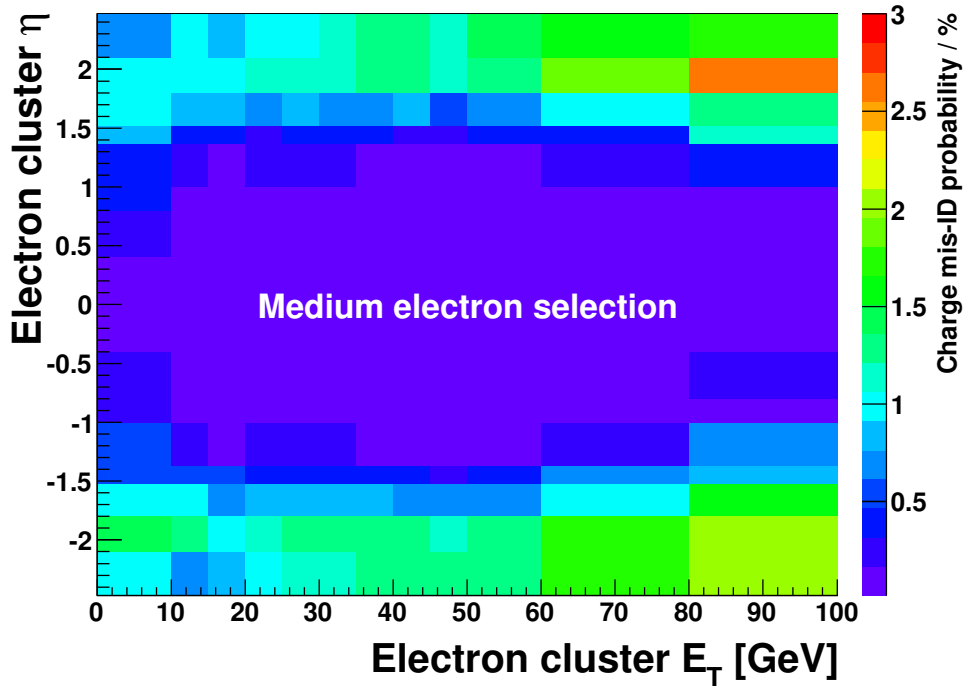

Figure 9.4: Charge misidentification rate for reconstructed electrons passing the medium selection cuts as a function of the cluster E_{T} and η in $Z/\gamma^* \to e^+e^-$ events. Statistical uncertainties vary up to 0.3% in the forward direction for the highest E_{T} bin, and are below 0.1% for electrons with $|\eta| < 1$ or $20 < E_{\mathrm{T}} < 40$ GeV.

term ϵ_q produces a change of less than 1% in the measured cross section, and its uncertainty will be neglected.

9.3.4 Trigger efficiency

Compared to the reconstruction and identification efficiencies, the contribution of ϵ_{trig} to the event efficiency is very small. This is due to the definition of the trigger efficiency correction, which is defined with respect to events that have already passed the medium offline selection. The efficiency of the e10_medium trigger for identified electrons is shown in Figure 9.5. This efficiency is generally very high, consistently above 99% in the central region ($|\eta| < 1.37$) and lower in the forward regions, averaging about 98% for electrons with $E_{\mathrm{T}} = 40$ GeV.

Only one electron needs to pass the e10_medium trigger selection to trigger an event. For electrons within the acceptance cuts, the trigger efficiency $\epsilon^{\mathrm{e}}_{\mathrm{trig}}$ is always greater than 95%, resulting in a worst-case event-level efficiency that is still better than 99.75%. The uncertainty on this correction will therefore be neglected, as the correction itself

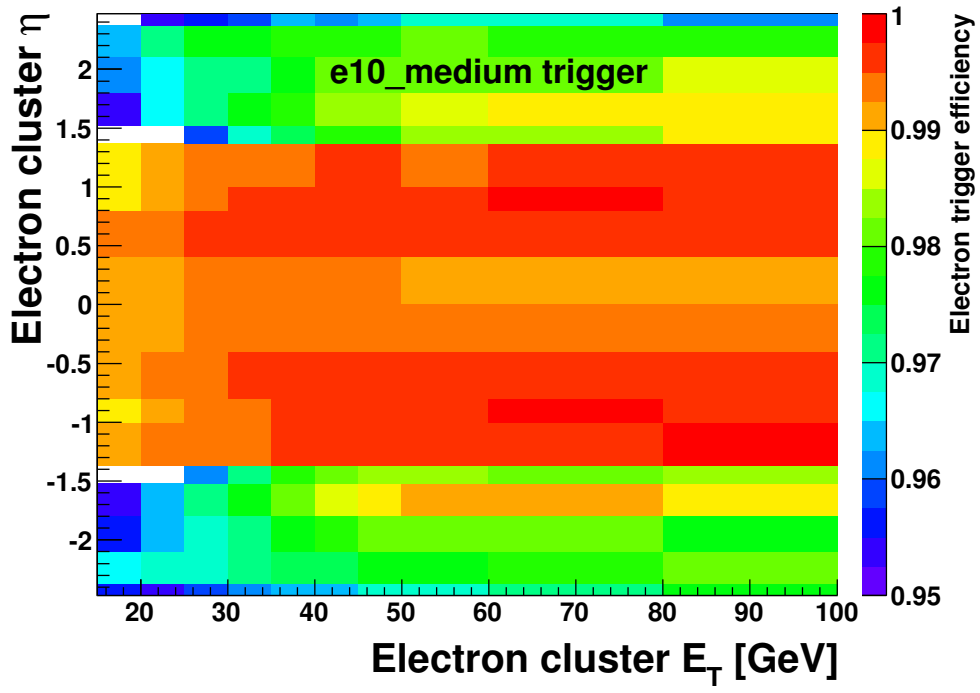

Figure 9.5: Efficiency of the e10_medium trigger for reconstructed electrons passing the medium offline selection cuts and a correctly assigned charge as a function of the cluster E_{T} and η in $Z/\gamma^* \to e^+e^-$ events. The trigger efficiency in the white regions is less than 95%. Statistical uncertainties vary from 0.1% and below at $E_{\mathrm{T}} = 40$ GeV to 0.4% at high and low E_{T}, and larger in the crack regions.

is so small.

9.3.5 Summary

Figure 9.6 shows the di-electron invariant mass spectrum after the simulation-based event-by-event corrections in Equation 9.11 have been applied, but before the other corrections are included, and before the invariant mass cut is applied. The backgrounds cannot be separated from the signal on an event-by-event basis in data, and are corrected using the same factors as were applied to the signal. Subsequent to the efficiency correction, the background fraction is remeasured and found to be $1.6 \pm 1.3\%$ within the mass range of $70 - 110$ GeV/c^2. The increase in the background fraction from 1.3% is partly due to the reconstructed electrons in the filtered event sample being concentrated at low values of $p_{\mathrm{T}}^{\mathrm{e}}$ where the signal reconstruction and identification efficiencies are lower.

The effect of the event-level efficiency corrections on the measured boson distri-

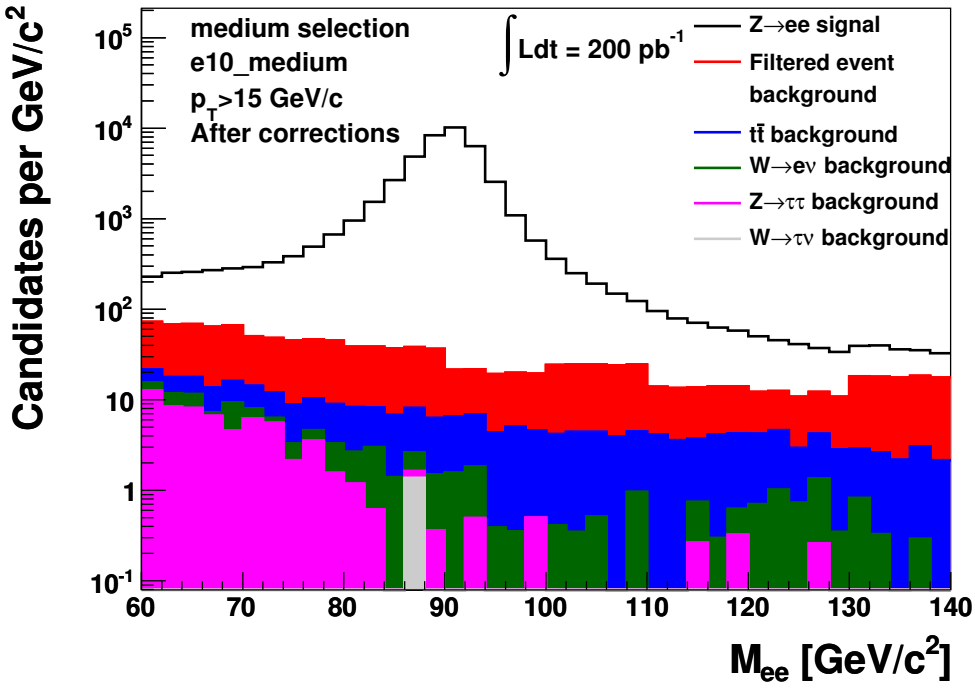

Figure 9.6: Cumulative expected signal and background as a function of M_{ee} for 200 pb^{-1} after the efficiency corrections of Section 9.3 but before cut 6 of Table 9.1. The contribution from filtered events has wider binning than the other components, and it is produced as described in Chapter 7.

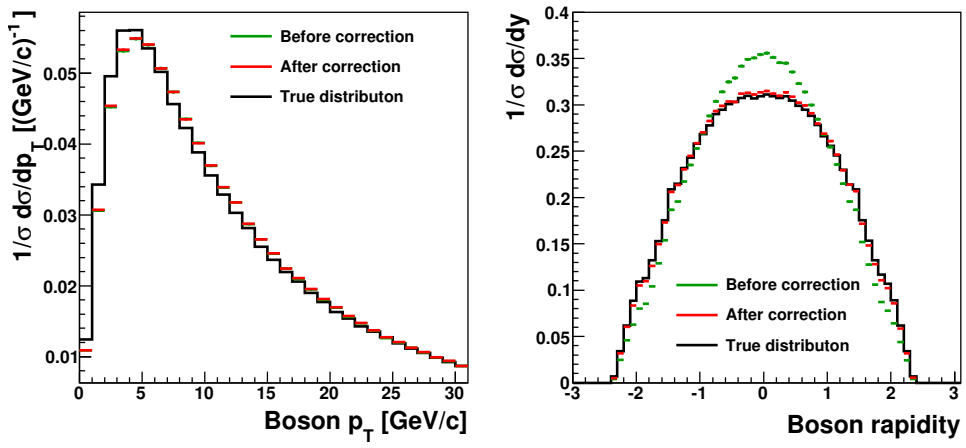

Figure 9.7: Comparison of the normalised differential Z/γ^* boson cross section before and after event-level corrections, but without explicit bin migration corrections. Left: as a function of the boson p_{T}. Right: As a function of the boson rapidity.

butions is shown in Figure 9.7. This figure shows the p_{T} and rapidity of di-electron pairs passing the event selection from the signal sample before and after correction, compared to the theoretical distribution of bosons from PYTHIA. Bin migration effects have not yet been considered, resulting in some biases in the $p_{\mathrm{T}}^{\mathrm{Z}}$ spectrum for $p_{\mathrm{T}}^{\mathrm{Z}} < 20$ GeV/c. The rapidity spectrum, where migration effects are expected to be smaller, agrees well with the true spectrum once the event-by-event efficiency corrections are applied. Applying a binned migration correction should improve this even further.

9.4 Further corrections

9.4.1 Acceptance

The acceptance factor $\mathcal{A}$ accounts for events where one or both electrons from a Z/γ^* decay fall outside the kinematic range considered in the analysis. This has been estimated by looking at the truth record of simulated signal events, as in Chapter 3. The primary simulated sample has a lepton filter applied, which rejects events with no electron in the region $|\eta| < 2.8$. To determine the acceptance correction, a separate sample of 735,000 events was used, generated without this filter. The four kinematic cuts of Table 9.2 were applied to this sample, namely $p_{\mathrm{T}}^{\mathrm{e}} > 15$ GeV/c, $|\eta| < 2.37$, the exclusion of $1.37 < |\eta| < 1.52$, and $70 < M_{ee} < 110$ GeV/c^2. Following the discussion at the end of Chapter 3, the acceptance was calculated after electrons were recombined with photons separated by less than $\Delta R_{\mathrm{cut}} = 0.05$, to reduce theoretical uncertainties. Overall, 37.23% of events pass these criteria, with a statistical uncertainty of 0.06%, and a systematic uncertainty (estimated in Chapter 3) of 1.6%.

9.4.2 Resolution correction

The limited resolution of the reconstructed electron variables may lead to migration of events across the boundaries of the chosen acceptance region. A correction factor $\mathcal{S}$ is determined which represents the difference between the acceptance derived theoretically and the number of accepted events applying equivalent cuts to the detector variables. This correction was determined using events with two reconstructed electrons passing the medium identification cuts, correctly matched (with $\Delta R < 0.1$ and correct charge)

to true electrons, but without explicit kinematic cuts applied. As with the acceptance calculation, the true electrons were recombined with nearby photons. The acceptance and mass cuts of Table 9.2 were then applied separately to the true and reconstructed electrons in these events. The resolution correction $\mathcal{S}$ is defined as the ratio of the number of events passing the acceptance cuts in each case:

$$\mathcal{S} = \frac{N_{\mathcal{A}}^{\text{reco}}}{N_{\mathcal{A}}^{\text{true}}} = 0.9894 \pm 0.0013(\text{stat.}). \tag{9.12}$$

Thus, less than 1.1% of electrons are lost to resolution effects. A small loss is expected because the electron energy response is asymmetric due to the effect of bremsstrahlung (see, for example, the p_{T} residual distribution in Figure 5.2).

The resolution correction mixes true and reconstructed quantities, and is therefore subject to both theoretical and experimental uncertainties. The only significant theoretical uncertainty might arise from the description of final state photon radiation. It was shown already that, for the acceptance, if photon recombination is applied, this contributes a small uncertainty. It remains to be verified to what extent the details of photon radiation at small ΔR affect electron reconstruction.

The other main factors expected to contribute to the experimental uncertainty of $\mathcal{S}$ are the overall electron energy scale and the knowledge of Inner Detector material and its effect on bremsstrahlung. It has been estimated that with 200 pb^{-1} of data the overall electron energy scale can be controlled to within 0.2% ("Calibration and Performance of the Electromagnetic Calorimeter", [42]). Variations at this level leave $\mathcal{S}$ unchanged within current statistical uncertainties. $\mathcal{S}$ is sensitive to true electrons which are "lost" through bremsstrahlung in the Inner Detector, and hence to the amount of material it contains. This material has been measured during the detector installation [53] and modelled within the ATLAS simulation. This effect is mitigated by the track cuts imposed by the medium electron selection, which will likely be failed by electrons that undergo significant amounts of bremsstrahlung. If the material is well monitored by the rate of photon conversions, for example, this should not result in a significant uncertainty for the energy measurement of well-reconstructed electrons. Overall, as the correction itself is small, its systematic uncertainty is assumed to be negligible, and is not considered further until the efficiency uncertainty improves.

9.4.3 Luminosity

To measure $\sigma_{Z/\gamma^* \to e^+e^-}$, the absolute luminosity delivered to ATLAS needs to be known and understood. Initially, this will be very poorly known, with the estimated uncertainty based on the LHC machine parameters alone ranging up to 30% [53]. There are, however, several detectors associated with ATLAS which will ultimately be able to measure the bunch-by-bunch luminosity. These were described in Section 4.8. The actual luminosity uncertainty for an analysis with 200 pb^{-1} of data depends primarily on the installation schedule of the ALFA detector. If ALFA were installed and running by early 2010, an uncertainty of less than 5% might be achieved [79].

9.5 Extraction of the $Z/\gamma^* \to e^+e^-$ cross section

It is essential to verify that the event corrections applied do not introduce any unexpected bias on the extraction of $\sigma_{Z/\gamma^* \to e^+e^-}$. To test this, these correction factors have been applied back to the simulated sample which generated them. This means that the corrections and results are statistically related, potentially allowing very small biases to be seen. No background was added for this test, since the background fraction is taken directly from the simulation. The simulated signal sample contains approximately 4.9 million events, which is equivalent to an integrated luminosity of almost L = 4.5 fb^{-1}. After selection, 1.17 million events remain, which after correction using Equation 9.11 yields $N_{\text{corr}} = 1.88$ million events. Applying further corrections for luminosity, efficiency, resolution and acceptance, results for $\sigma^{\text{kin}}_{Z/\gamma^* \to e^+e^-}$ and $\sigma_{Z/\gamma^* \to e^+e^-}$ are found:

$$\sigma^{\text{kin}}_{Z/\gamma^* \to e^+e^-} = \frac{N_{\text{corr}}}{\mathcal{S}\text{L}} = 422.4 \text{ pb} \pm 0.4 \text{ pb(stat.)}, \tag{9.13}$$

$$\sigma_{Z/\gamma^* \to e^+e^-} = \frac{\sigma^{\text{kin}}_{Z/\gamma^* \to e^+e^-}}{\mathcal{A}} = 1134 \text{ pb} \pm 1.1 \text{ pb(stat.)}. \tag{9.14}$$

These are within 0.9% of the input cross sections, 425.9 pb and 1144 pb respectively. This remaining bias is considered as a systematic uncertainty on the event correction procedure, and included in the systematic uncertainty on the efficiency correction.

The estimated uncertainties for a measurement of the $Z/\gamma^* \to e^+e^-$ cross section are summarised in Table 9.3. The statistical uncertainty is negligible compared to

Table 9.3: Summary of estimated uncertainties on the total and kinematic Z/γ^* production cross sections with 200 pb^{-1} of 10 TeV collision data. The individual systematic components have been summed in quadrature.

Correction factors	Value	Uncertainty
1/Efficiency (N_{corr}/N)	1.61	2.2%
Backgrounds ($1-f$)	0.984	1.2%
Resolution ($\mathcal{S}$)	0.9894	0.13%
Total syst. (exp.)		2.5%
Acceptance ($\mathcal{A}$) (theory)	0.3723	1.6%
Luminosity ($\int \mathcal{L}dt$)	200 pb^{-1}	$5-30$%
Stat. uncertainty		0.44%

the experimental and theoretical systematic uncertainties. Only the experimental systematic uncertainties (2.5%) contribute to the measurement of $\sigma^{\text{kin}}_{Z/\gamma^*\rightarrow e^+e^-}$, whilst the expected total systematic uncertainty on $\sigma_{Z/\gamma^*\rightarrow e^+e^-}$ is higher, at 3.0%, due to the theoretical uncertainty associated with the acceptance factor. The luminosity uncertainty, which dominates the others even in the most optimistic scenario, will be discussed further in Chapter 10.

A further test was performed using the equivalent of 200 pb^{-1} of simulated $Z/\gamma^* \rightarrow e^+e^-$ events generated using the MC@NLO generator [34]. This is a Next-to-Leading Order generator, which therefore includes processes such as $gq \rightarrow Z/\gamma^* q$ which are not present in PYTHIA. Other details of the detector simulation are the same as in the PYTHIA sample, meaning that this test primarily tests the acceptance uncertainty estimate, applying the acceptance estimate from PYTHIA to pseudo-data from MC@NLO.

After applying all cuts, 6.3×10^4 events remained, more than the estimate in Table 9.2 because the NLO cross section was used for this study. After corrections, N_{corr} was found to be equal to 1.02×10^5 events. Applying the same correction factors as before, the cross section obtained was

$$\sigma_{Z/\gamma^*\rightarrow e^+e^-} = 1379 \text{ pb} \pm 5 \text{ pb(stat.)} \pm 34 \text{ pb(exp.)} \pm 22 \text{ pb(theory)}. \quad (9.15)$$

This value of $\sigma_{Z/\gamma^*\rightarrow e^+e^-}$ is 1.6% higher than the input cross section of 1357 pb, which is within the expected theoretical uncertainty.

9.6 Summary

In this chapter, a procedure for measuring the inclusive $Z/\gamma^* \rightarrow e^+e^-$ cross section with 200 pb^{-1} of pp collision data has been demonstrated. The expected background fraction has been estimated, and is small compared to the signal. Large corrections for electron reconstruction and identification efficiencies are necessary, of which we will have limited knowledge in early data. Nevertheless, experimental systematics are expected to be controlled to within 2.5%. Extrapolation of the cross section outside the detector acceptance for electrons introduces an additional 1.6% theoretical uncertainty. One of the principal uncertainties is the knowledge of the integrated luminosity. Initially, this will be poorly known, but its estimation is expected to improve with time. This will be discussed further in the concluding chapter.

Chapter 10

Summary and outlook

This thesis has examined Z/γ^* boson production at the LHC and the detection of the $Z/\gamma^* \rightarrow e^+e^-$ decay in ATLAS using simulated events. This is an important channel for the early data-taking period of the LHC because of its clean experimental signature, high cross section and sensitivity to *pdf*s. The extraction of the total Z/γ^* boson production cross section has been studied, under the assumption that 200 pb^{-1} of data will be collected with a CM collision energy of $\sqrt{s} = 10$ TeV. New methods were presented for estimating the dominant backgrounds for this channel using limited Monte Carlo statistics. The measurement of electron trigger efficiencies from data and theoretical studies of the acceptance uncertainty in $Z/\gamma^* \rightarrow e^+e^-$ events were also presented. To facilitate these studies, new analysis software working within the general ATLAS framework was developed [112], which is now in use for studies of many different high energy physics topics.

The early measurement of the inclusive Z/γ^* boson cross section with ATLAS with 14 TeV data has been studied by others [42]. The present study, aimed at a lower centre of mass energy but a greater integrated luminosity, has addressed additional sources of both experimental and theoretical systematic uncertainty not considered in this previous work. In particular, more detailed studies have been made of the background sources, theoretical acceptance and corrections for detector effects such as reconstruction efficiencies and energy resolution. Additionally, a realistic prescription had been developed for measuring a "kinematic" cross section that does not involve extrapolation beyond the detector's acceptance. This cross section can be measured more precisely, with smaller theoretical uncertainties.

After analysis of the anticipated backgrounds, efficiencies and other detector effects, the expected systematic uncertainty for the extraction of the total $Z/\gamma^* \to e^+e^-$ cross section with 200 pb^{-1} of data is 3.0%, excluding the luminosity uncertainty. This uncertainty is reduced to 2.5% for a measurement of the kinematic cross section.

The principal experimental uncertainty (apart from the integrated luminosity determination) arises from the experimental knowledge of the electron reconstruction and identification efficiencies. These will be measured from data using the tag and probe method, which is described in Chapter 8 in the context of electron trigger efficiency measurements. Trigger efficiencies, for reconstructed electrons already passing offline selection criteria, can be measured with little bias and good statistical precision. This thesis shows that binned differential electron trigger efficiencies can be measured with a precision of $0.5 - 1\%$ per bin with as little as 50 pb^{-1} of data. While invaluable for monitoring the performance of the ATLAS trigger system, these measurements only have a minor impact on the Z/γ^* cross section measurement. The electron reconstruction and identification efficiency measurements, which contribute significantly to the experimental uncertainty on $\sigma_{Z/\gamma^* \to e^+e^-}$, suffer from higher backgrounds and less well-controlled systematic uncertainties. These will need to be studied further to be fully understood, in order to improve the precision of the Z/γ^* cross section measurement.

Another important experimental uncertainty arises from the background fraction after selection and efficiency corrections. An event scaling method has been developed in this thesis that produces a more statistically powerful background estimate despite the finite number of simulated QCD background events and the high rejection factors achieved by the electron identification cuts. This method improves the statistical precision of simulated background samples, and could be further improved if heavy flavour decays to electrons, an important background component, were simulated separately. The overall normalisation of the QCD background is still uncertain, due to theoretical uncertainties, and will need to be constrained using data.

The theoretical uncertainties associated with the extrapolation of the $Z/\gamma^* \to e^+e^-$ cross section measurement into unobserved regions of phase space have also been investigated. These uncertainties are of a similar size to the anticipated experimental

systematic uncertainties. The effects of soft QCD interactions modelled by PYTHIA and photon radiation modelled by PHOTOS on the acceptance of $Z/\gamma^* \to e^+e^-$ events have been studied, and a procedure for applying K-factors from higher order calculations has been described. The effects of recombining the 4-momenta of nearby electrons and photons has also been examined as a simple model of the clustering performance of the ATLAS electromagnetic calorimeter. Applying this procedure reduces the size of QED corrections to the acceptance significantly. This recombination has also been used in the definition of the kinematic cross section used in this thesis. Further studies should investigate assumptions made about the impact of higher order QCD effects on the acceptance, and make use of recent theoretical developments in the understanding of the interplay between electroweak and QCD processes in Drell-Yan production at the LHC [117].

It has been assumed that, following the incident on September 19$^{\text{th}}$ 2008, early physics data will be collected with a CM collision energy of 10 TeV, or 5 TeV per beam. Discussions about the likely early beam conditions [118] have concluded that this is the maximum beam energy that can be considered for collisions in 2010, and some data for physics analysis may be taken with lower energy beams. As the beam energy decreases, so does the Z/γ^* boson cross section and, although the measurement of $\sigma_{Z/\gamma^* \to e^+e^-}$ is not statistically limited, the precision with which the electron reconstruction efficiency can be measured with data will be reduced. It is predicted that at $\sqrt{s} = 8$ TeV, for example, the useful Z yield will drop by between 20 and 25% of what would be observed with the same integrated luminosity at $\sqrt{s} = 10$ TeV [119]. If this is the case, the uncertainties from tag and probe measurements of the electron reconstruction and identification efficiencies might be expected to increase by approximately 10%, and the background estimate will also be affected. Other aspects of the measurement, such as the small resolution correction or the theoretical acceptance calculation, will be less affected, as they are not limited by the signal event rates.

The dominant uncertainty in any measurement of an absolute cross section is in the integrated luminosity, $\int \mathcal{L} dt$. The systematic uncertainty on the integrated luminosity may be as much as 30% for the very first data, from estimation of the beam parameters

alone. The ALFA detector [53, 79, 86] could ultimately reduce the uncertainty to below 5%, but it now appears unlikely that it will be available for early collisions. The relatively small experimental and theoretical systematic uncertainties on the Z/γ^* boson production cross section suggest that the rate of $Z/\gamma^* \to e^+e^-$ production could be used as an alternative luminosity measure. With increased understanding of the systematic uncertainties, a measurement of the absolute luminosity with $\mathcal{O}(1-2\%)$ precision might be possible. This would however be achieved at the cost of losing an independent measurement of $\sigma_{Z/\gamma^* \to e^+e^-}$, and having a luminosity estimate that correlates with *pdf* assumptions.

The techniques and methods used in this analysis of $\sigma_{Z/\gamma^* \to e^+e^-}$ can be applied to other related SM measurements, which do not have a dependency on the luminosity estimation. One of these is the ratio $\sigma_{W \to e\nu_e}/\sigma_{Z/\gamma^* \to e^+e^-}$, which has a very precise theoretical prediction [26]. In addition, some sources of experimental systematic uncertainty, such as electron reconstruction efficiencies, will partially cancel in this measurement, further improving its precision.

Another important measurement will be of the Z/γ^* production spectra, especially in its rapidity and p_{T}. These measurements can be made independent of the integrated luminosity by defining the ratios $\frac{1}{\sigma}\frac{d\sigma}{dy}$ and $\frac{1}{\sigma}\frac{d\sigma}{dp_{\mathrm{T}}}$. The former is sensitive to *pdf*s, as the boson rapidity is related to the partons' x values. At leading order:

$$y_Z = \frac{1}{2}\ln\frac{x_1}{x_2}. \tag{10.1}$$

The boson p_{T} spectrum is dependent on QCD radiation in the initial state, as seen in Chapter 3, and is therefore sensitive to higher order effects, including soft QCD processes. It was shown in Section 9.3.5 that there is already a good understanding of the efficiency corrections required for the measurement of these distributions, using the correction methods developed for the measurement of the total cross section $\sigma_{Z/\gamma^* \to e^+e^-}$. The inclusion of bin migration corrections would further improve this.

In the longer term, study of the Drell-Yan spectrum extended to higher masses may produce hints of new physics, beyond the Standard Model. Several models predict high mass resonances which decay into opposite-sign lepton pairs, including new gauge groups (*eg* [120]), technicolour [121] and compactified extra dimensions [122]. These

resonances would appear as peaks in the invariant mass spectrum M_{ee}, much like the Z boson itself, and can be studied using similar techniques. Recent searches for di-electron resonances at the Tevatron have failed to find evidence of the existience of new resonances for masses $< \mathcal{O}(1\ \mathrm{TeV}/c^2)$ [123, 124, 125], but the high collision energy and luminosity of the LHC should extend these searches up to at least 3.5 TeV/c^2 [42].

To conclude, studies of the $Z/\gamma^* \rightarrow e^+e^-$ process are central to understanding theoretical and experimental factors affecting high energy physics studies in ATLAS. Measurement of the Z/γ^* production cross section can provide information about the proton parton density functions, and test the theoretical frameworks of QED and QCD. In addition, practical information about the detector's performance and operation can be obtained. The resulting improvements in the theoretical calculations and the detector simulation will have wide-ranging implications for the entire physics programme of ATLAS, including the potential discoveries of the much anticipated Higgs boson and new high mass particles at the LHC. This makes the Z boson one of the most important particles to study with early data at the LHC.

Bibliography

[1] J. J. Thomson. Cathode rays. *Phil. Mag.*, 44:293–316, 1897.

[2] A. Abulencia et al. Measurements of inclusive W and Z cross sections in p-pbar collisions at $\sqrt{s} = 1.96$ TeV. *J. Phys.*, G34:2457–2544, 2007.

[3] D0 Collaboration. Measurement of the cross section for W and Z production to electron final states with the D0 detector at $\sqrt{s} = 1.96$ TeV, 2004, D0Note 4403-CONF.

[4] W. N. Cottingham and D. A. Greenwood. *An introduction to the Standard Model of particle physics*. Cambridge Univ. Press, 2^{nd} edition, 2007.

[5] W. E. Burcham and M. Jobes. *Nuclear and particle physics*. Prentice Hall, 2^{nd} edition, 1994.

[6] S. L. Glashow. Partial symmetries of weak interactions. *Nucl. Phys.*, 22:579–588, 1961.

[7] S. Weinberg. A model of leptons. *Phys. Rev. Lett.*, 19:1264–1266, 1967.

[8] A. Salam. Weak and electromagnetic interactions. *Svartholm: Elementary Particle Theory, Proceedings Of The Nobel Symposium Held At Lerum, Sweden*, pages 367–377, 1968.

[9] M. Goldhaber, L. Grodzins, and A. W. Sunyar. Helicity of neutrinos. *Phys. Rev.*, 109:1015–1017, 1958.

[10] F. Englert and R. Brout. Broken symmetry and the mass of gauge vector mesons. *Phys. Rev. Lett.*, 13:321–322, 1964.

[11] P. W. Higgs. Broken symmetries and the masses of gauge bosons. *Phys. Rev. Lett.*, 13:508–509, 1964.

[12] G. S. Guralnik, C. R. Hagen, and T. W. B. Kibble. Global conservation laws and massless particles. *Phys. Rev. Lett.*, 13:585–587, 1964.

[13] The LEP and SLD Collaborations. Precision electroweak measurements on the Z resonance. *Phys. Rept.*, 427:257, 2006.

[14] The LEP, SLD and Tevatron Collaborations. Precision electroweak measurements and constraints on the Standard Model. 2008, arXiv:0811.4682 [hep-ex].

[15] C. Amsler et al. Review of particle physics. *Phys. Lett.*, B667:1, 2008.

[16] M. Gell-Mann. A schematic model of baryons and mesons. *Phys. Lett.*, 8:214–215, 1964.

[17] G. Zweig. An SU(3) model for strong interaction symmetry and its breaking, (2 Parts). 1964, CERN-TH-401, CERN-TH-412.

[18] S. D. Drell and T-M. Yan. Massive lepton pair production in hadron-hadron collisions at high-energies. *Phys. Rev. Lett.*, 25:316–320, 1970. [Erratum - ibid. 25:902, 1970].

[19] R. Devenish and A. Cooper-Sarkar. *Deep inelastic scattering.* 2004. Oxford Univ. Press.

[20] P. M. Nadolsky et al. Implications of CTEQ global analysis for collider observables. *Phys. Rev.*, D78:013004, 2008.

[21] A. D. Martin, W. J. Stirling, R. S. Thorne, and G. Watt. Parton distributions for the LHC. *Eur. Phys. J.*, C63:189–285, 2009.

[22] H1 and ZEUS Collaborations. Combination and QCD analysis of H1 and ZEUS deep inelastic $e^{\pm}p$ scattering cross section measurements. 2009. H1prelim-09-045, ZEUS-prel-09-011, ZEUS-prel-09-012.

[23] G. Altarelli and G. Parisi. Asymptotic freedom in parton language. *Nucl. Phys.*, B126:298, 1977.

[24] J. Pumplin et al. New generation of parton distributions with uncertainties from global QCD analysis. *JHEP*, 07:012, 2002.

[25] J. C. Collins and D. E. Soper. The theorems of perturbative QCD. *Ann. Rev. Nucl. Part. Sci.*, 37:383–409, 1987.

[26] H. Jung et al. Proceedings of the workshop: HERA and the LHC workshop series on the implications of HERA for LHC physics. 2009, arXiv:0903.3861 [hep-ph].

[27] K. Melnikov and F. Petriello. Electroweak gauge boson production at hadron colliders through $\mathcal{O}(\alpha(s)^2)$. *Phys. Rev.*, D74:114017, 2006.

[28] C. M. Carloni Calame, G. Montagna, O. Nicrosini, and A. Vicini. Precision electroweak calculation of the charged current Drell-Yan process. *JHEP*, 12:016, 2006.

[29] C. M. Carloni Calame, G. Montagna, O. Nicrosini, and A. Vicini. Precision electroweak calculation of the production of a high transverse-momentum lepton pair at hadron colliders. *JHEP*, 10:109, 2007.

[30] T. Sjostrand, S. Mrenna, and P. Skands. A brief introduction to PYTHIA 8.1. *Comput. Phys. Commun.*, 178:852–867, 2008.

[31] T. Sjostrand, S. Mrenna, and P. Skands. PYTHIA 6.4 physics and manual. *JHEP*, 05:026, 2006.

[32] G. Corcella et al. HERWIG 6.5: An event generator for hadron emission reactions with interfering gluons (including supersymmetric processes). *JHEP*, 01:010, 2001.

[33] G. Corcella et al. HERWIG 6.5 release note. 2002, arXiv:hep-ph/0210213.

[34] S. Frixione and B. R. Webber. Matching NLO QCD computations and parton shower simulations. *JHEP*, 06:029, 2002.

[35] A. Moraes, C. Buttar, and I. Dawson. Prediction for minimum bias and the underlying event at LHC energies. *Eur. Phys. J.*, C50:435–466, 2007.

[36] T. Sjostrand and P. Z. Skands. Transverse-momentum-ordered showers and interleaved multiple interactions. *Eur. Phys. J.*, C39:129–154, 2005.

[37] E. Barberio and Z. Was. PHOTOS: A universal Monte Carlo for QED radiative corrections. Version 2.0. *Comput. Phys. Commun.*, 79:291–308, 1994.

[38] E. Barberio, B. van Eijk, and Z. Was. PHOTOS: A universal Monte Carlo for QED radiative corrections in decays. *Comput. Phys. Commun.*, 66:115–128, 1991.

[39] S. Jadach, J. H. Kuhn, and Z. Was. TAUOLA: A library of Monte Carlo programs to simulate decays of polarized tau leptons. *Comput. Phys. Commun.*, 64:275–299, 1990.

[40] Z. Was. TAUOLA, TAUOLA universal interface PHOTOS and MC-TESTER: Status Report. *Nucl. Phys. Proc. Suppl.*, 189:43–48, 2009.

[41] J. M. Butterworth, J. R. Forshaw, and M. H. Seymour. Multiparton interactions in photoproduction at HERA. *Z. Phys.*, C72:637–646, 1996. See `http://projects.hepforge.org/jimmy/`.

[42] G. Aad et al. Expected performance of the ATLAS experiment - detector, trigger and physics. 2009, arXiv:0901.0512 [hep-ex].

[43] G. Altarelli, R. K. Ellis, and G. Martinelli. Large perturbative corrections to the Drell-Yan process in QCD. *Nucl. Phys.*, B157:461, 1979.

[44] N. E. Adam, V. Halyo, and S. A. Yost. Evaluation of the theoretical uncertainties in the $Z \to \ell^+\ell^-$ cross sections at the LHC. *JHEP*, 05:062, 2008.

[45] P. Golonka and Z. Was. Next to leading logarithms and the PHOTOS Monte Carlo. *Eur. Phys. J.*, C50:53–62, 2007.

[46] J. Campbell and R. K. Ellis. Next-to-leading order corrections to W + 2jet and Z + 2jet production at hadron colliders. *Phys. Rev.*, D65:113007, 2002.

[47] J. Campbell, R. K. Ellis, and D. L. Rainwater. Next-to-leading order QCD predictions for W + 2jet and Z + 2jet production at the CERN LHC. *Phys. Rev.*, D68:094021, 2003.

[48] F. D. Aaron et al. A precision measurement of the inclusive ep scattering cross section at HERA. 2009, arXiv:0904.3513 [hep-ex]. Submitted to Eur. Phys. J. C.

[49] G. Davatz, G. Dissertori, M. Dittmar, M. Grazzini, and F. Pauss. Effective K-factors for $gg \to H \to WW \to \ell\nu\ell\nu$ at the LHC. *JHEP*, 05:009, 2004.

[50] G. Davatz et al. Combining Monte Carlo generators with next-to-next-to-leading order calculations: Event reweighting for Higgs boson production at the LHC. *JHEP*, 07:037, 2006.

[51] L. Evans and P. Bryant, (ed.). LHC machine. *JINST*, 3:S08001, 2008.

[52] Summary of the analysis of the 19 September 2008 incident at the LHC. CERN Press Release, Geneva 2008.

[53] G. Aad et al. The ATLAS experiment at the CERN Large Hadron Collider. *JINST*, 3:S08003, 2008.

[54] ATLAS Collaboration. ATLAS detector and physics performance Technical Design Report, (2 volumes). 1999, CERN-LHCC-99-14, CERN-LHCC-99-15.

[55] K. Aamodt et al. The ALICE experiment at the CERN LHC. *JINST*, 3:S08002, 2008.

[56] R. Adolphi et al. The CMS experiment at the CERN LHC. *JINST*, 3:S08004, 2008.

[57] A. A. Alves, Jr et al. The LHCb detector at the LHC. *JINST*, 3:S08005, 2008.

[58] O. Adriani et al. The LHCf detector at the CERN Large Hadron Collider. *JINST*, 3:S08006, 2008.

[59] G. Anelli et al. The TOTEM experiment at the CERN Large Hadron Collider. *JINST*, 3:S08007, 2008.

[60] ATLAS Collaboration. ATLAS Inner Detector: Technical Design Report (2 volumes). 1997, CERN-LHCC-97-016, CERN-LHCC-97-017.

[61] G. Aad. ATLAS pixel detector electronics and sensors. *JINST*, 3:P07007, 2008.

[62] F. Lemeilleur, G. Lindstrom, and S. Watts. Third RD48 status report. 2000, CERN-LHCC-2000-009.

[63] V. Cindro et al. The ATLAS beam conditions monitor. *JINST*, 3:P02004, 2008.

[64] A. Abdesselam et al. The barrel modules of the ATLAS semiconductor tracker. *Nucl. Instrum. Meth.*, A568:642–671, 2006.

[65] A. Abdesselam et al. The ATLAS semiconductor tracker end-cap modules. *Nucl. Instrum. Meth.*, A575:353–389, 2007.

[66] E. Abat et al. The ATLAS Transition Radiation Tracker (TRT) proportional drift tube: Design and performance. *JINST*, 3:P02013, 2008.

[67] E. Abat et al. The ATLAS TRT barrel detector. *JINST*, 3:P02014, 2008.

[68] E. Abat et al. The ATLAS TRT end-cap detectors. *JINST*, 3:P10003, 2008.

[69] B. Aubert et al. Construction, assembly and tests of the ATLAS electromagnetic barrel calorimeter. *Nucl. Instrum. Meth.*, A558:388–418, 2006.

[70] M. Aleksa et al. Construction, assembly and tests of the ATLAS electromagnetic end-cap calorimeters. *JINST*, 3:P06002, 2008.

[71] ATLAS Collaboration. ATLAS liquid-argon calorimeter: Technical Design Report. 1996, CERN-LHCC-96-041.

[72] M. Aharrouche et al. Energy linearity and resolution of the ATLAS electromagnetic barrel calorimeter in an electron test-beam. *Nucl. Instrum. Meth.*, A568:601–623, 2006.

[73] M. Aharrouche et al. Response uniformity of the ATLAS liquid argon electromagnetic calorimeter. *Nucl. Instrum. Meth.*, A582:429–455, 2007.

[74] J. Colas et al. Position resolution and particle identification with the ATLAS EM calorimeter. *Nucl. Instrum. Meth.*, A550:96–115, 2005.

[75] ATLAS Collaboration. ATLAS tile calorimeter: Technical Design Report. 1996, CERN-LHCC-96-042.

[76] D. M. Gingrich et al. Construction, assembly and testing of the ATLAS hadronic end-cap calorimeter. *JINST*, 2:P05005, 2007.

[77] ATLAS Collaboration. ATLAS calorimeter performance: Technical Design Report. 1996, CERN-LHCC-96-040.

[78] J. P. Archambault et al. The ATLAS forward calorimeter. *JINST*, 3:P02010, 2008.

[79] ATLAS Collaboration. ATLAS forward detectors for measurement of elastic scattering and luminosity. 2008, CERN-LHCC-2008-004.

[80] ATLAS Collaboration. Zero degree calorimeters for ATLAS. 2007, CERN-LHCC-2007-001.

[81] ATLAS Collaboration. ATLAS muon spectrometer: Technical Design Report. 1997, CERN-LHCC-97-022.

[82] ATLAS Collaboration. ATLAS high-level trigger, data-acquisition and controls: Technical Design Report. 2003, CERN-LHCC-2003-022.

[83] ATLAS Collaboration. ATLAS level 1 trigger: Technical Design Report. 1998, CERN-LHCC-98-014.

[84] R. Achenbach et al. The ATLAS level-1 calorimeter trigger. *JINST*, 3:P03001, 2008.

[85] Robert Blair et al. The ATLAS high level trigger region of interest builder. *JINST*, 3:P04001, 2008.

[86] P. Jenni and M. Nessi. ATLAS forward detectors for luminosity measurement and monitoring. 2004, CERN-LHCC-2004-010.

[87] T. Pauly. Readiness of the ATLAS experiment for first data. 2009, ATL-GEN-PROC-2009-007.

[88] R. Achenbach et al. First data with the ATLAS level-1 calorimeter trigger. 2008, ATL-DAQ-PROC-2008-006.

[89] C. Padilla. Commissioning of the ATLAS high level trigger with single LHC beam and cosmic rays. 2009, ATL-DAQ-PROC-2009-017.

[90] A. Andreazza. Commissioning and performance of the ATLAS Inner Detector with the first beam and cosmic data. 2009, ATL-INDET-PROC-2009-009.

[91] S. Montesano. Results from the commissioning of the ATLAS pixel detector with cosmic ray data. 2009, ATL-INDET-PROC-2009-010.

[92] M. Cooke et al. In situ commissioning of the ATLAS electromagnetic calorimeter with cosmic muons. 2007, ATL-LARG-PUB-2007-013.

[93] P. S. Mangeard. Performance of the ATLAS liquid argon calorimeter with cosmic muons and single LHC beam data. 2009, ATL-LARG-PROC-2009-003.

[94] S. Laplace. Commissioning of the ATLAS liquid argon calorimeter. 2009, ATL-LARG-PROC-2009-005.

[95] W. Lampl et al. Calorimeter clustering algorithms: Description and performance. 2008, ATL-LARG-PUB-2008-002.

[96] T. Cornelissen et al. Concepts, design and implementation of the ATLAS New Tracking (NEWT). 2007, ATL-SOFT-PUB-2007-007.

[97] D. Banfi, L. Carminati, and L. Mandelli. Calibration of the ATLAS electromagnetic calorimeter using calibration hits. 2007, ATL-LARG-PUB-2007-012.

[98] V. Kartvelishvili. Electron bremsstrahlung recovery in ATLAS. *Nucl. Phys. Proc. Suppl.*, 172:208–211, 2007.

[99] ATLAS Collaboration. ATLAS computing: Technical Design Report. 2005, CERN-LHCC-2005-022.

[100] R. Brun and F. Rademakers. ROOT: An object oriented data analysis framework. *Nucl. Instrum. Meth.*, A389:81–86, 1997. For more information, see `http://root.cern.ch`.

[101] `http://pool.cern.ch/`.

[102] A. Stepanov and M. Lee. The Standard Template Library. HP Laboratories Technical Report 95-11. 1995.

[103] `https://twiki.cern.ch/twiki/bin/view/Atlas/AtlfastDocumentation`.

[104] S. Gieseke et al. Herwig++ 2.0 release note. 2006, arXiv:hep-ph/0609306.

[105] M. L. Mangano, M. Moretti, F. Piccinini, R. Pittau, and A. D. Polosa. ALPGEN, a generator for hard multiparton processes in hadronic collisions. *JHEP*, 07:001, 2003.

[106] D.-C. Dai et al. BlackMax: A black-hole event generator with rotation, recoil, split branes and brane tension. *Phys. Rev.*, D77:076007, 2008.

[107] M. Dobbs and J. B. Hansen. The HepMC C++ Monte Carlo event record for high energy physics. *Comput. Phys. Commun.*, 134:41–46, 2001.

[108] Z. Marshall. The ATLAS simulation software. ATL-SOFT-PROC-2008-001.

[109] S. Agostinelli et al. GEANT4: A simulation toolkit. *Nucl. Instrum. Meth.*, A506:250–303, 2003.

[110] I. Bird, (ed.) et al. LHC computing Grid. Technical Design Report. CERN-LHCC-2005-024.

[111] F. Brochu et al. Ganga: a tool for computational-task management and easy access to grid resources. 2009, arXiv:0902.2685 [cs.DC].

[112] `http://hep.ph.liv.ac.uk/twiki/bin/view/ATLAS/LiverpoolAnalysis`.

[113] J. Gaiser et al. Charmonium spectroscopy from inclusive ψ' and J/ψ radiative decays. *Phys. Rev.*, D34:711, 1986.

[114] https://twiki.cern.ch/twiki/bin/view/Atlas/FullDressRehearsal.

[115] J. Han, A. Bodek, W. Sakumoto, and Y. Chung. $d\sigma/dy$ distribution of Drell-Yan dielectron pairs at CDF. *J. Phys. Conf. Ser.*, 110:042009, 2008.

[116] J. Han. The differential cross section distribution of Drell-Yan dielectron pairs in the Z boson mass region. FERMILAB-THESIS-2008-65.

[117] G. Balossini et al. Combination of electroweak and QCD corrections to single W production at the Fermilab Tevatron and the CERN LHC. 2009, arXiv:0907.0276 [hep-ph].

[118] C Carli (ed.). Chamonix 2009 workshop on LHC performance. CERN-ATS-2009-001.

[119] https://twiki.cern.ch/twiki/bin/view/Atlas/AtlasResultsEcmDependence.

[120] H. Georgi and S. L. Glashow. Unity of all elementary particle forces. *Phys. Rev. Lett.*, 32:438–441, 1974.

[121] K. D. Lane and E. Eichten. Two scale technicolor. *Phys. Lett.*, B222:274, 1989.

[122] L. Randall and R. Sundrum. A large mass hierarchy from a small extra dimension. *Phys. Rev. Lett.*, 83:3370–3373, 1999.

[123] V. M. Abazov et al. Search for Randall-Sundrum gravitons in dilepton and diphoton final states. *Phys. Rev. Lett.*, 95:091801, 2005.

[124] D0 Collaboration. Search for high-mass narrow resonances in the di-electron channel at D0. 2009. D0Note 5923-CONF.

[125] T. Aaltonen et al. Search for high-mass e^+e^- resonances in $p\bar{p}$ collisions at $\sqrt{s} = 1.96$ TeV. *Phys. Rev. Lett.*, 102:031801, 2009.